The Fluid Mechanics of Microdevices---The Freeman Scholar Lecture

Article *in* Journal of Fluids Engineering · May 1999

DOI: 10.1115/1.2822013 · Source: CiteSeer

The Fluid Mechanics of Microdevices—The Freeman Scholar Lecture

Mohamed Gad-el-Hak
Professor,
Department of Aerospace and
Mechanical Engineering,
University of Notre Dame,
Notre Dame, IN 46556.
Fellow ASME
E-mail: Mohamed.Gad-el-Hak.1@nd.edu

Manufacturing processes that can create extremely small machines have been developed in recent years. Microelectromechanical systems (MEMS) refer to devices that have characteristic length of less than 1 mm but more than 1 micron, that combine electrical and mechanical components and that are fabricated using integrated circuit batch-processing techniques. Electrostatic, magnetic, pneumatic and thermal actuators, motors, valves, gears, and tweezers of less than 100-μm size have been fabricated. These have been used as sensors for pressure, temperature, mass flow, velocity and sound, as actuators for linear and angular motions, and as simple components for complex systems such as micro-heat-engines and micro-heat-pumps. The technology is progressing at a rate that far exceeds that of our understanding of the unconventional physics involved in the operation as well as the manufacturing of those minute devices. The primary objective of this article is to critically review the status of our understanding of fluid flow phenomena particular to microdevices. In terms of applications, the paper emphasizes the use of MEMS as sensors and actuators for flow diagnosis and control.

About the Author

Mohamed Gad-el-Hak received his B.Sc. (summa cum laude) in mechanical engineering from Ain Shams University in 1966 and his Ph.D. in fluid mechanics from the Johns Hopkins University in 1973. He has since taught and conducted research at the University of Southern California, University of Virginia, Institut National Polytechnique de Grenoble, and Université de Poitiers, and has lectured extensively at seminars in the United States and overseas. Dr. Gad-el-Hak is currently Professor of Aerospace and Mechanical Engineering at the University of Notre Dame. Prior to that, he was a Senior Research Scientist and Program Manager at Flow Research Company in Seattle, Washington. Dr. Gad-el-Hak has published over 280 articles and presented 170 invited lectures in the basic and applied research areas of isotropic turbulence, boundary layer flows, stratified flows, compliant coatings, unsteady aerodynamics, biological flows, non-Newtonian fluids, hard and soft computing including genetic algorithms, and flow control. He is the author of the book *Flow Control*, and editor of three Springer-Verlag's books *Frontiers in Experimental Fluid Mechanics*, *Advances in Fluid Mechanics Measurements*, and *Flow Control: Fundamentals and Practices.* Professor Gad-el-Hak is a fellow of The American Society of Mechanical Engineers, a life member of the American Physical Society, and an associate fellow of the American Institute of Aeronautics and Astronautics. He has recently been inducted as an eminent engineer in Tau Beta Pi, an honorary member in Sigma Gamma Tau and Pi Tau Sigma, and a member-at-large in Sigma Xi. From 1988 to 1991, Dr. Gad-el-Hak served as Associate Editor for *AIAA Journal.* He is currently an Associate Editor for *Applied Mechanics Reviews.* In 1998, Professor Gad-el-Hak was named the Fourteenth ASME Freeman Scholar.

1 Introduction

How many times when you are working on something frustratingly tiny, like your wife's wrist watch, have you said to yourself, ''If I could only train an ant to do this!'' What I would like to suggest is the possibility of training an ant to train a mite to do this. What are the possibilities of small but movable machines? They may or may not be useful, but they surely would be fun to make.

(From the talk ''There's Plenty of Room at the Bottom,'' delivered by Richard P. Feynman at the annual meeting of the American Physical Society, Pasadena, California, 29 December 1959.)

Tool making has always differentiated our species from all others on earth. Aerodynamically correct wooden spears were carved by archaic homosapiens close to 400,000 years ago. Man builds things consistent with his size, typically in the range of two orders of magnitude larger or smaller than himself, as indicated in Fig. 1. (Though the extremes of length-scale are outside the range of this figure, man, at slightly more than 10^0 m, amazingly fits right in the middle of the smallest subatomic particle which is approximately 10^{-26} m and the extent of the observable universe which is $\sim 1.42 \times 10^{26}$ m (15 billion light years). An egocentric universe indeed!) But humans have always striven to explore, build, and control the extremes of length and time scales. In the voyages to Lilliput and Brobdingnag of *Gulliver's Travels*, Jonathan Swift (1727) speculates on the remarkable possibilities which diminution or magnification of physical dimensions provides. The Great Pyramid of Khufu was originally 147 m high when completed around 2600 B.C., while the Empire State Building constructed in 1931 is presently—after the addition of a television antenna mast in 1950—449 m high. At the other end of the spectrum of man-made artifacts, a dime is slightly less than 2 cm in diameter. Watchmakers have practiced the art of miniaturization since the thirteenth century. The invention of the microscope in the seventeenth century opened the way for direct observation of microbes and plant and animal cells. Smaller things were manmade in the latter half of this century. The transistor—invented in 1948—in today integrated circuits has a size of 0.25 micron in production and approaches 50 nanometers in research laboratories. But what about the miniaturization of mechanical parts—machines—envisioned by Feynman (1961) in his legendary speech quoted above?

Manufacturing processes that can create extremely small machines have been developed in recent years (Angell et al., 1983;

Contributed by the Fluids Engineering Division for publication in the JOURNAL OF FLUIDS ENGINEERING. Manuscript received by the Fluids Engineering Division August 31, 1998; revised manuscript received December 14, 1998. Associate Technical Editor: D. P. Telionis.

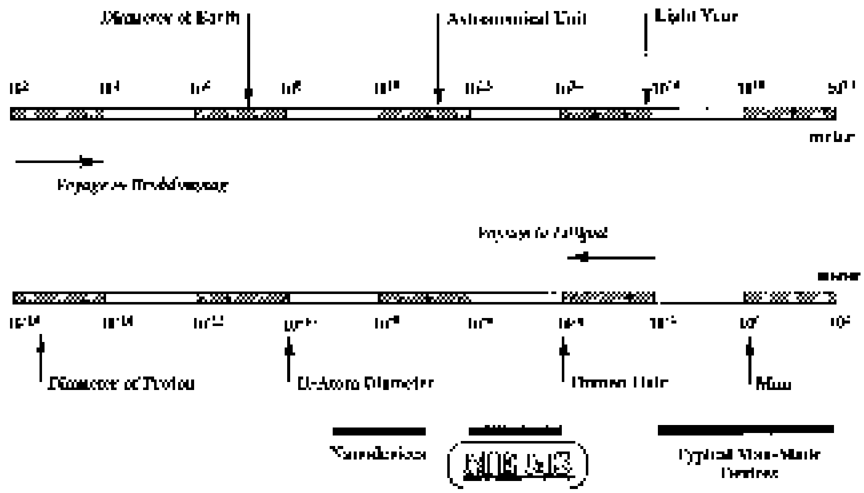

Fig. 1 The scale of things, in meters. Lower scale continues in the upper bar from left to right.

Gabriel et al., 1988; 1992; O'Connor, 1992; Gravesen et al., 1993; Bryzek et al., 1994; Gabriel, 1995; Hogan, 1996; Ho and Tai, 1996; 1998; Tien, 1997; Busch-Vishniac, 1998; Amato, 1998). Electrostatic, magnetic, pneumatic and thermal actuators, motors, valves, gears and tweezers of less than 100 μm size have been fabricated. These have been used as sensors for pressure, temperature, mass flow, velocity and sound, as actuators for linear and angular motions, and as simple components for complex systems such as micro-heat-engines and micro-heat-pumps (Lipkin, 1993; Garcia and Sniegowski, 1993; 1995; Sniegowski and Garcia, 1996; Epstein and Senturia, 1997; Epstein et al., 1997). The technology is progressing at a rate that far exceeds that of our understanding of the unconventional physics involved in the operation as well as the manufacturing of those minute devices. The present paper focuses on one aspect of such physics: fluid flow phenomena associated with micro-scale devices. In terms of applications, the paper will emphasize the use of MEMS as sensors and actuators for flow diagnosis and control.

Microelectromechanical systems (MEMS) refer to devices that have characteristic length of less than 1 mm but more than 1 micron, that combine electrical and mechanical components and that are fabricated using integrated circuit batch-processing technologies. Current manufacturing techniques for MEMS include surface silicon micromachining; bulk silicon micromachining; lithography, electrodeposition and plastic molding (or, in its original German, lithographie galvanoformung abformung, LIGA); and electrodischarge machining (EDM). As indicated in Fig. 1, MEMS are more than four orders of magnitude larger than the diameter of the hydrogen atom, but about four orders of magnitude smaller than the traditional man-made artifacts. Nanodevices (some say NEMS) further push the envelope of electromechanical miniaturization.

Despite Feynman's demurring regarding the usefulness of small machines, MEMS are finding increased applications in a variety of industrial and medical fields, with a potential worldwide market in the billions of dollars. Accelerometers for automobile airbags, keyless entry systems, dense arrays of micromirrors for high-definition optical displays, scanning electron microscope tips to image single atoms, micro-heat-exchangers for cooling of electronic circuits, reactors for separating biological cells, blood analyzers and pressure sensors for catheter tips are but a few of current usage. Microducts are used in infrared detectors, diode lasers, miniature gas chromatographs and high-frequency fluidic control systems. Micropumps are used for ink jet printing, environmental testing and electronic cooling. Potential medical applications for small pumps include controlled delivery and monitoring of minute amount of medication, manufacturing of nanoliters of chemicals and development of artificial pancreas. Several new journals are dedicated to the science and technology of MEMS, for example IEEE/ASME *Journal of Microelectromechanical Systems, Journal of Micromechanics and Microengineering,* and *Microscale Thermophysical Engineering.*

Not all MEMS devices involve fluid flows, but the present review will focus on the ones that do. Microducts, micropumps, microturbines and microvalves are examples of small devices involving the flow of liquids and gases. MEMS can also be related to fluid flows in an indirect way. The availability of inexpensive, batch-processing-produced microsensors and microactuators provides opportunities for targeting small-scale coherent structures in macroscopic turbulent shear flows. Flow control using MEMS promises a quantum leap in control system performance. The present article will cover both the direct and indirect aspects of microdevices and fluid flows. Section 2 addresses the question of modeling fluid flows in microdevices, and Section 3 gives a brief overview of typical applications of MEMS in the field of fluid mechanics. The paper by Löfdahl and Gad-el-Hak (1999) provides more detail on MEMS applications in turbulence and flow control.

The Freeman Scholarship is bestowed biennially, in even-numbered years. The Fourteenth Freeman Lecture presented in 1998 is, therefore, the last of its kind in this millennium, and the topic of micromachines is perhaps a fitting end to a century of spectacular progress in mechanical engineering led in no small part by members of ASME International.

2 Fluid Mechanics Issues

2.1 Prologue. The rapid progress in fabricating and utilizing microelectromechanical systems during the last decade has not been matched by corresponding advances in our understanding of the unconventional physics involved in the operation and manufacture of small devices. Providing such understanding is crucial to designing, optimizing, fabricating and operating improved MEMS devices.

Fluid flows in small devices differ from those in macroscopic machines. The operation of MEMS-based ducts, nozzles, valves, bearings, turbomachines, etc., cannot always be predicted from conventional flow models such as the Navier-Stokes equations with no-slip boundary condition at a fluid-solid interface, as routinely and successfully applied for larger flow devices. Many questions have been raised when the results of experiments with microdevices could not be explained via traditional flow modeling. The pressure gradient in a long microduct was observed to be non-constant and the measured flowrate was higher than that predicted from the conventional continuum flow model. Load capacities of microbearings were diminished and electric currents needed to move micromotors were extraordinarily high. The dynamic response of micromachined accelerometers operating at atmospheric conditions was observed to be over-damped.

In the early stages of development of this exciting new field, the objective was to build MEMS devices as productively as possible. Microsensors were reading something, but not many researchers seemed to know exactly what. Microactuators were moving, but conventional modeling could not precisely predict their motion. After a decade of unprecedented progress in MEMS technology, perhaps the time is now ripe to take stock, slow down a bit and answer the many questions that arose. The ultimate aim of this long-term exercise is to achieve rational-design capability for useful microdevices and to be able to characterize definitively and with as little empiricism as possible the operations of microsensors and microactuators.

In dealing with fluid flow through microdevices, one is faced with the question of which model to use, which boundary condition to apply and how to proceed to obtain solutions to the problem at hand. Obviously surface effects dominate in small devices. The surface-to-volume ratio for a machine with a characteristic length of 1 m is 1 m^{-1}, while that for a MEMS device having a size of 1 μm is 10^6 m^{-1}. The million-fold increase in surface area relative to the mass of the minute device substantially affects the transport of mass, momentum and energy through the surface. The small length-scale of microdevices may invalidate the continuum approximation altogether. Slip flow, thermal creep, rarefaction, viscous dissipation, compressibility, intermolecular forces and other unconventional effects may have to be taken into account, preferably using only first principles such as conservation of mass, Newton's second law, conservation of energy, etc.

In this section, we discuss continuum as well as molecular-based flow models, and the choices to be made. Computing typical Reynolds, Mach and Knudsen numbers for the flow through a particular device is a good start to characterize the flow. For gases, microfluid mechanics has been studied by incorporating slip boundary conditions, thermal creep, viscous dissipation as well as compressibility effects into the continuum equations of motion. Molecular-based models have also been attempted for certain ranges of the operating parameters. Use is made of the well-developed kinetic theory of gases, embodied in the Boltzmann equation, and direct simulation methods such as Monte Carlo. Microfluid mechanics of liquids is more complicated. The molecules are much more closely packed at normal pressures and temperatures, and the attractive or cohesive potential between the liquid molecules as well as between the liquid and solid ones plays a dominant role if the characteristic length of the flow is sufficiently small. In cases when the traditional continuum model fails to provide accurate predictions or postdictions, expensive molecular dynamics simulations seem to be the only first-principle approach available to rationally characterize liquid flows in microdevices. Such simulations are not yet feasible for realistic flow extent or number of molecules. As a consequence, the microfluid mechanics of liquids is much less developed than that for gases.

2.2 Fluid Modeling. There are basically two ways of modeling a flow field. Either as the fluid really is, a collection of molecules, or as a continuum where the matter is assumed continuous and indefinitely divisible. The former modeling is subdivided into deterministic methods and probabilistic ones, while in the latter approach the velocity, density, pressure, etc., are defined at every point in space and time, and conservation of mass, energy and momentum lead to a set of nonlinear partial differential equations (Euler, Navier-Stokes, Burnett, etc.). Fluid modeling classification is depicted schematically in Fig. 2.

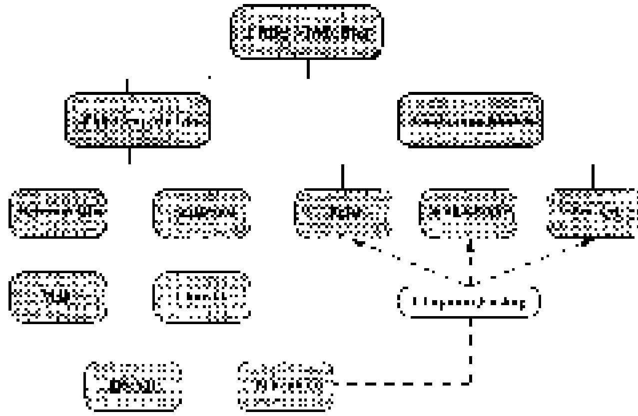

Fig. 2 Molecular and continuum flow models

The continuum model, embodied in the Navier-Stokes equations, is applicable to numerous flow situations. The model ignores the molecular nature of gases and liquids and regards the fluid as a continuous medium describable in terms of the spatial and temporal variations of density, velocity, pressure, temperature and other macroscopic flow quantities. For dilute gas flows near equilibrium, the Navier-Stokes equations are derivable from the molecularly-based Boltzmann equation, but can also be derived independently of that for both liquids and gases. In the case of direct derivation, some empiricism is necessary to close the resulting indeterminate set of equations. The continuum model is easier to handle mathematically (and is also more familiar to most fluid dynamists) than the alternative molecular models. Continuum models should therefore be used as long as they are applicable. Thus, careful considerations of the validity of the Navier-Stokes equations and the like are in order.

Basically, the continuum model leads to fairly accurate predictions as long as local properties such as density and velocity can be defined as averages over elements large compared with the microscopic structure of the fluid but small enough in comparison with the scale of the macroscopic phenomena to permit the use of differential calculus to describe them. Additionally, the flow must not be too far from thermodynamic equilibrium. The former condition is almost always satisfied, but it is the latter which usually restricts the validity of the continuum equations. As will be seen in Section 2.3, the continuum flow equations do not form a determinate set. The shear stress and heat flux must be expressed in terms of lower-order macroscopic quantities such as velocity and temperature, and the simplest (i.e., linear) relations are valid only when the flow is near thermodynamic equilibrium. Worse yet, the traditional no-slip boundary condition at a solid-fluid interface breaks down even before the linear stress-strain relation becomes invalid.

To be more specific, we temporarily restrict the discussion to gases where the concept of mean free path is well defined. Liquids are more problematic and we defer their discussion to Section 2.7. For gases, the mean free path $\mathcal{L}$ is the average distance traveled by molecules between collisions. For an ideal gas modeled as rigid spheres, the mean free path is related to temperature T and pressure p as follows

$$\mathcal{L} = \frac{1}{\sqrt{2}\pi n \sigma^2} = \frac{kT}{\sqrt{2}\pi p \sigma^2} \tag{1}$$

where n is the number density (number of molecules per unit volume), σ is the molecular diameter, and k is the Boltzmann constant.

The continuum model is valid when $\mathcal{L}$ is much smaller than a characteristic flow dimension L. As this condition is violated, the flow is no longer near equilibrium and the linear relation between stress and rate of strain and the no-slip velocity condition are no longer valid. Similarly, the linear relation between heat flux and temperature gradient and the no-jump temperature condition at a solid-fluid interface are no longer accurate when $\mathscr{L}$ is not much smaller than L.

The length-scale L can be some overall dimension of the flow, but a more precise choice is the scale of the gradient of a macroscopic quantity, as for example the density ρ,

$$L = \frac{\rho}{\left|\dfrac{\partial \rho}{\partial y}\right|} \tag{2}$$

The ratio between the mean free path and the characteristic length is known as the Knudsen number

$$\mathrm{Kn} = \frac{\mathscr{L}}{L} \tag{3}$$

and generally the traditional continuum approach is valid, albeit with modified boundary conditions, as long as $\mathrm{Kn} < 0.1$.

There are two more important dimensionless parameters in fluid mechanics, and the Knudsen number can be expressed in terms of those two. The Reynolds number is the ratio of inertial forces to viscous ones

$$\mathrm{Re} = \frac{v_o L}{\nu} \tag{4}$$

where v_o is a characteristic velocity, and ν is the kinematic viscosity of the fluid. The Mach number is the ratio of flow velocity to the speed of sound

$$\mathrm{Ma} = \frac{v_o}{a_o} \tag{5}$$

The Mach number is a dynamic measure of fluid compressibility and may be considered as the ratio of inertial forces to elastic ones. From the kinetic theory of gases, the mean free path is related to the viscosity as follows

$$\nu = \frac{\mu}{\rho} = \frac{1}{2} \mathscr{L} \bar{v}_m \tag{6}$$

where μ is the dynamic viscosity, and $\bar{v}_m$ is the mean molecular speed which is somewhat higher than the sound speed a_o,

$$\bar{v}_m = \sqrt{\frac{8}{\pi \gamma}}\, a_o \tag{7}$$

where γ is the specific heat ratio (i.e. the isentropic exponent). Combining Equations (3)–(7), we reach the required relation

$$\mathrm{Kn} = \sqrt{\frac{\pi \gamma}{2}} \frac{\mathrm{Ma}}{\mathrm{Re}} \tag{8}$$

In boundary layers, the relevant length-scale is the shear-layer thickness δ, and for laminar flows

$$\frac{\delta}{L} \sim \frac{1}{\sqrt{\mathrm{Re}}} \tag{9}$$

$$\mathrm{Kn} \sim \frac{\mathrm{Ma}}{\mathrm{Re}_\delta} \sim \frac{\mathrm{Ma}}{\sqrt{\mathrm{Re}}} \tag{10}$$

where Re_δ is the Reynolds number based on the freestream velocity v_o and the boundary layer thickness δ, and Re is based on v_o and the streamwise length-scale L.

Rarefied gas flows are in general encountered in flows in small geometries such as MEMS devices and in low-pressure applications such as high-altitude flying and high-vacuum gadgets. The local value of Knudsen number in a particular flow determines the degree of rarefaction and the degree of validity of the continuum model. The different Knudsen number regimes are determined empirically and are therefore only approximate for a particular flow geometry. The pioneering experiments in rarefied gas dynamics were conducted by Knudsen in 1909. In the limit of zero Knudsen number, the transport terms in the continuum momentum and energy equations are negligible and the Navier-Stokes equations then reduce to the inviscid Euler equations. Both heat conduction and viscous diffusion and dissipation are negligible, and the flow is then approximately isentropic (i.e., adiabatic and reversible) from the continuum viewpoint while the equivalent molecular viewpoint is that the velocity distribution function is everywhere of the local equilibrium or Maxwellian form. As Kn increases, rarefaction effects become more important, and eventually the continuum approach breaks down altogether. The different Knudsen number regimes are depicted in Fig. 3, and can be summarized as follows

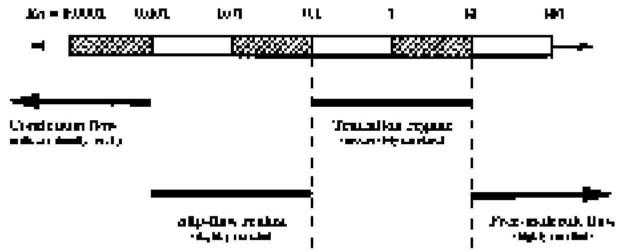

Fig. 3 Knudsen number regimes

Euler equations (neglect molecular diffusion):

$$\mathrm{Kn} \to 0 \ (\mathrm{Re} \to \infty)$$

Navier-Stokes equations with no-slip boundary conditions:

$$\mathrm{Kn} \le 10^{-3}$$

Navier-Stokes equations with slip boundary conditions:

$$10^{-3} \le \mathrm{Kn} \le 10^{-1}$$

Transition regime: $10^{-1} \le \mathrm{Kn} \le 10$

Free-molecule flow: $\mathrm{Kn} > 10$

We will return to those regimes in the following subsections.

As an example, consider air at standard temperature (T = 288 K) and pressure (p = 1.01 × 10^5 N/m^2). A cube one micron to the side contains 2.54 × 10^7 molecules separated by an average distance of 0.0034 micron. The gas is considered dilute if the ratio of this distance to the molecular diameter exceeds 7, and in the present example this ratio is 9, barely satisfying the dilute gas assumption. The mean free path computed from Eq. (1) is $\mathscr{L}$ = 0.065 μm. A microdevice with characteristic length of 1 μm would have Kn = 0.065, which is in the slip-flow regime. At lower pressures, the Knudsen number increases. For example, if the pressure is 0.1 atm and the temperature remains the same, Kn = 0.65 for the same 1-μm device, and the flow is then in the transition regime. There would still be over 2 million molecules in the same one-micron cube, and the average distance between them would be 0.0074 μm. The same device at 100 km altitude would have Kn = 3 × 10^4, well into the free-molecule flow regime. Knudsen number for the flow of a light gas like helium is about 3 times larger than that for air flow at otherwise the same conditions.

Consider a long microchannel where the entrance pressure is atmospheric and the exit conditions are near vacuum. As air goes down the duct, the pressure and density decrease while the velocity, Mach number and Knudsen number increase. The pressure drops to overcome viscous forces in the channel. If isothermal conditions prevail, density also drops and conservation of mass requires the flow to accelerate down the constant-area tube. (More likely the flow will be somewhere in between isothermal and adiabatic, Fanno flow. In that case both density and temperature decrease downstream, the former not as fast as in the isothermal case. None of that changes the qualitative arguments made in the example.) The fluid acceleration in turn affects the pressure gradient, resulting in a nonlinear pressure drop along the channel. The Mach number increases down the tube, limited only by choked-flow condition (Ma = 1). Additionally, the normal component of velocity is no longer zero. With lower density, the mean free path increases and Kn correspondingly increases. All flow regimes depicted in Fig. 3 may occur in the same tube: continuum with no-slip boundary conditions, slip-flow regime, transition regime and free-molecule flow. The air flow may also change from incompressible to compressible as it moves down the microduct. A similar scenario may take place if the entrance pressure is, say, 5 atm, while the exit is atmospheric. This deceivingly simple duct flow may in fact manifest every single complexity discussed in this section.

In the following six subsections, we discuss in turn the Navier-Stokes equations, compressibility effects, boundary conditions, molecular-based models, liquid flows and surface phenomena.

2.3 Continuum Model. We recall in this subsection the traditional conservation relations in fluid mechanics. No derivation is given here and the reader is referred to any advanced textbook in fluid mechanics, e.g., Batchelor (1967), Landau and Lifshitz (1987), Sherman (1990), Kundu (1990), and Panton (1996). In here, instead, we emphasize the precise assumptions needed to obtain a particular form of those equations. A continuum fluid implies that the derivatives of all the dependent variables exist in some reasonable sense. In other words, local properties such as density and velocity are defined as averages over elements large compared with the microscopic structure of the fluid but small enough in comparison with the scale of the macroscopic phenomena to permit the use of differential calculus to describe them. As mentioned earlier, such conditions are almost always met. For such fluids, and assuming the laws of non-relativistic mechanics hold, the conservation of mass, momentum and energy can be expressed at every point in space and time as a set of partial differential equations as follows

$$\frac{\partial \rho}{\partial t} + \frac{\partial}{\partial x_k}(\rho u_k) = 0 \tag{11}$$

$$\rho\left(\frac{\partial u_i}{\partial t} + u_k \frac{\partial u_i}{\partial x_k}\right) = \frac{\partial \sigma_{ki}}{\partial x_k} + \rho g_i \tag{12}$$

$$\rho\left(\frac{\partial e}{\partial t} + u_k \frac{\partial e}{\partial x_k}\right) = -\frac{\partial q_k}{\partial x_k} + \sigma_{ki}\frac{\partial u_i}{\partial x_k} \tag{13}$$

where ρ is the fluid density, u_k is an instantaneous velocity component (u, v, w), σ_{ki} is the second-order stress tensor (surface force per unit area), and g_i is the body force per unit mass, e is the internal energy, and q_k is the sum of heat flux vectors due to conduction and radiation. The independent variables are time t and the three spatial coordinates x_1, x_2 and x_3 or (x, y, z).

Equations (11), (12), and (13) constitute 5 differential equations for the 17 unknowns ρ, u_i, σ_{ki}, e, and q_k. Absent any body couples, the stress tensor is symmetric having only six independent components, which reduces the number of unknowns to 14. Obviously, the continuum flow equations do not form a determinate set. To close the conservation equations, relation between the stress tensor and deformation rate, relation between the heat flux vector and the temperature field and appropriate equations of state relating the different thermodynamic properties are needed. The stress-rate of strain relation and the heat flux-temperature relation are approximately linear if the flow is not too far from thermodynamic equilibrium. This is a phenomenological result but can be rigorously derived from the Boltzmann equation for a dilute gas assuming the flow is near equilibrium (see Section 2.6). For a Newtonian, isotropic, Fourier, ideal gas, for example, those relations read

$$\sigma_{ki} = -p\delta_{ki} + \mu\left(\frac{\partial u_i}{\partial x_k} + \frac{\partial u_k}{\partial x_i}\right) + \lambda\left(\frac{\partial u_j}{\partial x_j}\right)\delta_{ki} \tag{14}$$

$$q_i = -\kappa\frac{\partial T}{\partial x_i} + \text{Heat flux due to radiation} \tag{15}$$

$$de = c_v dT \quad \text{and} \quad p = \rho \mathcal{R} T \tag{16}$$

where p is the thermodynamic pressure, μ and λ are the first and second coefficients of viscosity, respectively, δ_{ki} is the unit second-order tensor (Kronecker delta), κ is the thermal conductivity, T is the temperature field, c_v is the specific heat at constant volume, and $\mathcal{R}$ is the gas constant which is given by the Boltzmann constant divided by the mass of an individual molecule ($k = m\mathcal{R}$). (Newtonian implies a linear relation between the stress tensor and the symmetric part of the deformation tensor (rate of strain tensor). The isotropy assumption reduces the 81 constants of proportionality in that linear relation to two constants. Fourier fluid is that for which the conduction part of the heat flux vector is linearly related to the temperature gradient, and again isotropy implies that the constant of proportionality in this relation is a single scalar.) The Stokes' hypothesis relates the first and second coefficients of viscosity thus $\lambda + \frac{2}{3}\mu = 0$, although the validity of this assumption for other than dilute, monatomic gases has occasionally been questioned (Gad-el-Hak, 1995). With the above constitutive relations and neglecting radiative heat transfer (a reasonable assumption when dealing with low to moderate temperatures since the radiative heat flux is proportional to T^4), Equations (11), (12), and (13), respectively, read

$$\frac{\partial \rho}{\partial t} + \frac{\partial}{\partial x_k}(\rho u_k) = 0 \tag{17}$$

$$\rho\left(\frac{\partial u_i}{\partial t} + u_k\frac{\partial u_i}{\partial x_k}\right) = -\frac{\partial p}{\partial x_i} + \rho g_i + \frac{\partial}{\partial x_k}\left[\mu\left(\frac{\partial u_i}{\partial x_k} + \frac{\partial u_k}{\partial x_i}\right) + \delta_{ki}\lambda\frac{\partial u_j}{\partial x_j}\right] \tag{18}$$

$$\rho c_v\left(\frac{\partial T}{\partial t} + u_k\frac{\partial T}{\partial x_k}\right) = \frac{\partial}{\partial x_k}\left(\kappa\frac{\partial T}{\partial x_k}\right) - p\frac{\partial u_k}{\partial x_k} + \phi \tag{19}$$

The three components of the vector equation (18) are the Navier-Stokes equations expressing the conservation of momentum for a Newtonian fluid. In the thermal energy equation (19), ϕ is the always positive (as required by the Second Law of thermodynamics) dissipation function expressing the irreversible conversion of mechanical energy to internal energy as a result of the deformation of a fluid element. The second term on the right-hand side of (19) is the reversible work done (per unit time) by the pressure as the volume of a fluid material element changes. For a Newtonian, isotropic fluid, the viscous dissipation rate is given by

$$\phi = \tfrac{1}{2}\mu\left(\frac{\partial u_i}{\partial x_k} + \frac{\partial u_k}{\partial x_i}\right)^2 + \lambda\left(\frac{\partial u_j}{\partial x_j}\right)^2 \tag{20}$$

There are now six unknowns, ρ, u_i, p and T, and the five coupled equations (17), (18), and (19) plus the equation of state relating pressure, density and temperature. These six equations together with sufficient number of initial and boundary conditions constitute a well-posed, albeit formidable, problem. The system of equations (17)–(19) is an excellent model for the laminar or turbulent flow of most fluids such as air and water under many circumstances, including high-speed gas flows for which the shock waves are thick relative to the mean free path of the molecules. (This condition is met if the shock Mach number is less than 2.)

Considerable simplification is achieved if the flow is assumed incompressible, usually a reasonable assumption provided that the characteristic flow speed is less than 0.3 of the speed of sound. (Although as will be demonstrated in the following subsection, there are circumstances when even a low-Mach-number flow should be treated as compressible.) The incompressibility assumption is readily satisfied for almost all liquid flows and many gas flows. In such cases, the density is assumed either a constant or a given function of temperature (or species concentration). (Within the so-called Boussinesq approximation, density variations have negligible effect on inertia but are retained in the buoyancy terms. The incompressible continuity equation is therefore used.) The governing equations for such flow are

$$\frac{\partial u_k}{\partial x_k} = 0 \tag{21}$$

$$\rho\left(\frac{\partial u_i}{\partial t} + u_k \frac{\partial u_i}{\partial x_k}\right) = -\frac{\partial p}{\partial x_i} + \frac{\partial}{\partial x_k}\left[\mu\left(\frac{\partial u_i}{\partial x_k} + \frac{\partial u_k}{\partial x_i}\right)\right] + \rho g_i \tag{22}$$

$$\rho c_p\left(\frac{\partial T}{\partial t} + u_k \frac{\partial T}{\partial x_k}\right) = \frac{\partial}{\partial x_k}\left(\kappa \frac{\partial T}{\partial x_k}\right) + \phi_{\text{incomp}} \tag{23}$$

where ϕ_{incomp} is the incompressible limit of Eq. (20). These are now five equations for the five dependent variables u_i, p and T. Note that the left-hand side of Eq. (23) has the specific heat at constant pressure c_p and not c_v. It is the convection of enthalpy—and not internal energy—that is balanced by heat conduction and viscous dissipation. This is the correct incompressible-flow limit—of a compressible fluid—as discussed in detail in Section 10.9 of Panton (1996); a subtle point perhaps but one that is frequently misinterpreted in textbooks. The system of equations (21)–(23) is coupled if either the viscosity or density depends on temperature, otherwise the energy equation is uncoupled from the continuity and momentum equations and can therefore be solved *after* the velocity and pressure fields are determined.

For both the compressible and the incompressible equations of motion, the transport terms are neglected away from solid walls in the limit of infinite Reynolds number ($\text{Kn} \to 0$). The fluid is then approximated as inviscid and non-conducting, and the corresponding equations read (for the compressible case)

$$\frac{\partial \rho}{\partial t} + \frac{\partial}{\partial x_k}(\rho u_k) = 0 \tag{24}$$

$$\rho\left(\frac{\partial u_i}{\partial t} + u_k \frac{\partial u_i}{\partial x_k}\right) = -\frac{\partial p}{\partial x_i} + \rho g_i \tag{25}$$

$$\rho c_v\left(\frac{\partial T}{\partial t} + u_k \frac{\partial T}{\partial x_k}\right) = -p \frac{\partial u_k}{\partial x_k} \tag{26}$$

The Euler equation (25) can be integrated along a streamline and the resulting Bernoulli's equation provides a direct relation between the velocity and pressure.

2.4 Compressibility. The issue of whether to consider the continuum flow compressible or incompressible seems to be rather straightforward, but is in fact full of potential pitfalls. If the local Mach number is less than 0.3, then the flow of a compressible fluid like air can—according to the conventional wisdom—be treated as incompressible. But the well-known Ma < 0.3 criterion is only a necessary not a sufficient one to allow treatment of the flow as approximately incompressible. In other words, there are situations where the Mach number can be exceedingly small while the flow is compressible. As is well documented in heat transfer textbooks, strong wall heating or cooling may cause the density to change sufficiently and the incompressible approximation to break down, even at low speeds. Less known is the situation encountered in some microdevices where the pressure may strongly change due to viscous effects even though the speeds may not be high enough for the Mach number to go above the traditional threshold of 0.3. Corresponding to the pressure changes would be strong density changes that must be taken into account when writing the continuum equations of motion. In this section, we systematically explain all situations relevant to MEMS where compressibility effects must be considered. (Two other situations where compressibility effects must also be considered are length-scales comparable to the scale height of the atmosphere and rapidly varying flows as in sound propagation (see Lighthill, 1963). Neither of these situations is likely to be encountered in microdevices.)

Let us rewrite the full continuity equation (11) as follows

$$\frac{D\rho}{Dt} + \rho \frac{\partial u_k}{\partial x_k} = 0 \tag{27}$$

where D/Dt is the substantial derivative $(\partial/\partial t + u_k \partial/\partial x_k)$, expressing changes following a fluid element. The proper criterion for the incompressible approximation to hold is that $(1/\rho)(D\rho/Dt)$ is vanishingly small. In other words, if density changes following a fluid particle are small, the flow is approximately incompressible. Density may change arbitrarily from one particle to another without violating the incompressible flow assumption. This is the case for example in the stratified atmosphere and ocean, where the variable-density/temperature/salinity flow is often treated as incompressible.

From the state principle of thermodynamics, we can express the density changes of a simple system in terms of changes in pressure and temperature,

$$\rho = \rho(p, T) \tag{28}$$

Using the chain rule of calculus,

$$\frac{1}{\rho}\frac{D\rho}{Dt} = \alpha \frac{Dp}{Dt} - \beta \frac{DT}{Dt} \tag{29}$$

where α and β are, respectively, the isothermal compressibility coefficient and the bulk expansion coefficient—two thermodynamic variables that characterize the fluid susceptibility to change of volume—which are defined by the following relations

$$\alpha(p, T) \equiv \frac{1}{\rho}\left.\frac{\partial \rho}{\partial p}\right|_T \tag{30}$$

$$\beta(p, T) \equiv -\frac{1}{\rho}\left.\frac{\partial \rho}{\partial T}\right|_p \tag{31}$$

For ideal gases, $\alpha = 1/p$, and $\beta = 1/T$. Note, however, that in the following arguments it will not be necessary to invoke the ideal gas assumption.

The flow must be treated as compressible if pressure and/or temperature changes are sufficiently strong. Equation (29) must of course be properly nondimensionalized before deciding whether a term is large or small. In here, we follow closely the procedure detailed in Panton (1996).

Consider first the case of adiabatic walls. Density is normalized with a reference value ρ_o, velocities with a reference speed v_o, spatial coordinates, and time with, respectively, L and L/v_o, the isothermal compressibility coefficient and bulk expansion coefficient with reference values α_o and β_o. The pressure is nondimensionalized with the inertial pressure-scale $\rho_o v_o^2$. This scale is twice the dynamic pressure, i.e., the pressure change as an inviscid fluid moving at the reference speed is brought to rest.

Temperature changes for the case of adiabatic walls result from the irreversible conversion of mechanical energy into internal energy via viscous dissipation. Temperature is therefore nondimensionalized as follows

$$T^* = \frac{T - T_o}{\left(\frac{\mu_o v_o^2}{\kappa_o}\right)} = \frac{T - T_o}{\mathrm{Pr}\left(\frac{v_o^2}{c_{p_o}}\right)} \tag{32}$$

where T_o is a reference temperature, μ_o, κ_o, and c_{p_o} are, respectively, reference viscosity, thermal conductivity and specific heat at constant pressure, and Pr is the reference Prandtl number, $(\mu_o c_{p_o})/\kappa_o$.

In the present formulation, the scaling used for pressure is based on the Bernoulli's equation, and therefore neglects viscous effects. This particular scaling guarantees that the pressure term in the momentum equation will be of the same order as the inertia term. The temperature scaling assumes that the conduction, convection and dissipation terms in the energy equation have the same order of magnitude. The resulting dimensionless form of Eq. (29) reads

$$\frac{1}{\rho^*}\frac{D\rho^*}{Dt^*} = \gamma_o \,\mathrm{Ma}^2\left\{\alpha^* \frac{Dp^*}{Dt^*} - \frac{\mathrm{Pr}\; B\beta^*}{A}\frac{DT^*}{Dt^*}\right\} \tag{33}$$

where the superscript * indicates a nondimensional quantity, Ma is the reference Mach number, and A and B are dimensionless constants defined by $A \equiv \alpha_o \rho_o c_{p_o} T_o$, and $B \equiv \beta_o T_o$. If the scaling is properly chosen, the terms having the * superscript in the right-hand side should be of order one, and the relative importance of such terms in the equations of motion is determined by the magnitude of the dimensionless parameter(s) appearing to their left, e.g. Ma, Pr, etc. Therefore, as $\mathrm{Ma}^2 \to 0$, temperature changes due to viscous dissipation are neglected (unless Pr is very large, as for example in the case of highly viscous polymers and oils). Within the same order of approximation, all thermodynamic properties of the fluid are assumed constant.

Pressure changes are also neglected in the limit of zero Mach number. Hence, for $\mathrm{Ma} < 0.3$ (i.e. $\mathrm{Ma}^2 < 0.09$), density changes following a fluid particle can be neglected and the flow can then be approximated as incompressible. (With an error of about 10% at $\mathrm{Ma} = 0.3$, 4% at $\mathrm{Ma} = 0.2$, 1% at $\mathrm{Ma} = 0.1$, and so on.) However, there is a caveat in this argument. Pressure changes due to inertia can indeed be neglected at small Mach numbers and this is consistent with the way we nondimensionalized the pressure term above. If, on the other hand, pressure changes are mostly due to viscous effects, as is the case for example in a long duct or a gas bearing, pressure changes may be significant even at low speeds (low Ma). In that case the term Dp^*/Dt^* in Eq. (33) is no longer of order one, and may be large regardless of the value of Ma. Density then may change significantly and the flow must be treated as compressible. Had pressure been nondimensionalized using the viscous scale ($\mu_o v_o/L$) instead of the inertial one ($\rho_o v_o^2$), the revised equation (33) would have Re^{-1} appearing explicitly in the first term in the right-hand side, accentuating the importance of this term when viscous forces dominate.

A similar result can be gleaned when the Mach number is interpreted as follows

$$\mathrm{Ma}^2 = \frac{v_o^2}{a_o^2} = v_o^2 \left.\frac{\partial \rho}{\partial p}\right|_s = \frac{\rho_o v_o^2}{\rho_o}\left.\frac{\partial \rho}{\partial p}\right|_s \sim \frac{\Delta p}{\rho_o}\frac{\Delta \rho}{\Delta p} = \frac{\Delta \rho}{\rho_o} \tag{34}$$

where s is the entropy. Again, the above equation assumes that pressure changes are inviscid, and therefore small Mach number means negligible pressure and density changes. In a flow dominated by viscous effects—such as that inside a microduct—density changes may be significant even in the limit of zero Mach number.

Identical arguments can be made in the case of isothermal walls. Here strong temperature changes may be the result of wall heating or cooling, even if viscous dissipation is negligible. The proper temperature scale in this case is given in terms of the wall temperature T_w and the reference temperature T_o as follows

$$\hat{T} = \frac{T - T_o}{T_w - T_o} \tag{35}$$

where $\hat{T}$ is the new dimensionless temperature. The nondimensional form of Eq. (29) now reads

$$\frac{1}{\rho^*}\frac{D\rho^*}{Dt^*} = \gamma_o \,\mathrm{Ma}^2\, \alpha^* \frac{Dp^*}{Dt^*} - \beta^* B\left(\frac{T_w - T_o}{T_o}\right)\frac{D\hat{T}}{Dt^*} \tag{36}$$

Here we notice that the temperature term is different from that in Eq. (33). Ma is no longer appearing in this term, and strong temperature changes, i.e., large $(T_w - T_o)/T_o$, may cause strong density changes regardless of the value of the Mach number. Additionally, the thermodynamic properties of the fluid are not constant but depend on temperature, and as a result, the continuity, momentum and energy equations are all coupled. The pressure term in Eq. (36), on the other hand, is exactly as it was in the adiabatic case and the same arguments made before apply: the flow should be considered compressible if $\mathrm{Ma} > 0.3$, or if pressure changes due to viscous forces are sufficiently large.

Experiments in gaseous microducts confirm the above arguments. For both low- and high-Mach-number flows, pressure gradients in long microchannels are non-constant, consistent with the compressible flow equations. Such experiments were conducted by, among others, Prud'homme et al. (1986), Pfahler et al. (1991), van den Berg et al. (1993), Liu et al. (1993; 1995), Pong et al. (1994), Harley et al. (1995), Piekos and Breuer (1996), Arkilic (1997), and Arkilic et al. (1995; 1997a; 1997b). Sample results will be presented in the following subsection.

There is one last scenario in which significant pressure and density changes may take place without viscous or inertial effects. That is the case of quasi-static compression/expansion of a gas in, for example, a piston-cylinder arrangement. The resulting compressibility effects are, however, compressibility of the fluid and not of the flow.

2.5 Boundary Conditions. The equations of motion described in Section 2.3 require a certain number of initial and boundary conditions for proper mathematical formulation of flow problems. In this subsection, we describe the boundary conditions at a fluid-solid interface. Boundary conditions in the inviscid flow theory pertain only to the velocity component normal to a solid surface. The highest spatial derivative of velocity in the inviscid equations of motion is first-order, and only one velocity boundary condition at the surface is admissible.

The normal velocity component at a fluid-solid interface is specified, and no statement can be made regarding the tangential velocity component. The normal-velocity condition simply states that a fluid-particle path cannot go through an impermeable wall. Real fluids are of course viscous and the corresponding momentum equation has second-order derivatives of velocity, thus requiring an additional boundary condition on the velocity component tangential to a solid surface.

Traditionally, the no-slip condition at a fluid-solid interface is enforced in the momentum equation and an analogous no-temperature-jump condition is applied in the energy equation. The notion underlying the no-slip/no-jump condition is that within the fluid there cannot be any finite discontinuities of velocity/temperature. Those would involve infinite velocity/temperature gradients and so produce infinite viscous stress/heat flux that would destroy the discontinuity in infinitesimal time. The interaction between a fluid particle and a wall is similar to that between neighboring fluid particles, and therefore no discontinuities are allowed at the fluid-solid interface either. In other words, the fluid velocity must be zero relative to the surface and the fluid temperature must equal to that of the surface. But strictly speaking those two boundary conditions are valid only if the fluid flow adjacent to the surface is in thermodynamic equilibrium. This requires an infinitely high frequency of collisions between the fluid and the solid surface. In practice, the no-slip/no-jump condition leads to fairly accurate predictions as long as $\mathrm{Kn} < 0.001$ (for gases). Beyond that, the collision frequency is simply not high enough to ensure equilibrium and a certain degree of tangential-velocity slip and temperature jump must be allowed. This is a case frequently encountered in MEMS flows, and we develop the appropriate relations in this subsection.

For both liquids and gases, the linear Navier boundary condition empirically relates the tangential velocity slip at the wall $\Delta u|_w$ to the local shear

$$\Delta u|_w = u_{\text{fluid}} - u_{\text{wall}} = L_s \left.\frac{\partial u}{\partial y}\right|_w \tag{37}$$

where L_s is the constant slip length, and $\partial u/\partial y|_w$ is the strain rate computed at the wall. In most practical situations, the slip length is so small that the no-slip condition holds. In MEMS applications, however, that may not be the case. Once again we defer the discussion of liquids to Section 2.7, and focus for now on gases.

Assuming isothermal conditions prevail, the above slip relation has been rigorously derived by Maxwell (1879) from considerations of the kinetic theory of dilute, monatomic gases. Gas molecules, modeled as rigid spheres, continuously strike and reflect from a solid surface, just as they continuously collide with each other. For an idealized perfectly smooth (at the molecular scale) wall, the incident angle exactly equals the reflected angle and the molecules conserve their tangential momentum and thus exert no shear on the wall. This is termed specular reflection and results in perfect slip at the wall. For an extremely rough wall, on the other hand, the molecules reflect at some random angle uncorrelated with their entry angle. This perfectly diffuse reflection results in zero tangential-momentum for the reflected fluid molecules to be balanced by a finite slip velocity in order to account for the shear stress transmitted to the wall. A force balance near the wall leads to the following expression for the slip velocity

$$u_{\text{gas}} - u_{\text{wall}} = \mathcal{L} \left.\frac{\partial u}{\partial y}\right|_w \tag{38}$$

where $\mathcal{L}$ is the mean free path. The right-hand side can be considered as the first term in an infinite Taylor series, sufficient if the mean free path is relatively small enough. The equation above states that significant slip occurs only if the mean velocity of the molecules varies appreciably over a distance of one mean free path. This is the case, for example, in vacuum applications and/or flow in microdevices. The number of collisions between the fluid molecules and the solid in those cases is not large enough for even an approximate flow equilibrium to be established. Furthermore, additional (nonlinear) terms in the Taylor series would be needed as $\mathcal{L}$ increases and the flow is further removed from the equilibrium state.

For real walls some molecules reflect diffusively and some reflect specularly. In other words, a portion of the momentum of the incident molecules is lost to the wall and a (typically smaller) portion is retained by the reflected molecules. The tangential-momentum-accommodation coefficient σ_v is defined as the fraction of molecules reflected diffusively. This coefficient depends on the fluid, the solid and the surface finish, and has been determined experimentally to be between 0.2–0.8 (Thomas and Lord, 1974; Seidl and Steiheil, 1974; Porodnov et al., 1974; Arkilic et al., 1997b; Arkilic, 1997), the lower limit being for exceptionally smooth surfaces while the upper limit is typical of most practical surfaces. The final expression derived by Maxwell for an isothermal wall reads

$$u_{\text{gas}} - u_{\text{wall}} = \frac{2-\sigma_v}{\sigma_v} \mathcal{L} \left.\frac{\partial u}{\partial y}\right|_w \tag{39}$$

For $\sigma_v = 0$, the slip velocity is unbounded, while for $\sigma_v = 1$, Eq. (39) reverts to (38).

Similar arguments were made for the temperature-jump boundary condition by von Smoluchowski (1898). For an ideal gas flow in the presence of wall-normal and tangential temperature gradients, the complete slip-flow and temperature-jump boundary conditions read

$$\begin{aligned} u_{\text{gas}} - u_{\text{wall}} &= \frac{2-\sigma_v}{\sigma_v} \frac{1}{\rho\sqrt{\dfrac{2\mathcal{R}T_{\text{gas}}}{\pi}}} \tau_w + \frac{3}{4} \frac{\Pr(\gamma-1)}{\gamma\rho\mathcal{R}T_{\text{gas}}} (-q_x)_w \\ &= \frac{2-\sigma_v}{\sigma_v} \mathcal{L} \left(\frac{\partial u}{\partial y}\right)_w + \frac{3}{4} \frac{\mu}{\rho T_{\text{gas}}} \left(\frac{\partial T}{\partial x}\right)_w \end{aligned} \tag{40}$$

$$\begin{aligned} T_{\text{gas}} - T_{\text{wall}} &= \frac{2-\sigma_T}{\sigma_T} \left[\frac{2(\gamma-1)}{(\gamma+1)}\right] \frac{1}{\rho\mathcal{R}\sqrt{\dfrac{2\mathcal{R}T_{\text{gas}}}{\pi}}} (-q_y)_w \\ &= \frac{2-\sigma_T}{\sigma_T} \left[\frac{2\gamma}{(\gamma+1)}\right] \frac{\mathcal{L}}{\Pr} \left(\frac{\partial T}{\partial y}\right)_w \end{aligned} \tag{41}$$

where x and y are the streamwise and normal coordinates, ρ and μ are respectively the fluid density and viscosity, $\mathcal{R}$ is the gas constant, T_{gas} is the temperature of the gas adjacent to the wall, T_{wall} is the wall temperature, τ_w is the shear stress at the wall, Pr is the Prandtl number, γ is the specific heat ratio, and $(q_x)_w$ and $(q_y)_w$ are, respectively, the tangential and normal heat flux at the wall.

The tangential-momentum-accommodation coefficient σ_v and the thermal-accommodation coefficient σ_T are given by, respectively,

$$\sigma_v = \frac{\tau_i - \tau_r}{\tau_i - \tau_w} \tag{42}$$

$$\sigma_T = \frac{dE_i - dE_r}{dE_i - dE_w} \tag{43}$$

where the subscripts i, r, and w stand for, respectively, incident, reflected and solid wall conditions, τ is a tangential momentum flux, and dE is an energy flux.

The second term in the right-hand side of Eq. (40) is the *thermal creep* which generates slip velocity in the fluid opposite to the direction of the tangential heat flux, i.e., flow in the direction of increasing temperature. At sufficiently high Knudsen numbers, streamwise temperature gradient in a conduit leads to a measurable pressure gradient along the tube. This may be the case in vacuum applications and MEMS devices. Thermal creep is the basis for the so-called Knudsen pump—a device with no moving parts—in which rarefied gas is hauled from one cold chamber to a hot one. (The terminology *Knudsen pump* has been used by, for example, Vargo and Muntz (1996), but according to Loeb (1961), the original experiments demonstrating such pump were carried out by Osborne Reynolds.) Clearly, such pump performs best at high Knudsen numbers, and is typically designed to operate in the free-molecule flow regime.

In dimensionless form, Eqs. (40) and (41), respectively, read

$$u^*_{\text{gas}} - u^*_{\text{wall}} = \frac{2-\sigma_v}{\sigma_v}\,\mathrm{Kn}\left(\frac{\partial u^*}{\partial y^*}\right)_w + \frac{3}{2\pi}\,\frac{(\gamma-1)}{\gamma}\,\frac{\mathrm{Kn}^2\,\mathrm{Re}}{\mathrm{Ec}}\left(\frac{\partial T^*}{\partial x^*}\right)_w \tag{44}$$

$$T^*_{\text{gas}} - T^*_{\text{wall}} = \frac{2-\sigma_T}{\sigma_T}\left[\frac{2\gamma}{(\gamma+1)}\right]\frac{\mathrm{Kn}}{\mathrm{Pr}}\left(\frac{\partial T^*}{\partial y^*}\right)_w \tag{45}$$

where the superscript * indicates dimensionless quantity, Kn is the Knudsen number, Re is the Reynolds number, and Ec is the Eckert number defined by

$$\mathrm{Ec} = \frac{v_o^2}{c_p \Delta T} = (\gamma - 1)\,\frac{T_o}{\Delta T}\,\mathrm{Ma}^2 \tag{46}$$

where v_o is a reference velocity, $\Delta T = (T_{\text{gas}} - T_o)$, and T_o is a reference temperature. Note that very low values of σ_v and σ_T lead to substantial velocity slip and temperature jump even for flows with small Knudsen number.

The first term in the right-hand side of Eq. (44) is first-order in Knudsen number, while the thermal creep term is second-order, meaning that the creep phenomenon is potentially significant at large values of the Knudsen number. Equation (45) is first-order in Kn. Using Eqs. (8) and (46), the thermal creep term in Eq. (44) can be rewritten in terms of ΔT and Reynolds number. Thus,

$$u^*_{\text{gas}} - u^*_{\text{wall}} = \frac{2-\sigma_v}{\sigma_v}\,\mathrm{Kn}\left(\frac{\partial u^*}{\partial y^*}\right)_w + \frac{3}{4}\,\frac{\Delta T}{T_o}\,\frac{1}{\mathrm{Re}}\left(\frac{\partial T^*}{\partial x^*}\right)_w \tag{47}$$

It is clear that large temperature changes along the surface or low Reynolds numbers lead to significant thermal creep.

The continuum Navier-Stokes equations with no-slip/no-temperature jump boundary conditions are valid as long as the Knudsen number does not exceed 0.001. First-order slip/temperature-jump boundary conditions should be applied to the Navier-Stokes equations in the range of $0.001 < \mathrm{Kn} < 0.1$. The transition regime spans the range of $0.1 < \mathrm{Kn} < 10$, and second-order or higher slip/temperature-jump boundary conditions are applicable there. Note, however, that the Navier-Stokes equations are first-order accurate in Kn as will be shown in Section 2.6, and are themselves not valid in the transition regime. Either higher-order continuum equations, e.g., Burnett equations, should be used there or molecular modeling should be invoked, abandoning the continuum approach altogether.

For isothermal walls, Beskok (1994) derived a higher-order slip-velocity condition as follows

$$u_{\text{gas}} - u_{\text{wall}} = \frac{2-\sigma_v}{\sigma_v}\left[\mathcal{L}\left(\frac{\partial u}{\partial y}\right)_w + \frac{\mathcal{L}^2}{2!}\left(\frac{\partial^2 u}{\partial y^2}\right)_w + \frac{\mathcal{L}^3}{3!}\left(\frac{\partial^3 u}{\partial y^3}\right)_w + \ldots\right] \tag{48}$$

Attempts to implement the above slip condition in numerical simulations are rather difficult. Second-order and higher derivatives of velocity cannot be computed accurately near the wall. Based on asymptotic analysis, Beskok (1996) and Beskok and Karniadakis (1994; 1998) proposed the following alternative higher-order boundary condition for the tangential velocity, including the thermal creep term,

$$u^*_{\text{gas}} - u^*_{\text{wall}} = \frac{2-\sigma_v}{\sigma_v}\,\frac{\mathrm{Kn}}{1-b\,\mathrm{Kn}}\left(\frac{\partial u^*}{\partial y^*}\right)_w + \frac{3}{2\pi}\,\frac{(\gamma-1)}{\gamma}\,\frac{\mathrm{Kn}^2\,\mathrm{Re}}{\mathrm{Ec}}\left(\frac{\partial T^*}{\partial x^*}\right)_w \tag{49}$$

where b is a high-order slip coefficient determined from the presumably known no-slip solution, thus avoiding the computational difficulties mentioned above. If this high-order slip coefficient is chosen as $b = u''_w/2u'_w$, where the prime denotes derivative with respect to y and the velocity is computed from the no-slip Navier-Stokes equations, Eq. (49) becomes second-order accurate in Knudsen number. Beskok's procedure can be extended to third- and higher-orders for both the slip-velocity and thermal creep terms.

Similar arguments can be applied to the temperature-jump boundary condition, and the resulting Taylor series reads in dimensionless form (Beskok, 1996),

$$T^*_{\text{gas}} - T^*_{\text{wall}} = \frac{2-\sigma_T}{\sigma_T}\left[\frac{2\gamma}{(\gamma+1)}\right]\frac{1}{\mathrm{Pr}}\left[\mathrm{Kn}\left(\frac{\partial T^*}{\partial y^*}\right)_w + \frac{\mathrm{Kn}^2}{2!}\left(\frac{\partial^2 T^*}{\partial y^{*2}}\right)_w + \ldots\right] \tag{50}$$

Again, the difficulties associated with computing second- and higher-order derivatives of temperature are alleviated using an identical procedure to that utilized for the tangential velocity boundary condition.

Several experiments in low-pressure macroducts or in microducts confirm the necessity of applying slip boundary condition at sufficiently large Knudsen numbers. Among them are those conducted by Knudsen (1909), Pfahler at al. (1991), Tison (1993), Liu et al. (1993; 1995), Pong et al. (1994), Arkilic et al. (1995), Harley et al. (1995), and Shih et al. (1995; 1996). The experiments are complemented by the numerical simulations carried out by Beskok (1994; 1996), Beskok and Karniadakis (1994; 1998), and Beskok et al. (1996). Here we present selected examples of the experimental and numerical results.

Tison (1993) conducted pipe flow experiments at very low pressures. His pipe has a diameter of 2 mm and a length-to-diameter ratio of 200. Both inlet and outlet pressures were varied to yield Knudsen number in the range of $\mathrm{Kn} = 0-200$. Figure 4 shows the variation of mass flowrate as a function of $(p_i^2 - p_o^2)$, where p_i is the inlet pressure and p_o is the outlet pressure. (The original data in this figure were acquired by S. A. Tison and plotted by Beskok et al. (1996).) The pressure drop in this rarefied pipe flow is nonlinear, characteristic of low-Reynolds-number, compressible flows. Three distinct flow regimes are identified: (1) slip flow regime, $0 < \mathrm{Kn} < 0.6$; (2) transition regime, $0.6 < \mathrm{Kn} < 17$, where the mass flowrate is almost constant as the pressure changes; and (3) free-molecule flow, $\mathrm{Kn} > 17$. Note that the demarkation between these three re-

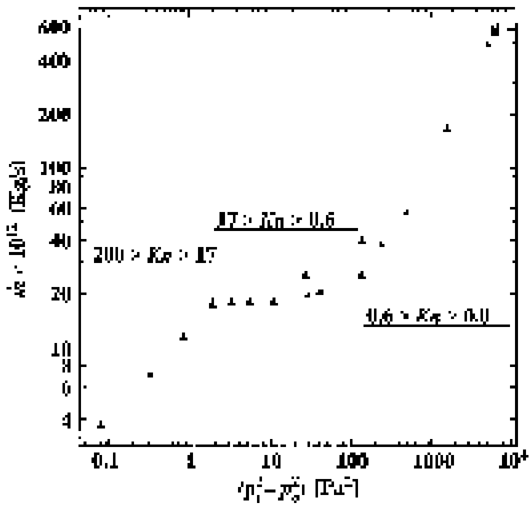

Fig. 4 Variation of mass flowrate as a function of $(p_i^2 - p_o^2)$. Original data acquired by S. A. Tison and plotted by Beskok et al. (1996).

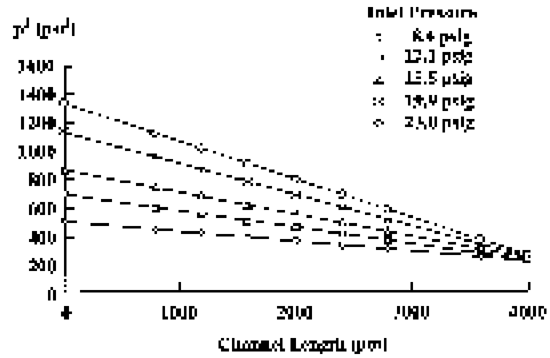

Fig. 6 Pressure distribution of nitrous oxide in a microduct. From Shih et al. (1996).

gimes is slightly different from that mentioned in Section 2.2. As stated, the different Knudsen number regimes are determined empirically and are therefore only approximate for a particular flow geometry.

Shih et al. (1995) conducted their experiments in a microchannel using helium as a fluid. The inlet pressure varied but the duct exit was atmospheric. Microsensors where fabricated in-situ along their MEMS channel to measure the pressure. Figure 5 shows their measured mass flowrate versus the inlet pressure. The data are compared to the no-slip solution and the slip solution using three different values of the tangential-momentum-accommodation coefficient, 0.8, 0.9 and 1.0. The agreement is reasonable with the case $\sigma_v = 1.0$, indicating perhaps that the channel used by Shih et al. was quite rough on the molecular scale. In a second experiment (Shih et al., 1996), nitrous oxide was used as the fluid. The square of the pressure distribution along the channel is plotted in Fig. 6 for five different inlet pressures. The experimental data (symbols) compare well with the theoretical predictions (solid lines). Again, the nonlinear pressure drop shown indicates that the gas flow is compressible.

Arkilic (1997) provided an elegant analysis of the compressible, rarefied flow in a microchannel. The results of his theory are compared to the experiments of Pong et al. (1994) in Fig. 7. The dotted line is the incompressible flow solution, where the pressure is predicted to drop linearly with streamwise distance. The dashed line is the compressible flow solution that neglects rarefaction effects (assumes Kn = 0). Finally, the solid line is the theoretical result that takes into account both compressibility and rarefaction via slip-flow boundary condition computed at the exit Knudsen number of Kn = 0.06. That theory compares most favorably with the experimental data. In the compressible flow through the constant-area duct, density decreases and thus velocity increases in the streamwise direction. As a result, the pressure distribution is nonlinear with negative curvature. A moderate Knudsen number (i.e. moderate slip) actually diminishes, albeit rather weakly, this curvature. Thus, compressibility and rarefaction effects lead to opposing trends, as pointed out by Beskok et al. (1996).

2.6 Molecular-Based Models. In the continuum models discussed in Section 2.3, the macroscopic fluid properties are the dependent variables while the independent variables are the three spatial coordinates and time. The molecular models recognize the fluid as a myriad of discrete particles: molecules, atoms, ions and electrons. The goal here is to determine the position, velocity and state of all particles at all times. The molecular approach is either deterministic or probabilistic (refer to Fig. 2). Provided that there is a sufficient number of microscopic particles within the smallest significant volume of a flow, the macroscopic properties at any location in the flow can then be computed from the discrete-particle information by a suitable averaging or weighted averaging process. The present subsection discusses molecular-based models and their relation to the continuum models previously considered.

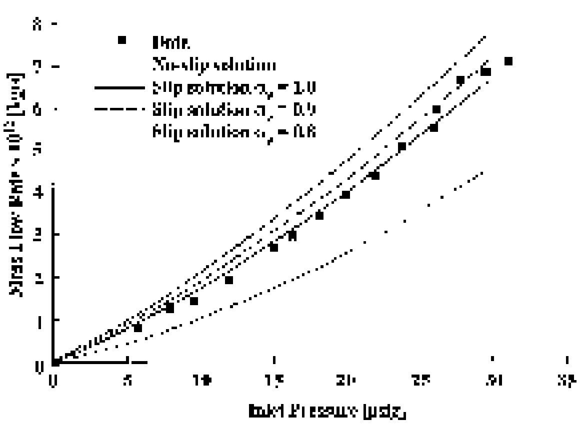

Fig. 5 Mass flowrate versus inlet pressure in a microchannel. From Shih et al. (1995).

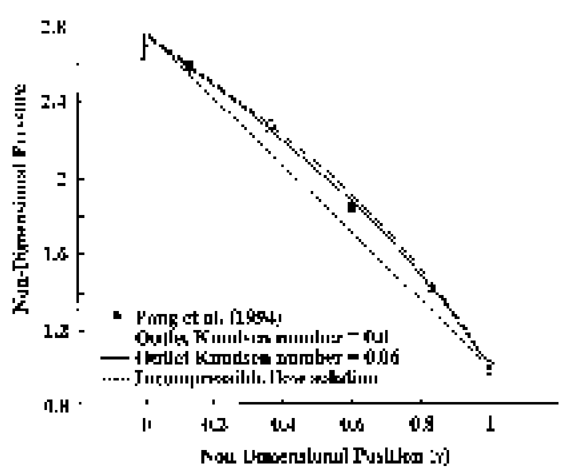

Fig. 7 Pressure distribution in a long microchannel. The symbols are experimental data while the solid lines are different theoretical predictions. From Arkilic (1997).

The most fundamental of the molecular models is a deterministic one. The motion of the molecules are governed by the laws of classical mechanics, although, at the expense of greatly complicating the problem, the laws of quantum mechanics can also be considered in special circumstances. The modern molecular dynamics computer simulations (MD) have been pioneered by Alder and Wainwright (1957; 1958; 1970) and reviewed by Ciccotti and Hoover (1986), Allen and Tildesley (1987), Haile (1993), and Koplik and Banavar (1995). The simulation begins with a set of N molecules in a region of space, each assigned a random velocity corresponding to a Boltzmann distribution at the temperature of interest. The interaction between the particles is prescribed typically in the form of a two-body potential energy and the time evolution of the molecular positions is determined by integrating Newton's equations of motion. Because MD is based on the most basic set of equations, it is valid in principle for any flow extent and any range of parameters. The method is straightforward in principle but there are two hurdles: choosing a proper and convenient potential for particular fluid and solid combinations, and the colossal computer resources required to simulate a reasonable flow field extent.

For purists, the former difficulty is a sticky one. There is no totally rational methodology by which a convenient potential can be chosen. Part of the art of MD is to pick an appropriate potential and validate the simulation results with experiments or other analytical/computational results. A commonly used potential between two molecules is the generalized Lennard-Jones 6-12 potential, to be used in Section 2.7 and further discussed in Section 2.8.

The second difficulty, and by far the most serious limitation of molecular dynamics simulations, is the number of molecules N that can realistically be modeled on a digital computer. Since the computation of an element of trajectory for any particular molecule requires consideration of all other molecules as potential collision partners, the amount of computation required by the MD method is proportional to N^2. Some saving in computer time can be achieved by cutting off the weak tail of the potential (see Fig. 12) at, say, $r_c = 2.5\sigma$, and shifting the potential by a linear term in r so that the force goes smoothly to zero at the cutoff. As a result, only nearby molecules are treated as potential collision partners, and the computation time for N molecules no longer scales with N^2.

The state of the art of molecular dynamics simulations in the 1990s is such that with a few hours of CPU time, general purpose supercomputers can handle around 10,000 molecules. At enormous expense, the fastest parallel machine available can simulate around 1 million particles. Because of the extreme diminution of molecular scales, the above translates into regions of liquid flow of about 0.01 μm (100 Å) in linear size, over time intervals of around 0.001 μs, just enough for continuum behavior to set in, for simple molecules. To simulate 1 s of real time for complex molecular interactions, e.g., including vibration modes, reorientation of polymer molecules, collision of colloidal particles, etc., requires unrealistic CPU time measured in thousands of years.

MD simulations are highly inefficient for dilute gases where the molecular interactions are infrequent. The simulations are more suited for dense gases and liquids. Clearly, molecular dynamics simulations are reserved for situations where the continuum approach or the statistical methods are inadequate to compute from first principles important flow quantities. Slip boundary conditions for liquid flows in extremely small devices is such a case as will be discussed in Section 2.7.

An alternative to the deterministic molecular dynamics is the statistical approach where the goal is to compute the probability of finding a molecule at a particular position and state. If the appropriate conservation equation can be solved for the probability distribution, important statistical properties such as the mean number, momentum or energy of the molecules within an element of volume can be computed from a simple weighted averaging. In a practical problem, it is such average quantities that concern us rather than the detail for every single molecule. Clearly, however, the accuracy of computing average quantities, via the statistical approach, improves as the number of molecules in the sampled volume increases. The kinetic theory of dilute gases is well advanced, but that for dense gases and liquids is much less so due to the extreme complexity of having to include multiple collisions and intermolecular forces in the theoretical formulation. The statistical approach is well covered in books such as those by Kennard (1938), Hirschfelder et al. (1954), Schaaf and Chambré (1961), Vincenti and Kruger (1965), Kogan (1969), Chapman and Cowling (1970), Cercignani (1988), and Bird (1994), and review articles such as those by Kogan (1973), Muntz (1989), and Oran et al. (1998).

In the statistical approach, the fraction of molecules in a given location and state is the sole dependent variable. The independent variables for monatomic molecules are time, the three spatial coordinates and the three components of molecular velocity. Those describe a six-dimensional phase space. (The evolution equation of the probability distribution is considered, hence time is the 7th independent variable.) For diatomic or polyatomic molecules, the dimension of phase space is increased by the number of internal degrees of freedom. Orientation adds an extra dimension for molecules which are not spherically symmetric. Finally, for mixtures of gases, separate probability distribution functions are required for each species. Clearly, the complexity of the approach increases dramatically as the dimension of phase space increases. The simplest problems are, for example, those for steady, one-dimensional flow of a simple monatomic gas.

To simplify the problem we restrict the discussion here to monatomic gases having no internal degrees of freedom. Furthermore, the fluid is restricted to dilute gases and molecular chaos is assumed. The former restriction requires the average distance between molecules δ to be an order of magnitude larger than their diameter σ. That will almost guarantee that all collisions between molecules are binary collisions, avoiding the complexity of modeling multiple encounters. (Dissociation and ionization phenomena involve triple collisions and therefore require separate treatment.) The molecular chaos restriction improves the accuracy of computing the macroscopic quantities from the microscopic information. In essence, the volume over which averages are computed has to have sufficient number of molecules to reduce statistical errors. It can be shown that computing macroscopic flow properties by averaging over a number of molecules will result in statistical fluctuations with a standard deviation of approximately 0.1% if one million molecules are used and around 3% if one thousand molecules are used. The molecular chaos limit requires the length-scale L for the averaging process to be at least 100 times the average distance between molecules (i.e., typical averaging over at least one million molecules).

Figure 8, adapted from Bird (1994), shows the limits of validity of the dilute gas approximation ($\delta/\sigma > 7$), the continuum approach (Kn < 0.1, as discussed previously in Section 2.2), and the neglect of statistical fluctuations ($L/\delta > 100$). Using a molecular diameter of $\sigma = 4 \times 10^{-10}$ m as an example, the three limits are conveniently expressed as functions of the normalized gas density ρ/ρ_o or number density n/n_o, where the reference densities ρ_o and n_o are computed at standard conditions. All three limits are straight lines in the log-log plot of L versus ρ/ρ_o, as depicted in Figure 8. Note the shaded triangular wedge inside which both the Boltzmann and Navier-Stokes equations are valid. Additionally, the lines describing the three limits very nearly intersect at a single point. As a consequence, the continuum breakdown limit always lies between the dilute gas limit and the limit for molecular chaos. As density or characteristic dimension is reduced in a dilute gas, the Navier-Stokes model breaks down before the level of statistical fluctuations becomes significant. In a dense gas, on the other hand, signifi-

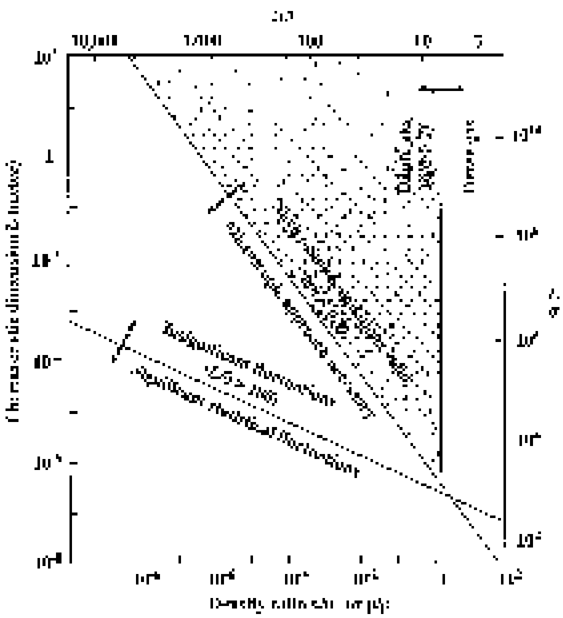

Fig. 8 Effective limits of different flow models. From Bird (1994).

cant fluctuations may be present even when the Navier-Stokes model is still valid.

The starting point in statistical mechanics is the Liouville equation which expresses the conservation of the N-particle distribution function in $6N$-dimensional phase space (three positions and three velocities for each molecule of a monatomic gas with no internal degrees of freedom), where N is the number of particles under consideration. Considering only external forces which do not depend on the velocity of the molecules (this excludes Lorentz forces, for example), the Liouville equation for a system of N mass points reads

$$\frac{\partial \mathcal{F}}{\partial t} + \sum_{k=1}^{N} \boldsymbol{\xi}_k \cdot \frac{\partial \mathcal{F}}{\partial \mathbf{x}_k} + \sum_{k=1}^{N} \mathbf{F}_k \cdot \frac{\partial \mathcal{F}}{\partial \boldsymbol{\xi}_k} = 0 \tag{51}$$

where $\mathcal{F}$ is the probability of finding a molecule at a particular point in phase space, t is time, $\boldsymbol{\xi}_k$ is the three-dimensional velocity vector for the kth molecule, $\mathbf{x}_k$ is the three-dimensional position vector for the kth molecule, and $\mathbf{F}$ is the external force vector. Note that the dot product in the above equation is carried out over each of the three components of the vectors $\boldsymbol{\xi}$, $\mathbf{x}$, and $\mathbf{F}$, and that the summation is over all molecules. Obviously such an equation is not tractable for realistic number of particles.

A hierarchy of reduced distribution functions may be obtained by repeated integration of the Liouville equation above. The final equation in the hierarchy is for the single particle distribution which also involves the two-particle distribution function. Assuming molecular chaos, that final equation becomes a closed one (i.e., one equation in one unknown), and is known as the Boltzmann equation, the fundamental relation of the kinetic theory of gases. That final equation in the hierarchy is the only one which carries any hope of obtaining analytical solutions.

A simpler direct derivation of the Boltzmann equation is provided by Bird (1994). For monatomic gas molecules in binary collisions, the integro-differential Boltzmann equation reads

$$\frac{\partial(nf)}{\partial t} + \xi_j \frac{\partial(nf)}{\partial x_j} + F_j \frac{\partial(nf)}{\partial \xi_j} = J(f, f^*), \quad j = 1, 2, 3 \tag{52}$$

where nf is the product of the number density and the normalized velocity distribution function ($dn/n = f\,\mathbf{d}\boldsymbol{\xi}$), x_j and ξ_j are, respectively, the coordinates and speeds of a molecule (constituting, together with time, the seven independent variables of the single-dependent-variable equation), F_j is a known external force, and $J(f, f^*)$ is the nonlinear collision integral that describes the net effect of populating and depopulating collisions on the distribution function. The collision integral is the source of difficulty in obtaining analytical solutions to the Boltzmann equation, and is given by

$$J(f, f^*) = \int_{-\infty}^{\infty} \int_{0}^{4\pi} n^2 (f^* f_1^* - f f_1) \boldsymbol{\xi}_r \sigma d\Omega (d\boldsymbol{\xi})_1 \tag{53}$$

where the superscript * indicates post-collision values, f and f_1 represent two different molecules, $\boldsymbol{\xi}_r$ is the relative speed between two molecules, σ is the molecular cross-section, Ω is the solid angle, and $d\boldsymbol{\xi} = d\xi_1 d\xi_2 d\xi_3$.

Once a solution for f is obtained, macroscopic quantities such as density, velocity, temperature, etc., can be computed from the appropriate weighted integral of the distribution function. For example,

$$\rho = mn = m \int (nf) d\boldsymbol{\xi} \tag{54}$$

$$u_i = \int \xi_i f d\boldsymbol{\xi} \tag{55}$$

$$\tfrac{3}{2} kT = \int \frac{1}{2} m \xi_i \xi_i f d\boldsymbol{\xi} \tag{56}$$

If the Boltzmann equation is nondimensionalized with a characteristic length L and characteristic speed $[2(k/m)T]^{1/2}$, where k is the Boltzmann constant, m is the molecular mass, and T is temperature, the inverse Knudsen number appears explicitly in the right-hand side of the equation as follows

$$\frac{\partial \hat{f}}{\partial \hat{t}} + \hat{\xi}_j \frac{\partial \hat{f}}{\partial \hat{x}_j} + \hat{F}_j \frac{\partial \hat{f}}{\partial \hat{\xi}_j} = \frac{1}{\text{Kn}} \hat{J}(\hat{f}, \hat{f}^*), \quad j = 1, 2, 3 \tag{57}$$

where the superscript ˆ represents a dimensionless variable, and $\hat{f}$ is nondimensionalized using a reference number density n_o.

The five conservation equations for the transport of mass, momentum, and energy can be derived by multiplying the Boltzmann equation above by, respectively, the molecular mass, momentum and energy, then integrating over all possible molecular velocities. Subject to the restrictions of dilute gas and molecular chaos stated earlier, the Boltzmann equation is valid for all ranges of Knudsen number from 0 to ∞. Analytical solutions to this equation for arbitrary geometries are difficult mostly because of the nonlinearity of the collision integral. Simple models of this integral have been proposed to facilitate analytical solutions; see, for example, Bhatnagar et al. (1954).

There are two important asymptotes to Eq. (57). First, as $\text{Kn} \rightarrow \infty$, molecular collisions become unimportant. This is the free-molecule flow regime depicted in Fig. 3 for $\text{Kn} > 10$, where the only important collision is that between a gas molecule and the solid surface of an obstacle or a conduit. Analytical solutions are then possible for simple geometries, and numerical simulations for complicated geometries are straightforward once the surface-reflection characteristics are accurately modeled. Second, as $\text{Kn} \rightarrow 0$, collisions become important and the flow approaches the continuum regime of conventional fluid dynamics. The Second Law specifies a tendency for thermodynamic systems to revert to equilibrium state, smoothing out any discontinuities in macroscopic flow quantities. The number of molecular collisions in the limit $\text{Kn} \rightarrow 0$ is so large that the flow approaches the equilibrium state in a time short compared to the macroscopic time-scale. For example, for air at standard conditions ($T = 288$ K; $p = 1$ atm), each molecule experiences, on the average, 10 collisions per nanosecond and travels

1 micron in the same time period. Such a molecule has already *forgotten* its previous state after 1 ns. In a particular flow field, if the macroscopic quantities vary little over a distance of 1 μm or over a time interval of 1 ns, the flow of STP air is near equilibrium.

At Kn = 0, the velocity distribution function is everywhere of the local equilibrium or Maxwellian form:

$$\hat{f}^{(0)} = \frac{n}{n_o} \pi^{-3/2} \exp[-(\hat{\xi} - \hat{u})^2] \tag{58}$$

where $\hat{\xi}$ and $\hat{u}$ are, respectively, the dimensionless speeds of a molecule and of the flow. In this Knudsen number limit, the velocity distribution of each element of the fluid instantaneously adjusts to the equilibrium thermodynamic state appropriate to the local macroscopic properties as this molecule moves through the flow field. From the continuum viewpoint, the flow is isentropic and heat conduction and viscous diffusion and dissipation vanish from the continuum conservation relations.

The Chapman-Enskog theory attempts to solve the Boltzmann equation by considering a small perturbation of $\hat{f}$ from the equilibrium Maxwellian form. For small Knudsen numbers, the distribution function can be expanded in terms of Kn in the form of a power series

$$\hat{f} = \hat{f}^{(0)} + \mathrm{Kn}\, \hat{f}^{(1)} + \mathrm{Kn}^2 \hat{f}^{(2)} + \ldots \tag{59}$$

By substituting the above series in the Boltzmann equation (57) and equating terms of equal order, the following recurrent set of integral equations result:

$$\hat{J}(\hat{f}^{(0)}, \hat{f}^{(0)}) = 0,$$
$$\hat{J}(\hat{f}^{(0)}, \hat{f}^{(1)}) = \frac{\partial \hat{f}^{(0)}}{\partial \hat{t}} + \hat{\xi}_j \frac{\partial \hat{f}^{(0)}}{\partial \hat{x}_j} + \hat{F}_j \frac{\partial \hat{f}^{(0)}}{\partial \hat{\xi}_j}, \ldots \tag{60}$$

The first integral is nonlinear and its solution is the local Maxwellian distribution, Eq. (58). The distribution functions $\hat{f}^{(1)}$, $\hat{f}^{(2)}$, etc., each satisfies an inhomogeneous linear equation whose solution leads to the transport terms needed to close the continuum equations appropriate to the particular level of approximation. The continuum stress tensor and heat flux vector can be written in terms of the distribution function, which in turn can be specified in terms of the macroscopic velocity and temperature and their derivatives (Kogan, 1973). The zeroth-order equation yields the Euler equations, the first-order equation results in the linear transport terms of the Navier-Stokes equations, the second-order equation gives the nonlinear transport terms of the Burnett equations, and so on. Keep in mind, however, that the Boltzmann equation as developed in this subsection is for a monatomic gas. This excludes the all important air which is composed largely of diatomic nitrogen and oxygen.

As discussed in Sections 2.2, 2.3, and 2.5, the Navier-Stokes equations can and should be used up to a Knudsen number of 0.1. Beyond that, the transition flow regime commences ($0.1 < \mathrm{Kn} < 10$). In this flow regime, the molecular mean free path for a gas becomes significant relative to a characteristic distance for important flow-property changes to take place. The Burnett equations can be used to obtain analytical/numerical solutions for at least a portion of the transition regime for a monatomic gas, although their complexity have precluded much results for realistic geometries. There is also a certain degree of uncertainty about the proper boundary conditions to use with the continuum Burnett equations, and experimental validation of the results have been very scarce. Additionally, as the gas flow further departs from equilibrium, the bulk viscosity ($=\lambda + \frac{2}{3}\mu$, where λ is the second coefficient of viscosity) is no longer zero, and the Stokes' hypothesis no longer holds (see Gad-el-Hak, 1995, for an interesting summary of the issue of bulk viscosity).

In the transition regime, the molecularly-based Boltzmann equation cannot easily be solved either, unless the nonlinear collision integral is simplified. So, clearly the transition regime is one of dire need of alternative methods of solution. MD simulations as mentioned earlier are not suited for dilute gases. The best approach for the transition regime right now is the direct simulation Monte Carlo (DSMC) method developed by Bird (1963; 1965; 1976; 1978; 1994) and briefly described below. Some recent reviews of DSMC include those by Muntz (1989), Cheng (1993), Cheng and Emmanuel (1995), and Oran et al. (1998). The mechanics as well as the history of the DSMC approach and its ancestors are well described in the book by Bird (1994).

Unlike molecular dynamics simulations, DSMC is a statistical computational approach to solving rarefied gas problems. Both approaches treat the gas as discrete particles. Subject to the dilute gas and molecular chaos assumptions, the direct simulation Monte Carlo method is valid for all ranges of Knudsen number, although it becomes quite expensive for $\mathrm{Kn} < 0.1$. Fortunately, this is the continuum regime where the Navier-Stokes equations can be used analytically or computationally. DSMC is therefore ideal for the transition regime ($0.1 < \mathrm{Kn} < 10$), where the Boltzmann equation is difficult to solve. The Monte Carlo method is, like its name sake, a random number strategy based directly on the physics of the individual molecular interactions. The idea is to track a large number of randomly selected, statistically representative particles, and to use their motions and interactions to modify their positions and states. The primary approximation of the direct simulation Monte Carlo method is to uncouple the molecular motions and the intermolecular collisions over small time intervals. A significant advantage of this approximation is that the amount of computation required is proportional to N, in contrast to N^2 for molecular dynamics simulations. In essence, particle motions are modeled deterministically while collisions are treated probabilistically, each simulated molecule representing a large number of actual molecules. Typical computer runs of DSMC in the 1990s involve tens of millions of intermolecular collisions and fluid-solid interactions.

The DSMC computation is started from some initial condition and followed in small time steps that can be related to physical time. Colliding pairs of molecules in a small geometric cell in physical space are randomly selected after each computational time step. Complex physics such as radiation, chemical reactions and species concentrations can be included in the simulations without the necessity of nonequilibrium thermodynamic assumptions that commonly afflict nonequilibrium continuum-flow calculations. DSMC is more computationally intensive than classical continuum simulations, and should therefore be used only when the continuum approach is not feasible.

The DSMC technique is explicit and time marching, and therefore always produces unsteady flow simulations. For macroscopically steady flows, Monte Carlo simulation proceeds until a steady flow is established, within a desired accuracy, at sufficiently large time. The macroscopic flow quantities are then the time average of all values calculated after reaching the steady state. For macroscopically unsteady flows, ensemble averaging of many independent Monte Carlo simulations is carried out to obtain the final results within a prescribed statistical accuracy.

2.7 Liquid Flows. From the continuum point of view, liquids and gases are both fluids obeying the same equations of motion. For incompressible flows, for example, the Reynolds number is the primary dimensionless parameter that determines the nature of the flow field. True, water, for example, has density and viscosity that are, respectively, three and two orders of magnitude higher than those for air, but if the Reynolds number and geometry are matched, liquid and gas flows should be identical. (Barring phenomena unique to liquids such as cavitation, free surface flows, etc.) For MEMS applications, however, we anticipate the possibility of non-equilibrium flow conditions and the consequent invalidity of the Navier-Stokes equations and the no-slip boundary conditions. Such circumstances can best be researched using the molecular approach. This was discussed for gases in Section 2.6, and the corresponding arguments for liquids will be given in the present subsection. The literature on non-Newtonian fluids in general and polymers in particular is vast (for example, the bibliographic survey by Nadolink and Haigh, 1995, cites over 4,900 references on polymer drag reduction alone) and provides a rich source of information on the molecular approach for liquid flows.

Solids, liquids and gases are distinguished merely by the degree of proximity and the intensity of motions of their constituent molecules. In solids, the molecules are packed closely and confined, each hemmed in by its neighbors (Chapman and Cowling, 1970). Only rarely would one solid molecule slip from its neighbors to join a new set. As the solid is heated, molecular motion becomes more violent and a slight thermal expansion takes place. At a certain temperature that depends on ambient pressure, sufficiently intense motion of the molecules enables them to pass freely from one set of neighbors to another. The molecules are no longer confined but are nevertheless still closely packed, and the substance is now considered a liquid. Further heating of the matter eventually releases the molecules altogether, allowing them to break the bonds of their mutual attractions. Unlike solids and liquids, the resulting gas expands to fill any volume available to it.

Unlike solids, both liquids and gases cannot resist finite shear force without continuous deformation; that is the definition of a fluid medium. In contrast to the reversible, elastic, static deformation of a solid, the continuous deformation of a fluid resulting from the application of a shear stress results in an irreversible work that eventually becomes random thermal motion of the molecules; that is viscous dissipation. There are around 25-million molecules of STP air in a one-micron cube. The same cube would contain around 34-billion molecules of water. So, liquid flows are continuum even in extremely small devices through which gas flows would not. The average distance between molecules in the gas example is one order of magnitude higher than the diameter of its molecules, while that for the liquid phase approaches the molecular diameter. As a result, liquids are almost incompressible. Their isothermal compressibility coefficient α and bulk expansion coefficient β are much smaller compared to those for gases. For water, for example, a hundred-fold increase in pressure leads to less than 0.5% decrease in volume. Sound speeds through liquids are also high relative to those for gases, and as a result most liquid flows are incompressible. The exception being propagation of ultra-high-frequency sound waves and cavitation phenomena. (Note that we distinguish between a fluid and a flow being compressible/incompressible. For example, the flow of the highly compressible air can be either compressible or incompressible.)

The mechanism by which liquids transport mass, momentum and energy must be very different from that for gases. In dilute gases, intermolecular forces play no role and the molecules spend most of their time in free flight between brief collisions at which instances the molecules' direction and speed abruptly change. The random molecular motions are responsible for gaseous transport processes. In liquids, on the other hand, the molecules are closely packed though not fixed in one position. In essence, the liquid molecules are always in a *collision* state. Applying a shear force must create a velocity gradient so that the molecules move relative to one another, *ad infinitum* as long as the stress is applied. For liquids, momentum transport due to the random molecular motion is negligible compared to that due to the intermolecular forces. The straining between liquid molecules causes some to separate from their original neighbors, bringing them into the force field of new molecules. Across the plane of the shear stress, the sum of all intermolecular forces must, on the average, balance the imposed shear. Liquids at rest transmit only normal force, but when a velocity gradient occurs, the net intermolecular force would have a tangential component.

The incompressible Navier-Stokes equations describe liquid flows under most circumstances. Liquids, however, do not have a well advanced molecular-based theory as that for dilute gases. The concept of mean free path is not very useful for liquids and the conditions under which a liquid flow fails to be in quasi-equilibrium state are not well defined. There is no Knudsen number for liquid flows to guide us through the maze. We do not know, from first principles, the conditions under which the no-slip boundary condition becomes inaccurate, or the point at which the (stress)-(rate of strain) relation or the (heat flux)-(temperature gradient) relation fails to be linear. Certain empirical observations indicate that those simple relations that we take for granted occasionally fail to accurately model liquid flows. For example, it has been shown in rheological studies (Loose and Hess, 1989) that non-Newtonian behavior commences when the strain rate approximately exceeds twice the molecular frequency-scale

$$\dot{\gamma} = \frac{\partial u}{\partial y} \geq 2\tau^{-1} \tag{61}$$

where the molecular time-scale τ is given by

$$\tau = \left[\frac{m\sigma^2}{\epsilon}\right]^{1/2} \tag{62}$$

where m is the molecular mass, and σ and ϵ are respectively the characteristic length- and energy-scale for the molecules. For ordinary liquids such as water, this time-scale is extremely small and the threshold shear rate for the onset of non-Newtonian behavior is therefore extraordinarily high. For high-molecular-weight polymers, on the other hand, m and σ are both many orders of magnitude higher than their respective values for water, and the linear stress-strain relation breaks down at realistic values of the shear rate.

The moving contact line when a liquid spreads on a solid substrate is an example where slip flow must be allowed to avoid singular or unrealistic behavior in the Navier-Stokes solutions (Dussan and Davis, 1974; Dussan, 1976; 1979; Thompson and Robbins, 1989). Other examples where slip-flow must be admitted include corner flows (Moffatt, 1964; Koplik and Banavar, 1995) and extrusion of polymer melts from capillary tubes (Pearson and Petrie, 1968; Richardson, 1973; Den, 1990).

Existing experimental results of liquid flow in microdevices are contradictory. This is not surprising given the difficulty of such experiments and the lack of a guiding rational theory. Pfahler et al. (1990; 1991), Pfahler (1992), and Bau (1994) summarize the relevant literature. For small-length-scale flows, a phenomenological approach for analyzing the data is to define an apparent viscosity μ_a calculated so that if it were used in the traditional no-slip Navier-Stokes equations instead of the fluid viscosity μ, the results would be in agreement with experimental observations. Israelachvili (1986) and Gee et al. (1990) found that $\mu_a = \mu$ for thin-film flows as long as the film thickness exceeds 10 molecular layers ($\approx$5 nm). For thinner films, μ_a depends on the number of molecular layers and can be as much as 10^5 times larger than μ. Chan and Horn's (1985) results are somewhat different; the apparent viscosity deviates from the fluid viscosity for films thinner than 50 nm.

In polar-liquid flows through capillaries, Migun and Prokhorenko (1987) report that μ_a increases for tubes smaller than 1 micron in diameter. In contrast, Debye and Cleland (1959) report μ_a smaller than μ for paraffin flow in porous glass with average pore size several times larger than the molecular length-scale. Experimenting with microchannels ranging in depths from 0.5 micron to 50 microns, Pfahler et al. (1991) found that μ_a is consistently smaller than μ for both liquid (isopropyl alcohol; silicone oil) and gas (nitrogen; helium) flows in micro-

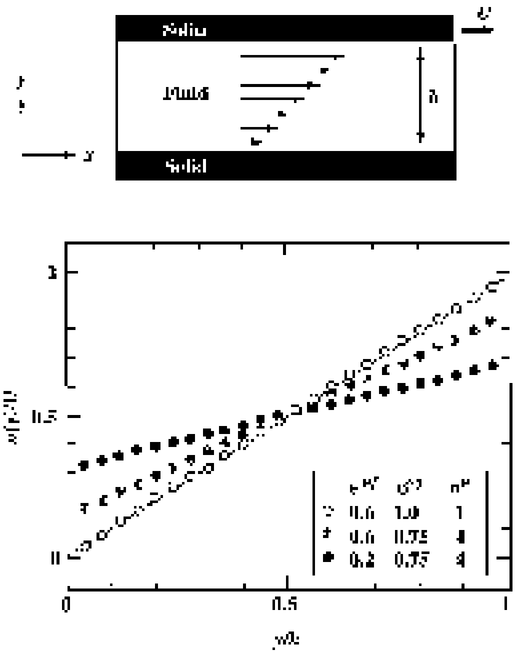

Fig. 9 Velocity profiles in a Couette flow geometry at different interfacial parameters. All three profiles are for $U = \sigma\tau^{-1}$, and $h = 24.57\sigma$. The dashed line is the no-slip Couette-flow solution. From Thompson and Troian (1997).

channels. For liquids, the apparent viscosity decreases with decreasing channel depth. Other researchers using small capillaries report that μ_a is about the same as μ (Anderson and Quinn, 1972; Tukermann and Pease, 1981; 1982; Tuckermann, 1984; Guvenc, 1985; Nakagawa et al., 1990).

The above contradictory results point to the need for replacing phenomenological models by first-principles ones. The lack of molecular-based theory of liquids—despite extensive research by the rheology and polymer communities—leaves molecular dynamics simulations as the nearest weapon to first-principles arsenal. MD simulations offer a unique approach to checking the validity of the traditional continuum assumptions. However, as was pointed out in Section 2.6, such simulations are limited to exceedingly minute flow extent.

Thompson and Troian (1997) provide molecular dynamics simulations to quantify the slip-flow boundary condition dependence on shear rate. Recall the linear Navier boundary condition introduced in Section 2.5,

$$\Delta u|_w = u_{\text{fluid}} - u_{\text{wall}} = L_s \left.\frac{\partial u}{\partial y}\right|_w \tag{63}$$

where L_s is the constant slip length, and $\partial u/\partial y|_w$ is the strain rate computed at the wall. The goal of Thompson and Troian's simulations was to determine the degree of slip at a solid-liquid interface as the interfacial parameters and the shear rate change. In their simulations, a simple liquid underwent planar shear in a Couette cell as shown in Fig. 9. The typical cell measured $12.51 \times 7.22 \times h$, in units of molecular length-scale σ, where the channel depth h varied in the range of $16.71\sigma - 24.57\sigma$, and the corresponding number of molecules simulated ranged from 1,152 to 1,728. The liquid is treated as an isothermal ensemble of spherical molecules. A shifted Lennart-Jones 6-12 potential is used to model intermolecular interactions, with energy- and length-scales ϵ and σ, and cut-off distance $r_c = 2.2\sigma$:

$$V(r) = 4\epsilon\left[\left(\frac{r}{\sigma}\right)^{-12} - \left(\frac{r}{\sigma}\right)^{-6} - \left(\frac{r_c}{\sigma}\right)^{-12} + \left(\frac{r_c}{\sigma}\right)^{-6}\right] \tag{64}$$

The truncated potential is set to zero for $r > r_c$.

The fluid-solid interaction is also modeled with a truncated Lennard-Jones potential, with energy- and length-scales ϵ^{wf} and σ^{wf}, and cut-off distance r_c. The equilibrium state of the fluid is a well-defined liquid phase characterized by number density $n = 0.81\sigma^{-3}$ and temperature $T = 1.1\epsilon/k$, where k is the Boltzmann constant.

The steady-state velocity profiles resulting from Thompson and Troian's (1997) MD simulations are depicted in Fig. 9 for different values of the interfacial parameters ϵ^{wf}, σ^{wf} and n^w. Those parameters, shown in units of the corresponding fluid parameters ϵ, σ and n, characterize, respectively, the strength of the liquid-solid coupling, the thermal roughness of the interface and the commensurability of wall and liquid densities. The macroscopic velocity profiles recover the expected flow behavior from continuum hydrodynamics with boundary conditions involving varying degrees of slip. Note that when slip exists, the shear rate $\dot{\gamma}$ no longer equals U/h. The degree of slip increases (i.e. the amount of momentum transfer at the wall-fluid interface decreases) as the relative wall density n^w increases or the strength of the wall-fluid coupling σ^{wf} decreases; in other words when the relative surface energy corrugation of the wall decreases. Conversely, the corrugation is maximized when the wall and fluid densities are commensurate and the strength of the wall-fluid coupling is large. In this case, the liquid feels the corrugations in the surface energy of the solid owing to the atomic close-packing. Consequently, there is efficient momentum transfer and the no-slip condition applies, or in extreme cases, a 'stick' boundary condition takes hold.

Variations of the slip length L_s and viscosity μ as functions of shear rate $\dot{\gamma}$ are shown in parts (a) and (b) of Fig. 10, for five different sets of interfacial parameters. For Couette flow, the slip length is computed from its definition, $L_s = \Delta u|_w/\dot{\gamma} = (U/\dot{\gamma} - h)/2$. The slip length, viscosity and shear rate are normalized in the figure using the respective molecular scales for length σ, viscosity $\epsilon\tau\sigma^{-3}$, and inverse time τ^{-1}. The viscosity of the fluid is constant over the entire range of shear rates (Fig. 10(b)), indicating Newtonian behavior. As indicated earlier, non-Newtonian behavior is expected for $\dot{\gamma} \geq 2\tau^{-1}$, well above the shear rates used in Thompson and Troian's simulations.

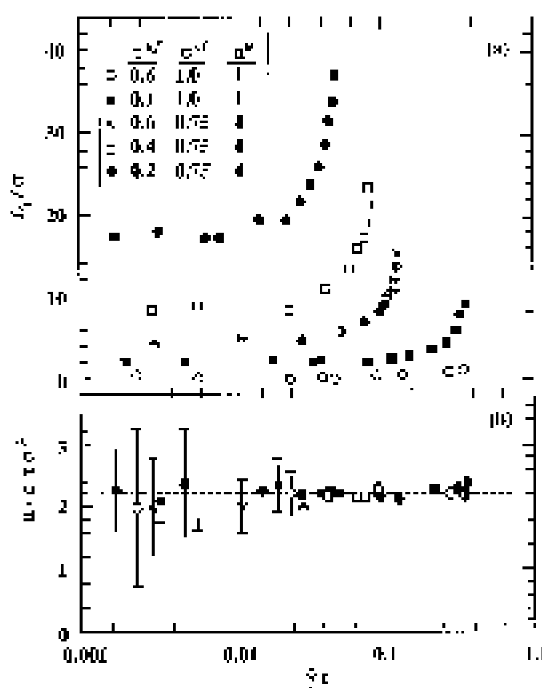

Fig. 10 Variation of slip length and viscosity as functions of shear rate. From Thompson and Troian (1997).

At low shear rates, the slip length behavior is consistent with the Navier model, i.e., is independent of the shear rate. Its limiting value L_s^o ranges from 0 to $\sim 17\sigma$ for the range of interfacial parameters chosen (Fig. 10(a)). In general, the amount of slip increases with decreasing surface energy corrugation. Most interestingly, at high shear rates the Navier condition breaks down as the slip length increases rapidly with $\dot{\gamma}$. The critical shear-rate value for the slip length to diverge, $\dot{\gamma}_c$, decreases as the surface energy corrugation decreases. Surprisingly, the boundary condition is nonlinear even though the liquid is still Newtonian. In dilute gases, as discussed in Section 2.6, the linear slip condition and the Navier-Stokes equations, with their linear stress-strain relation, are both valid to the same order of approximation in Knudsen number. In other words, deviation from linearity is expected to take place at the same value of Kn = 0.1. In liquids, in contrast, the slip length appears to become nonlinear and to diverge at a critical value of shear rate well below the shear rate at which the linear stress-strain relation fails. Moreover, the boundary condition deviation from linearity is not gradual but is rather catastrophic. The critical value of shear rate $\dot{\gamma}_c$ signals the point at which the solid can no longer impart momentum to the liquid. This means that the same liquid molecules sheared against different substrates will experience varying amounts of slip and vice versa.

Based on the above results, Thompson and Troian (1997) suggest a universal boundary condition at a solid-liquid interface. Scaling the slip length L_s by its asymptotic limiting value L_s^o and the shear rate $\dot{\gamma}$ by its critical value $\dot{\gamma}_c$, collapses the data in the single curve shown in Figure 11. The data points are well described by the relation

$$L_s = L_s^o\left[1 - \frac{\dot{\gamma}}{\dot{\gamma}_c}\right]^{-1/2} \qquad (65)$$

The nonlinear behavior close to a critical shear rate suggests that the boundary condition can significantly affect flow behavior at macroscopic distances from the wall. Experiments with polymers confirm this observation (Atwood and Schwalter, 1989). The rapid change in the slip length suggests that for flows in the vicinity of $\dot{\gamma}_c$, small changes in surface properties can lead to large fluctuations in the apparent boundary condition. Thompson and Troian (1997) conclude that the Navier slip condition is but the low-shear-rate limit of a more generalized universal relationship which is nonlinear and divergent. Their relation provides a mechanism for relieving the stress singularity in spreading contact lines and corner flows, as it naturally allows for varying degrees of slip on approach to regions of higher rate of strain.

To place the above results in physical terms, consider water at a temperature of $T = 288$ K. (Water molecules are complex ones, forming directional, short-range covalent bonds. Thus requiring a more complex potential than the Lennard-Jones to describe the intermolecular interactions. For the purpose of the qualitative example described here, however, we use the computational results of Thompson and Troian (1997) who employed the L-J potential.) The energy-scale in the Lennard-Jones potential is then $\epsilon = 3.62 \times 10^{-21}$ J. For water, $m = 2.99 \times 10^{-26}$ kg, $\sigma = 2.89 \times 10^{-10}$ m, and at standard temperature $n = 3.35 \times 10^{28}$ molecules/m^3. The molecular time-scale can thus be computed, $\tau = [m\sigma^2/\epsilon]^{1/2} = 8.31 \times 10^{-13}$ s. For the third case depicted in Fig. 11 (the open squares), $\dot{\gamma}_c \tau = 0.1$, and the critical shear rate at which the slip condition diverges is thus $\dot{\gamma}_c = 1.2 \times 10^{11}$ s^{-1}. Such an enormous rate of strain may be found in extremely small devices having extremely high speeds. (Note however that $\dot{\gamma}_c$ for high-molecular-weight polymers would be many orders of magnitude smaller than the value developed here for water.) On the other hand, the conditions to achieve a measurable slip of 17σ (the solid circles in Fig. 10) are not difficult to encounter in microdevices: density of solid

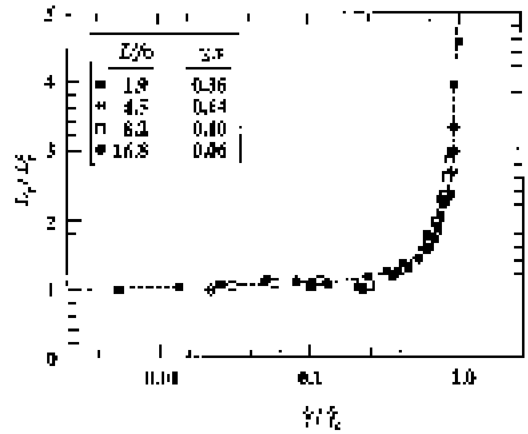

Fig. 11 Universal relation of slip length as a function of shear rate. From Thompson and Troian (1997).

four times that of liquid, and energy-scale for wall-fluid interaction that is one fifth of energy-scale for liquid.

The limiting value of slip length is independent of the shear rate and can be computed for water as $L_s^o = 17\sigma = 4.91 \times 10^{-9}$ m. Consider a water microbearing having a shaft diameter of 100 μm and rotation rate of 20,000 rpm and a minimum gap of $h = 1$ μm. In this case, $U = 0.1$ m/s and the no-slip shear rate is $U/h = 10^5$ s^{-1}. When slip occurs at the limiting value just computed, the shear rate and the wall slip-velocity are computed as follows

$$\dot{\gamma} = \frac{U}{h + 2L_s^o} = 9.90 \times 10^4 \text{ s}^{-1} \qquad (66)$$

$$\Delta u|_w = \dot{\gamma} L_s = 4.87 \times 10^{-4} \text{ m/s} \qquad (67)$$

As a result of the Navier slip, the shear rate is reduced by 1% from its no-slip value, and the slip velocity at the wall is about 0.5% of U, small but not insignificant.

2.8 Surface Phenomena. As mentioned in Section 2.1, the surface-to-volume ratio for a machine with a characteristic length of 1 m is 1 m^{-1}, while that for a MEMS device having a size of 1 μm is 10^6 m^{-1}. The million-fold increase in surface area relative to the mass of the minute device substantially affects the transport of mass, momentum and energy through the surface. Obviously surface effects dominate in small devices. The surface boundary conditions in MEMS flows have already been discussed in Sections 2.5 and 2.7. In microdevices, it has been shown that it is possible to have measurable slip-velocity and temperature jump at a solid-fluid interface. In this subsection, we illustrate other ramifications of the large surface-to-volume ratio unique to MEMS, and provide a molecular viewpoint to surface forces.

In microdevices, both radiative and convective heat loss/gain are enhanced by the huge surface-to-volume ratio. Consider a device having a characteristic length L_s. Use of the lumped capacitance method to compute the rate of convective heat transfer, for example, is justified if the Biot number ($\equiv hL_s/\kappa_s$, where h is the convective heat transfer coefficient of the fluid and κ_s is the thermal conductivity of the solid) is less than 0.1. Small L_s implies small Biot number, and a nearly uniform temperature within the solid. Within this approximation, the rate at which heat is lost to the surrounding fluid is given by

$$\rho_s L_s^3 c_s \frac{dT_s}{dt} = -hL_s^2(T_s - T_\infty) \qquad (68)$$

where ρ_s and c_s are respectively the density and specific heat of the solid, T_s is its (uniform) temperature, and T_∞ is the ambient fluid temperature. Solution of the above equation is trivial, and the temperature of a hot surface drops exponentially with time from an initial temperature T_i,

$$\frac{T_s(t) - T_\infty}{T_i - T_\infty} = \exp\left[-\frac{t}{\mathcal{T}}\right] \quad (69)$$

where the time constant $\mathcal{T}$ is given by

$$\mathcal{T} = \frac{\rho_s L_s^3 c_s}{h L_s^2} \quad (70)$$

For small devices, the time it takes the solid to cool down is proportionally small. Clearly, the million-fold increase in surface-to-volume ratio implies a proportional increase in the rate at which heat escapes. Identical scaling arguments can be made regarding mass transfer.

Another effect of the diminished scale is the increased importance of surface forces and the waning importance of body forces. Based on biological studies, Went (1968) concludes that the demarkation length-scale is around 1 mm. Below that, surface forces dominate over gravitational forces. A 10-mm piece of paper will fall down when gently placed on a smooth, vertical wall, while a 0.1-mm piece will stick. Try it! *Stiction* is a major problem in MEMS applications. Certain structures such as long, thin polysilicon beams and large, thin comb drives have a propensity to stick to their substrates and thus fail to perform as designed (Mastrangelo and Hsu, 1992; Tang et al., 1989).

Conventional dry friction between two solids in relative motion is proportional to the normal force which is usually a component of the moving device weight. The friction is independent of the contact-surface area because the van der Waals cohesive forces are negligible relative to the weight of the macroscopic device. In MEMS applications, the cohesive intermolecular forces between two surfaces are significant and the stiction is independent of the device mass but is proportional to its surface area. The first micromotor did not move—despite large electric current through it—until the contact area between the 100-micron rotor and the substrate was reduced significantly by placing dimples on the rotor's surface (Fan et al., 1988; 1989; Tai and Muller, 1989).

One last example of surface effects that to my knowledge has not been investigated for microflows is the adsorbed layer in gaseous wall-bounded flows. It is well known (see, for example, Brunauer, 1944; Lighthill, 1963) that when a gas flows in a duct, the gas molecules are attracted to the solid surface by the van der Waals and other forces of cohesion. The potential energy of the gas molecules drops on reaching the surface. The adsorbed layer partakes the thermal vibrations of the solid, and the gas molecules can only escape when their energy exceeds the potential energy minimum. In equilibrium, at least part of the solid would be covered by a monomolecular layer of adsorbed gas molecules. Molecular species with significant partial pressure—relative to their vapor pressure—may locally form layers two or more molecules thick. Consider, for example, the flow of a mixture of dry air and water vapor at STP. The energy of adsorption of water is much larger than that for nitrogen and oxygen, making it more difficult for water molecules to escape the potential energy trap. It follows that the life time of water molecules in the adsorbed layer significantly exceeds that for the air molecules (by 60,000 folds, in fact) and, as a result, the thin surface layer would be mostly water. For example, if the proportion of water vapor in the ambient air is 1:1,000 (i.e., very low humidity level), the ratio of water to air in the adsorbed layer would be 60:1. Microscopic roughness of the solid surface causes partial condensation of the water along portions having sufficiently strong concave curvature. So, surfaces exposed to non-dry air flows are mainly liquid water surfaces. In most applications, this thin adsorbed layer has little effect on the flow dynamics, despite the fact that the density and viscosity of liquid water are far greater than those for air. In MEMS applications, however, the layer thickness may not be an insignificant portion of the characteristic flow dimension and the water layer may have a measurable effect on the gas flow. A hybrid approach of molecular dynamics and continuum flow simulations or MD-Monte Carlo simulations may be used to investigate this issue.

It should be noted that quite recently, Majumdar and Mezic (1998; 1999) have studied the stability and rupture into droplets of thin liquid films on solid surfaces. They point out that the free energy of a liquid film consists of a surface tension component as well as highly nonlinear volumetric intermolecular forces resulting from van der Waals, electrostatic, hydration and elastic strain interactions. For water films on hydrophilic surfaces such as silica and mica, Majumdar and Mezic (1998) estimate the equilibrium film thickness to be about 0.5 nm (2 monolayers) for a wide range of ambient-air relative humidities. The equilibrium thickness grows very sharply, however, as the relative humidity approaches 100%.

Majumdar and Mezic's (1998; 1999) results open many questions. What are the stability characteristics of their water film in the presence of air flow above it? Would this water film affect the accommodation coefficient for microduct air flow? In a modern Winchester-type hard disk, the drive mechanism has a read/write head that floats 50 nm above the surface of the spinning platter. The head and platter together with the air layer in between form a slider bearing. Would the computer performance be affected adversely by the high relative humidity on a particular day when the adsorbed water film is no longer 'thin'? If a microduct hauls liquid water, would the water film adsorbed by the solid walls influence the effective viscosity of the water flow? Electrostatic forces can extend to almost 1 micron (the Debye length), and that length is known to be highly pH-dependent. Would the water flow be influenced by the surface and liquid chemistry? Would this explain the contradictory experimental results of liquid flows in microducts discussed in Section 2.7?

The few examples above illustrate the importance of surface effects in small devices. From the continuum viewpoint, forces at a solid-fluid interface are the limit of pressure and viscous forces acting on a parallel elementary area displaced into the fluid, when the displacement distance is allowed to tend to zero. From the molecular point of view, all macroscopic surface forces are ultimately traced to intermolecular forces, which subject is extensively covered in the book by Israelachvilli (1991) and references therein. Here we provide a very brief introduction to the molecular viewpoint. The four forces in nature are (1) the strong and (2) weak forces describing the interactions between neutrons, protons, electrons, etc.; (3) the electromagnetic forces between atoms and molecules; and (4) gravitational forces between masses. The range of action of the first two forces is around 10^{-5} nm, and hence neither concerns us overly in MEMS applications. The electromagnetic forces are effective over a much larger though still small distance on the order of the interatomic separations (0.1–0.2 nm). Effects over longer range—several orders of magnitude longer—can and do rise from the short range intermolecular forces. For example, the rise of liquid column in capillaries and the action of detergent molecules in removing oily dirt from fabric are the result of intermolecular interactions. Gravitational forces decay with the distance to second power, while intermolecular forces decay much quicker, typically with the seventh power. Cohesive forces are therefore negligible once the distance between molecules exceeds few molecular diameters, while massive bodies like stars and planets are still strongly interacting, via gravity, over astronomical distances.

Electromagnetic forces are the source of all intermolecular interactions and the cohesive forces holding atoms and molecules together in solids and liquids. They can be classified into (1) purely electrostatic arising from the Coulomb force between

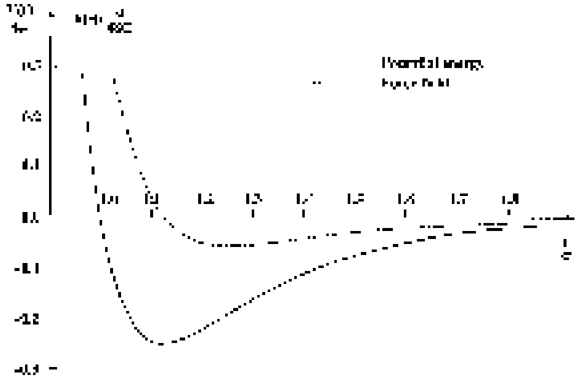

Fig. 12 Typical Lennard-Jones 6–12 potential and the intermolecular force field resulting from it. Only a small portion of the potential function is shown for clarity.

charges, interactions between charges, permanent dipoles, quadrupoles, etc.; (2) polarization forces arising from the dipole moments induced in atoms and molecules by the electric field of nearby charges and permanent dipoles; and (3) quantum mechanical forces that give rise to covalent or chemical bonding and to repulsive steric or exchange interactions that balance the attractive forces at very short distances. The Hellman-Feynman theorem of quantum mechanics states that once the spatial distribution of the electron clouds has been determined by solving the appropriate Schrödinger equation, intermolecular forces may be calculated on the basis of classical electrostatics, in effect reducing all intermolecular forces to Coulombic forces. Note, however, that intermolecular forces exist even when the molecules are totally neutral. Solutions of the Schrödinger equation for general atoms and molecules are not easy of course, and alternative modeling are sought to represent intermolecular forces. The van der Waals attractive forces are usually represented with a potential that varies as the inverse-sixth power of distance, while the repulsive forces are represented with either a power or an exponential potential.

A commonly used potential between two molecules is the generalized Lennard-Jones (L-J 6-12) pair potential given by

$$V_{ij}(r) = 4\epsilon\left[c_{ij}\left(\frac{r}{\sigma}\right)^{-12} - d_{ij}\left(\frac{r}{\sigma}\right)^{-6}\right] \tag{71}$$

where V_{ij} is the potential energy between two particles i and j, r is the distance between the two molecules, ϵ and σ are, respectively, characteristic energy and length-scales, and c_{ij} and d_{ij} are parameters to be chosen for the particular fluid and solid combinations under consideration. The first term in the right-hand side is the strong repulsive force that is felt when two molecules are at extremely close range comparable to the molecular length-scale. That short-range repulsion prevents overlap of the molecules in physical space. The second term is the weaker, van der Waals attractive force that commences when the molecules are sufficiently close (several times σ). That negative part of the potential represents the attractive polarization interaction of neutral, spherically symmetric particles. The power of 6 associated with this term is derivable from quantum mechanics considerations, while the power of the repulsive part of the potential is found empirically. The Lennard-Jones potential is zero at very large distances, has a weak negative peak at r slightly larger than σ, is zero at $r = \sigma$, and is infinite as $r \rightarrow 0$.

The force field resulting from this potential is given by

$$F_{ij}(r) = -\frac{\partial V_{ij}}{\partial r} = \frac{48\epsilon}{\sigma}\left[c_{ij}\left(\frac{r}{\sigma}\right)^{-13} - \frac{d_{ij}}{2}\left(\frac{r}{\sigma}\right)^{-7}\right] \tag{72}$$

A typical L-J 6-12 potential and force field are shown in Fig. 12, for $c = d = 1$. The minimum potential $V_{\min} = -\epsilon$, corresponds to the equilibrium position (zero force) and occurs at $r = 1.12\sigma$. The attractive van der Waals contribution to the minimum potential is -2ϵ, while the repulsive energy contribution is $+\epsilon$. Thus the inverse 12th power repulsive force term decreases the strength of the binding energy at equilibrium by 50%.

The L-J potential is commonly used in molecular dynamics simulations to model intermolecular interactions between dense gas or liquid molecules and between fluid and solid molecules. As mentioned in Section 2.7, such potential is not accurate for complex substances such as water whose molecules form directional covalent bonds. As a result, MD simulations for water are much more involved.

3 Typical Fluid Applications

3.1 Prologue. The physics of fluid flows in microdevices was covered in Section 2. In this section, we provide a number of examples of useful applications of MEMS devices in fluid mechanics. The list is by no means exhaustive, but includes the use of MEMS-based sensors and actuators for flow diagnosis and control, a recently developed viscous micropump/microturbine, and analysis of a journal microbearing. The paper by Löfdahl and Gad-el-Hak (1999) offers more detail on some of the topics covered in this section.

3.2 Turbulence Measurements. Microelectromechanical systems offer great opportunities for better flow diagnosis and control, particularly for turbulent flows. The batch processing fabrication of microdevices makes it possible to produce large number of identical transducers within extremely tight tolerance. Microsensors and microactuators are small, inexpensive, combine electronic and mechanical parts, have low energy consumption and can be distributed over a wide area. In this subsection we discuss the advantages of using MEMS-based sensors for turbulence measurements, and in the following subsection the issue of flow control will be addressed.

Turbulence remains largely an enigma, analytically unapproachable yet practically very important. For a turbulent flow, the dependent variables are random functions of space and time, and no straightforward method exists for analytically obtaining stochastic solutions to the governing nonlinear, partial differential equations. The statistical approach to solving the Navier-Stokes equations sets a more modest aim of solving for the average flow quantities rather than the instantaneous ones. But as a result of the nonlinearity of the governing equations, this approach always leads to more unknowns than equations (the closure problem), and solutions based on first principles are again not possible. Turbulence, therefore, is a conundrum that appears to yield its secrets only to physical and numerical experiments, provided that the wide band of relevant scales is fully resolved—a far-from-trivial task particularly at high Reynolds numbers.

A turbulent flow field is composed of a hierarchy of eddies having a broad range of time- and length-scales. The largest eddies have a spatial extension of approximately the same size as the width of the flow field, while the smallest eddies are of the size where viscous effects become dominant and energy is transferred from kinetic into internal. The ratio of the smallest length-scale—the Kolmogorov microscale η—to the largest scale l is related to the turbulence Reynolds number as follows

$$\frac{\eta}{l} \approx \left(\frac{ul}{\nu}\right)^{-3/4} = \mathrm{Re}^{-3/4} \tag{73}$$

Similar expressions can be written for time- and velocity-scales (see, for example, Tennekes and Lumley, 1972). Not only does a sensor have to be sufficiently small to resolve the smallest eddies, but multi-sensors distributed over a large volume are needed to detect any flow structures at the largest scale. Clearly, the problem worsens as the Reynolds number increases.

In wall-bounded flows, the shear-layer thickness provides a measure of the largest eddies in the flow. The smallest scale is the viscous wall unit. Viscous forces dominate over inertia in the near-wall region. The characteristic scales there are obtained from the magnitude of the mean vorticity in the region and its viscous diffusion away from the wall. Thus, the viscous time-scale, t_ν, is given by the inverse of the mean wall vorticity

$$t_\nu = \left[\left. \frac{\partial \bar{U}}{\partial y} \right|_w \right]^{-1} \tag{74}$$

where $\bar{U}$ is the mean streamwise velocity. The viscous length-scale, l_ν, is determined by the characteristic distance by which the (spanwise) vorticity is diffused from the wall, and is thus given by

$$l_\nu = \sqrt{\nu t_\nu} = \sqrt{\frac{\nu}{\left. \frac{\partial \bar{U}}{\partial y} \right|_w}} \tag{75}$$

where ν is the kinematic viscosity. The wall velocity-scale (so-called friction velocity, u_τ) follows directly from the time and length-scales

$$u_\tau = \frac{l_\nu}{t_\nu} = \sqrt{\nu \left. \frac{\partial \bar{U}}{\partial y} \right|_w} = \sqrt{\frac{\tau_w}{\rho}} \tag{76}$$

where τ_w is the mean shear stress at the wall, and ρ is the fluid density. A wall unit implies scaling with the viscous scales, and the usual $(\ )^+$ notation is used; for example, $y^+ = y/l_\nu = yu_\tau/\nu$. In the wall region, the characteristic length for the large eddies is y itself, while the Kolmogorov scale is related to the distance from the wall y as follows

$$\eta^+ \equiv \frac{\eta u_\tau}{\nu} \approx (\kappa y^+)^{1/4} \tag{77}$$

where κ is the von Kármán constant (≈ 0.41). As y^+ changes in the range of 1–5 (the extent of the viscous sublayer), η changes from 0.8 to 1.2 wall units.

It is clear from the above that the spatial and temporal resolutions for any probe to be used to resolve high-Reynolds-number turbulent flows are extremely tight. For example, both the Kolmogorov scale and the viscous length-scale change from few microns at the typical field Reynolds number—based on the momentum thickness—of 10^6, to a couple of hundred microns at the typical laboratory Reynolds number of 10^3. MEMS sensors for pressure, velocity, temperature and shear stress are at least one order of magnitude smaller than conventional sensors (Ho and Tai, 1996; Löfdahl et al., 1996). Their small size improves both the spatial and temporal resolutions of the measurements, typically few microns and few microseconds, respectively. For example, a micro-hot-wire (called hot point) has very small thermal inertia and the diaphragm of a micro-pressure-transducer has correspondingly fast dynamic response. Moreover, the microsensors' extreme miniaturization and low energy consumption make them ideal for monitoring the flow state without appreciably affecting it. Lastly, literally hundreds of microsensors can be fabricated on the same silicon chip at a reasonable cost, making them well suited for distributed measurements. The UCLA/Caltech team (see, for example, Ho and Tai, 1996; 1998, and references therein) has been very effective in developing many MEMS-based sensors and actuators for turbulence diagnosis and control.

3.3 Flow Control. Due to their small size, fast response, low unit-cost and energy consumption and an ability to combine mechanical and electronic components, MEMS-based sensors and actuators are presently the best candidate for reactive control of turbulent flows where distributed arrays of sensing and actuation elements are required. In this subsection we offer a brief introduction to targeted flow control. More detail are found in the review papers by Gad-el-Hak (1989; 1994; 1996), Wilkinson (1990), and Moin and Bewley (1994).

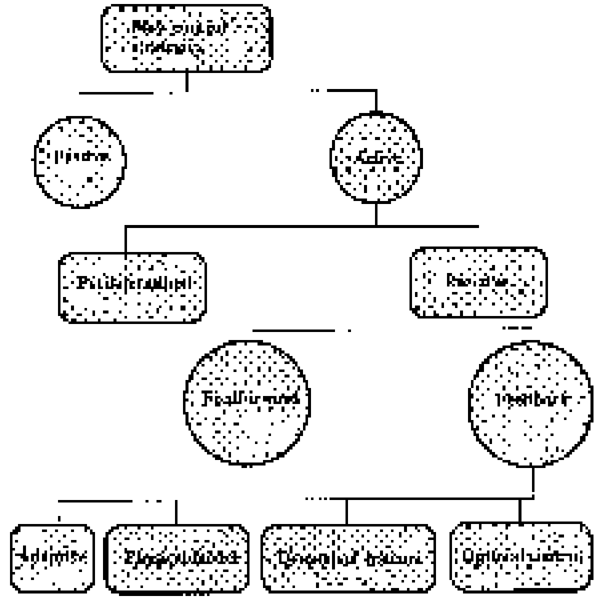

Fig. 13 Classification of flow control strategies

The ability to actively or passively manipulate a flow field to effect a desired change is of immense technological importance, and this undoubtedly accounts for the fact that the subject is more hotly pursued by scientists and engineers than any other topic in fluid mechanics. The potential benefits of realizing efficient flow control systems range from saving billions of dollars in annual fuel cost for land, air and sea vehicles to achieving economically/environmentally more competitive industrial processes involving fluid flows. Flow control can be used to achieve transition delay/advance, separation postponement/provocation, lift enhancement, drag reduction, turbulence augmentation/suppression or noise reduction.

3.3.1 Classification Schemes. There are different classification schemes for flow control methods. One is to consider whether the technique is applied at the wall or away from it. Surface parameters that can influence the flow include roughness, shape, curvature, rigid-wall motion, compliance, temperature and porosity. Heating and cooling of the surface can influence the flow via the resulting viscosity and density gradients. Mass transfer can take place through a porous wall or a wall with slots. Suction and injection of primary fluid can have significant effects on the flow field, influencing particularly the shape of the velocity profile near the wall and thus the boundary layer susceptibility to transition and separation. Different additives, such as polymers, surfactants, micro-bubbles, droplets, particles, dust or fibers, can also be injected through the surface in water or air wall-bounded flows. Control devices located away from the surface can also be beneficial. Large-eddy breakup devices (also called outer-layer devices, or OLDs), acoustic waves bombarding a shear layer from outside, additives introduced in the middle of a shear layer, manipulation of freestream turbulence levels and spectra, gust, and magneto- and electro-hydrodynamic body forces are examples of flow control strategies applied away from the wall.

A second scheme for classifying flow control methods considers energy expenditure and the control loop involved. As shown in the schematic in Fig. 13, a control device can be

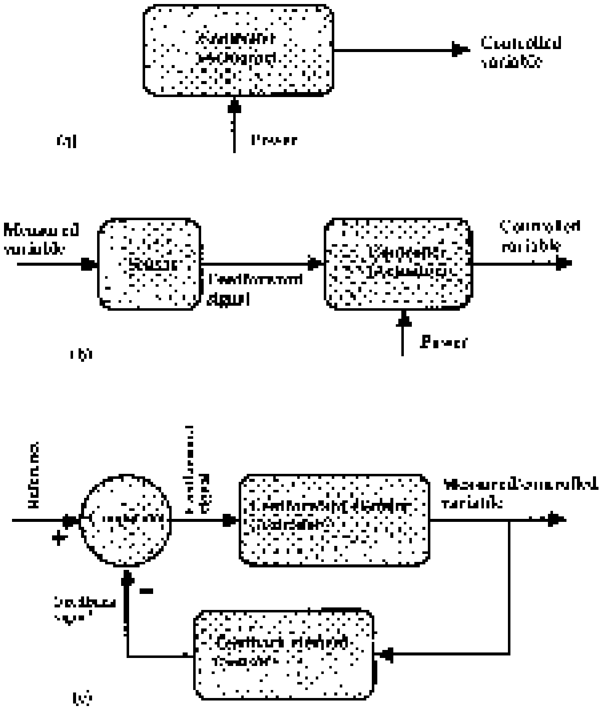

Fig. 14 Different control loops for active flow control. (*a*) Predetermined, open-loop control; (*b*) reactive, feedforward, open-loop control; (*c*) reactive, feedback, closed-loop control.

passive, requiring no auxiliary power, or active, requiring energy expenditure. As for the action of passive devices, some prefer to use the term flow management rather than flow control (Fiedler and Fernholz, 1990), reserving the latter terminology for dynamic processes. Active control—always requiring actuators—is further divided into predetermined or reactive. Predetermined control includes the application of steady or unsteady energy input without regard to the particular state of the flow. The control loop in this case is open as shown in Figure 14(*a*), and no sensors are required. Reactive control is a special class of active control where the control input is continuously adjusted based on measurements of some kind. The control loop in this case can either be an open, feedforward one (Fig. 14(*b*)) or a closed, feedback loop (Fig. 14(*c*)). Classical control theory deals, for the most part, with reactive control.

The distinction between feedforward and feedback is particularly important when dealing with the control of flow structures which convect over stationary sensors and actuators. In feedforward control, the measured variable and the controlled variable differ. For example, the pressure or velocity can be sensed at an upstream location, and the resulting signal is used together with an appropriate control law to trigger an actuator which in turn influences the velocity at a downstream position. Feedback control, on the other hand, necessitates that the controlled variable be measured, fed back and compared with a reference input. Reactive feedback control is further classified into four categories: Adaptive, physical model-based, dynamical systems-based and optimal control (Moin and Bewley, 1994).

A yet another classification scheme is to consider whether the control technique directly modifies the shape of the instantaneous/mean velocity profile or selectively influence the small dissipative eddies. An inspection of the Navier-Stokes equations written at the surface indicates that the spanwise and streamwise vorticity fluxes at the wall can be changed, either instantaneously or in the mean, via wall motion/compliance, suction/injection, streamwise or spanwise pressure-gradient (respectively), or normal viscosity-gradient. (Note that streamwise vorticity exists only if the velocity field is three-dimensional, instantaneously or in the mean.) These vorticity fluxes determine the fullness of the corresponding velocity profiles. For example, suction (or downward wall motion), favorable pressure-gradient or lower wall-viscosity results in vorticity flux away from the wall, making the surface a source of spanwise and streamwise vorticity. The corresponding fuller velocity profiles have negative curvature at the wall and are more resistant to transition and to separation but are associated with higher skin-friction drag. Conversely, an inflectional velocity profile can be produced by injection (or upward wall motion), adverse pressure-gradient or higher wall-viscosity. Such profile is more susceptible to transition and to separation and is associated with lower, even negative, skin friction. Note that many techniques are available to effect a wall viscosity-gradient; for example surface heating/cooling, film boiling, cavitation, sublimation, chemical reaction, wall injection of lower/higher viscosity fluid and the presence of shear thinning/thickening additive.

Flow control devices can alternatively target certain scales of motion rather than globally changing the velocity profile. Polymers, riblets and LEBUs, for example, appear to selectively damp only the small dissipative eddies in turbulent wall-bounded flows. These eddies are responsible for the (instantaneous) inflectional profile and the secondary instability in the buffer zone, and their suppression leads to increased scales, a delay in the reduction of the (mean) velocity-profile slope and consequent thickening of the wall region. In the buffer zone, the scales of the dissipative and energy containing eddies are roughly the same and, hence, the energy containing eddies will also be suppressed resulting in reduced Reynolds stress production, momentum transport and skin friction.

Considering the extreme complexity of the turbulence problem in general and the unattainability of first-principles analytical solutions in particular, it is not surprising that controlling a turbulent flow remains a challenging task, mired in empiricism and unfulfilled promises and aspirations. Brute force suppression, or *taming*, of turbulence via active, energy-consuming control strategies is always possible, but the penalty for doing so often exceeds any potential benefits. The artifice is to achieve a desired effect with minimum energy expenditure. This is where the concept of reactive control and the use of microsensors/microactuators come into the domain of this paper.

3.3.2 Control of Turbulence. Numerous methods of flow control have already been successfully implemented in practical engineering devices. Yet, very few of the classical strategies are effective in controlling free-shear or wall-bounded turbulent flows. Serious limitations exist for some familiar control techniques when applied to certain turbulent flow situations. For example, in attempting to reduce the skin-friction drag of a body having a turbulent boundary layer using global suction, the *penalty* associated with the control device often exceeds the saving derived from its use. What is needed is a way to reduce this penalty to achieve a more efficient control.

Flow control is most effective when applied near the transition or separation points; in other words, near the critical flow regimes where flow instabilities magnify quickly. Therefore, delaying/advancing laminar-to-turbulence transition and preventing/provoking separation are relatively easier tasks to accomplish. To reduce the skin-friction drag in a non-separating turbulent boundary layer, where the mean flow is quite stable, is a more challenging problem. Yet, even a modest reduction in the fluid resistance to the motion of, for example, the worldwide commercial air fleet is translated into fuel savings estimated to be in the billions of dollars. Newer ideas for turbulent flow control focus on the direct onslaught on coherent structures. Spurred by the recent developments in chaos control, microfabrication and soft computing tools, reactive control of turbulent flows is now in the realm of the possible for future practical devices.

Such futuristic systems are envisaged as consisting of a large number of intelligent, interactive, microfabricated wall sensors and actuators arranged in a checkerboard pattern and targeted towards specific organized structures that occur randomly within the boundary layer. Sensors detect oncoming coherent structures, and adaptive controllers process the sensors information and provide control signals to the actuators which in turn attempt to favorably modulate the quasi-periodic events. Finite number of wall sensors perceive only partial information about the entire flow field above. However, a low-dimensional dynamical model of the near-wall region used in a Kalman filter can make the most of the partial information from the sensors. Conceptually all of that is not too difficult, but in practice the complexity of such a control system is daunting and much research and development work still remain.

Targeted control implies sensing and reacting to a particular quasi-periodic structure in the boundary layer. The wall seems to be the logical place for such reactive control, because of the relative ease of placing something in there, the sensitivity of the flow in general to surface perturbations and the proximity and therefore accessibility to the dynamically all important near-wall coherent events.

3.3.3 Targeted Control. As discussed above, successful techniques to reduce the skin friction in a turbulent flow, such as polymers, particles or riblets, appear to act indirectly through local interaction with discrete turbulent structures, particularly small-scale eddies, within the flow. Common characteristics of all these methods are increased losses in the near-wall region, thickening of the buffer layer, and lowered production of Reynolds shear stress (Bandyopadhyay, 1986). Methods that act directly on the mean flow, such as suction or lowering of near-wall viscosity, also lead to inhibition of Reynolds stress. However, skin friction is increased when any of these velocity-profile modifiers is applied globally.

Could these seemingly inefficient techniques, e.g., global suction, be used more sparingly and be optimized to reduce their associated penalty? It appears that the more successful drag-reduction methods, e.g., polymers, act selectively on particular scales of motion and are thought to be associated with stabilization of the secondary instabilities. It is also clear that energy is wasted when suction or heating/cooling is used to suppress the turbulence throughout the boundary layer when the main interest is to affect a near-wall phenomenon. One ponders, what would become of wall turbulence if specific coherent structures are to be targeted, by the operator through a reactive control scheme, for modification? The myriad of organized structures present in all shear flows are instantaneously identifiable, quasi-periodic motions (Cantwell, 1981; Robinson, 1991). Bursting events in wall-bounded flows, for example, are both intermittent and random in space as well as time. The random aspects of these events reduce the effectiveness of a predetermined active control strategy. If such structures are nonintrusively detected and altered, on the other hand, net performance gain might be achieved. It seems clear, however, that temporal phasing as well as spatial selectivity would be required to achieve proper control targeted towards random events.

A nonreactive version of the above idea is the *selective suction technique* which combines suction to achieve an asymptotic turbulent boundary layer and longitudinal riblets to fix the location of low-speed streaks (Gad-el-Hak and Blackwelder, 1989). Although far from indicating net drag reduction, the available results are encouraging and further optimization is needed. When implemented via an array of reactive control loops, the selective suction method is potentially capable of skin-friction reduction that approaches 60%.

3.3.4 Required Characteristics. The randomness of the bursting events necessitates temporal phasing as well as spatial selectivity to effect selective (targeted) control. Practical applications of methods targeted at controlling a particular turbulent structure to achieve a prescibed goal would therefore require implementing a large number of surface sensors/actuators together with appropriate control algorithms. That strategy for controlling wall-bounded turbulent flows has been advocated by, among others and in chronological order, Gad-el-Hak and Blackwelder (1987; 1989), Blackwelder and Gad-el-Hak (1990), Lumley (1991; 1996), Choi et al. (1992; 1994), Reynolds (1993), Jacobson and Reynolds (1993; 1995; 1998), Moin and Bewley (1994), Gad-el-Hak (1994; 1996; 1998), McMichael (1996), Mehregany et al. (1996), and Lumley and Blossey (1998). Special mention should also be made of the UCLA/Caltech team who has been very effective in developing many MEMS-based sensors and actuators for turbulence diagnosis and control. Their list of publications in the field is rather long, but see, for example, Ho and Tai (1996), Tsao et al. (1997), Ho et al. (1997), Ho and Tai (1998), and references therein.

It is instructive to estimate some representative characteristics of the required array of sensors/actuators. Consider a typical commercial aircraft cruising at a speed of $U_\infty = 300$ m/s and at an altitude of 10 km. The density and kinematic viscosity of air and the unit Reynolds number in this case are, respectively, $\rho = 0.4$ kg/m^3, $\nu = 3 \times 10^{-5}$ m^2/s, and Re $= 10^7$/m. Assume further that the portion of fuselage to be controlled has a turbulent boundary layer characteristics which are identical to those for a zero-pressure-gradient flat plate at a distance of 1 m from the leading edge. In this case, the skin-friction coefficient and the friction velocity are, respectively, $C_f = 0.003$ and $u_\tau = 11.62$ m/s. (Note that the skin friction decreases as the distance from the leading edge increases. It is also strongly affected by such things as the externally imposed pressure gradient. Therefore, the estimates provided in here are for illustration purposes only.) At this location, one viscous wall unit is only $\nu/u_\tau = 2.6$ microns. In order for the surface array of sensors/actuators to be hydraulically smooth, it should not protrude beyond the viscous sublayer, or $5\nu/u_\tau = 13$ μm.

Wall-speed streaks are the most visible, reliable and detectable indicators of the preburst turbulence production process. The detection criterion is simply low velocity near the wall, and the actuator response should be to accelerate (or to remove) the low-speed region before it breaks down. Local wall motion, tangential injection, suction or heating triggered on sensed wall-pressure or wall-shear stress could be used to cause local acceleration of near-wall fluid.

The recent numerical experiments of Berkooz et al. (1993) indicate that effective control of bursting pair of rolls may be achieved by using the equivalent of two wall-mounted shear sensors. If the goal is to stabilize or to eliminate all low-speed streaks in the boundary layer, a reasonable estimate for the spanwise and streamwise distances between individual elements of a checkerboard array is, respectively, 100 and 1000 wall units or 260 μm and 2600 μm, for our particular example. (Note that 100 and 1000 wall units are equal to, respectively, the average spanwise wavelength between two adjacent streaks and the average streamwise extent for a typical low-speed region. One can argue that those estimates are too conservative: once a region is relaminarized, it would perhaps stay as such for quite a while as the flow convects downstream. The next row of sensors/actuators may therefore be relegated to a downstream location well beyond 1000 wall units.) A reasonable size for each element is probably one-tenth of the spanwise separation, or 26 μm. A (1 m $\times$ 1 m) portion of the surface would have to be covered with about $n = 1.5$ million elements. This is a colossal number, but the density of sensors/actuators can be considerably reduced if we moderate our goal of targeting every single bursting event (and also if less conservative assumptions are used).

It is well known that not every low-speed streak leads to a burst. On the average, a particular sensor would detect an incipient bursting event every wall-unit interval of $P^+ = Pu_\tau^2/\nu =$

250, or $P = 56\ \mu$s. The corresponding dimensionless and dimensional frequencies are $f^+ = 0.004$ and $f = 18$ kHz, respectively. At different distances from the leading edge and in the presence of nonzero pressure-gradient, the sensors/actuators array would have different characteristics, but the corresponding numbers would still be in the same ballpark as estimated in here.

As a second example, consider an underwater vehicle moving at a speed of $U_\infty = 10$ m/s. Despite the relatively low speed, the unit Reynolds number is still the same as estimated above for the air case, Re $= 10^7$/m, due to the much lower kinematic viscosity of water. At one meter from the leading edge of an imaginary flat plate towed in water at the same speed, the friction velocity is only $u_\tau = 0.39$ m/s, but the wall unit is still the same as in the aircraft example, $\nu/u_\tau = 2.6\ \mu$m. The density of required sensors/actuators array is the same as computed for the aircraft example, $n = 1.5 \times 10^6$ elements/m^2. The anticipated average frequency of sensing a bursting event is, however, much lower at $f = 600$ Hz.

Similar calculations have also been made by Gad-el-Hak (1993; 1994), Reynolds (1993), and Wadsworth et al. (1993). Their results agree closely with the estimates made here for typical field requirements. In either the airplane or the submarine case, the actuator's response need not be too large. As will be shown in Section 3.3.5, wall displacement on the order of 10 wall units (26 μm in both examples), suction coefficient of about 0.0006, or surface cooling/heating on the order of 40°C/2°C (in the first/second example, respectively) should be sufficient to stabilize the turbulent flow.

As computed in the two examples above, both the required size for a sensor/actuator element and the average frequency at which an element would be activated are within the presently known capabilities of microfabrication technology. The number of elements needed per unit area is, however, alarmingly large. The unit cost of manufacturing a programmable sensor/actuator element would have to come down dramatically, perhaps matching the unit cost of a conventional transistor, before the idea advocated in here would become practical.

An additional consideration to the size, amplitude, and frequency response is the energy consumed by each sensor/actuator element. Total energy consumption by the entire control system obviously has to be low enough to achieve net savings. Consider the following calculations for the aircraft example. One meter from the leading edge, the skin-friction drag to be reduced is approximately 54 N/m^2. Engine power needed to overcome this retarding force per unit area is 16 kW/m^2, or $10^4\ \mu$W/sensor. If a 60% drag-reduction is achieved, this energy consumption is reduced to 4320 μW/sensor. This number will increase by the amount of energy consumption of a sensor/actuator unit, but hopefully not back to the uncontrolled levels. The voltage across a sensor is typically in the range of $V = 0.1$–1 V, and its resistance in the range of $R = 0.1$–1 MΩ. This means a power consumption by a typical sensor in the range of $\mathcal{P} = V^2/R = 0.1$–$10\ \mu$W, well below the anticipated power savings due to reduced drag. For a single actuator in the form of a spring-loaded diaphragm with a spring constant of $k = 100$ N/m, oscillating up and down at the bursting frequency of $f = 18$ kHz, with an amplitude of $y = 26$ microns, the power consumption is $\mathcal{P} = (\frac{1}{2})ky^2 f = 600\ \mu$W/actuator. If suction is used instead, $C_q = 0.0006$, and assuming a pressure difference of $\Delta p = 10^4$ N/m^2 across the suction holes/slots, the corresponding power consumption for a single actuator is $\mathcal{P} = C_q U_\infty \Delta p/n = 1200\ \mu$W/actuator. It is clear then that when the power penalty for the sensor/actuator is added to the lower-level drag, a net saving is still achievable. The corresponding actuator power penalties for the submarine example are even smaller ($\mathcal{P} = 20\ \mu$W/actuator, for the wall motion actuator, and $\mathcal{P} = 40\ \mu$W/actuator, for the suction actuator), and larger savings are therefore possible.

3.3.5 Microdevices for Flow Control. MEMS integrates electronics and mechanical components and can therefore execute sense-decision-actuation on a monolithic level. Microsensors/microactuators would be ideal for the reactive flow control concept advocated in the present subsection. Methods of flow control targeted toward specific coherent structures involve nonintrusive detection and subsequent modulation of events that occur randomly in space and time. To achieve proper targeted control of these quasi-periodic vortical events, temporal phasing as well as spatial selectivity are required. Practical implementation of such an idea necessitates the use of a large number of intelligent, communicative wall sensors and actuators arranged in a checkerboard pattern. Section 3.3.4 provided estimates for the number, characteristics and energy consumption of such elements required to modulate the turbulent boundary layer which develops along a typical commercial aircraft or nuclear submarine. An upper-bound number to achieve total turbulence suppression is about one million sensors/actuators per square meter of the surface, although as argued earlier the actual number needed to achieve effective control could perhaps be one or two orders of magnitude below that.

The sensors would be expected to measure the amplitude, location, and phase or frequency of the signals impressed upon the wall by incipient bursting events. Instantaneous wall-pressure or wall-shear stress can be sensed, for example. The normal or in-plane motion of a minute membrane is proportional to the respective point force of primary interest. For measuring wall pressure, microphone-like devices respond to the motion of a vibrating surface membrane or an internal elastomer. Several types are available including variable-capacitance (condenser or electret), ultrasonic, optical (e.g., optical-fiber and diode-laser), and piezoelectric devices (see, for example, Löfdahl et al., 1993; 1994). A potentially useful technique for our purposes has been tried at MIT (Warkentin et al., 1987; Young et al., 1988; Haritonidis et al., 1990a; 1990b). An array of extremely small (0.2 mm in diameter) laser-powered microphones (termed picophones) was machined in silicon using integrated circuit fabrication techniques, and was used for field measurement of the instantaneous surface pressure in a turbulent boundary layer. The wall-shear stress, though smaller and therefore more difficult to measure than pressure, provides a more reliable signature of the near-wall events.

Actuators are expected to produce a desired change in the targeted coherent structures. The local acceleration action needed to stabilize an incipient bursting event can be in the form of adaptive wall, transpiration or wall heat transfer. Traveling surface waves can be used to modify a locally convecting pressure gradient such that the wall motion follows that of the coherent event causing the pressure change. Surface motion in the form of a Gaussian hill with height $y^+ = \mathcal{O}[10]$ should be sufficient to suppress typical incipient bursts (Lumley, 1991; Carlson and Lumley, 1996). Such time-dependent alteration in wall geometry can be generated by driving a flexible skin using an array of piezoelectric devices (dilate or contract depending on the polarity of current passing through them), electromagnetic actuators, magnetoelastic ribbons (made of nonlinear materials that change their stiffness in the presence of varying magnetic fields), or Terfenol-d rods (a novel metal composite, developed at Grumman Corporation, which changes its length when subjected to a magnetic field). Note should also be made of other exotic materials that can be used for actuation. For example, electrorheological fluids (Halsey and Martin, 1993) instantly solidify when exposed to an electric field, and may thus be useful for the present application. Recently constructed microactuators specifically designed for flow control include those by Wiltse and Glezer (1993), James et al. (1994), Jacobson and Reynolds (1993; 1995; 1998), and Vargo and Muntz (1996).

Suction/injection at many discrete points can be achieved by simply connecting a large number of minute streamwise slots, arranged in a checkerboard pattern, to a low-pressure/high-pressure reservoir located underneath the working surface. The transpiration through each individual slot is turned on and off using a corresponding number of independently controlled microvalves. Alternatively, positive-displacement or rotary micropumps (see, for example, Sen et al., 1996; Sharatchandra et al., 1997) can be used for blowing or sucking fluid through small holes/slits. Based on the results of Gad-el-Hak and Blackwelder (1989), equivalent suction coefficients of about 0.0006 should be sufficient to stabilize the near-wall region. Assuming that the skin-friction coefficient in the uncontrolled boundary layer is $C_f = 0.003$, and assuming further that the suction used is sufficient to establish an asymptotic boundary layer ($d\delta_\theta/dx = 0$, where δ_θ is the momentum thickness), the skin friction in the reactively controlled case is then $C_f = 0 + 2C_q = 0.0012$, or 40% of the original value. The net benefit would, of course, be reduced by the energy expenditure of the suction pump (or micropumps) as well as the array of microsensors and microvalves.

Finally, if the bursting events are to be eliminated by lowering the near-wall viscosity, direct electric-resistance heating can be used in liquid flows and thermoelectric devices based on the Peltier effect can be used for cooling in the case of gaseous boundary layers. The absolute viscosity of water at 20°C decreases by approximately 2% for each 1°C rise in temperature, while for room-temperature air, μ decreases by approximately 0.2% for each 1°C drop in temperature. The streamwise momentum equation written at the wall can be used to show that a suction coefficient of 0.0006 has approximately the same effect on the wall-curvature of the instantaneous velocity profile as a surface heating of 2°C in water or a surface cooling of 40°C in air (Liepmann and Nosenchuck, 1982; Liepmann et al., 1982).

Sensors and actuators of the types discussed in this section can be combined on individual electronic chips using microfabrication technology. The chips can be interconnected in a communication network that is controlled by a massively parallel computer or a self-learning neural network, perhaps each sensor/actuator unit communicating only with its immediate neighbors. In other words, it may not be necessary for one sensor/actuator to exchange signals with another far away unit. Factors to be considered in an eventual field application of chips produced using microfabrication processes include sensitivity of sensors, sufficiency and frequency response of actuators' action, fabrication of large arrays at affordable prices, survivability in the hostile field environment, and energy required to power the sensors/actuators. As argued by Gad-el-Hak (1994), sensor/actuator chips currently produced are small enough for typical field application, and they can be programmed to provide a sufficiently large/fast action in response to a certain sensor output (see also Jacobson and Reynolds, 1995). Present prototypes are, however, still quite expensive as well as delicate. But so was the transistor when first introduced! It is hoped that the unit price of future sensor/actuator elements would follow the same dramatic trends witnessed in case of the simple transistor and even the much more complex integrated circuit. The price anticipated by Texas Instruments for an array of 0.5–2 million, individually actuated mirrors used in high-definition optical displays hints that the technology is well in its way to mass-produce phenomenally inexpensive microsensors and microactuators. Additionally, current automotive applications are a rigorous proving ground for MEMS: under-the-hood sensors can already withstand harsh conditions such as intense heat, shock, continual vibration, corrosive gases and electromagnetic fields.

3.4 Micropumps. There have been several studies of microfabricated pumps. Some of them use non-mechanical effects. The Knudsen pump mentioned in Section 2.5 uses the thermal-creep effect to move rarefied gases from one chamber to another. Ion-drag is used in electrohydrodynamic pumps (Bart et al., 1990; Richter et al., 1991; Fuhr et al., 1992); these rely on the electrical properties of the fluid and are thus not suitable for many applications. Valveless pumping by ultrasound has also been proposed (Moroney et al., 1991), but produces very little pressure difference.

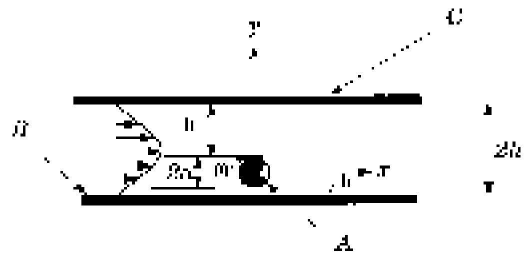

Fig. 15 Schematic of micropump developed by Sen et al. (1996)

Mechanical pumps based on conventional centrifugal or axial turbomachinery will not work at micromachine scales where the Reynolds numbers are typically small, on the order of 1 or less. Centrifugal forces are negligible and, furthermore, the Kutta condition through which lift is normally generated is invalid when inertial forces are vanishingly small. In general there are three ways in which mechanical micropumps can work:

1. Positive-displacement pumps. These are mechanical pumps with a membrane or diaphragm actuated in a reciprocating mode and with unidirectional inlet and outlet valves. They work on the same physical principle as their larger cousins. Micropumps with piezoelectric actuators have been fabricated (Van Lintel et al., 1988; Esashi et al., 1989; Smits, 1990). Other actuators, such as thermopneumatic, electrostatic, electromagnetic or bimetallic, can be used (Pister et al., 1990; Döring et al., 1992; Gabriel et al., 1992). These exceedingly minute positive-displacement pumps require even smaller valves, seals and mechanisms, a not-too-trivial micromanufacturing challenge. In addition there are long-term problems associated with wear or clogging and consequent leaking around valves. The pumping capacity of these pumps is also limited by the small displacement and frequency involved. Gear pumps are a different kind of positive-displacement device.
2. Continuous, parallel-axis rotary pumps. A screw-type, three-dimensional device for low Reynolds numbers was proposed by Taylor (1972) for propulsion purposes and shown in his seminal film. It has an axis of rotation parallel to the flow direction implying that the powering motor must be submerged in the flow, the flow turned through an angle, or that complicated gearing would be needed.
3. Continuous, transverse-axis rotary pumps. This is the class of machines that was recently developed by Sen et al. (1996). They have shown that a rotating body, asymmetrically placed within a duct, will produce a net flow due to viscous action. The axis of rotation can be perpendicular to the flow direction and the cylinder can thus be easily powered from outside a duct. A related viscous-flow pump was designed by Odell and Kovasznay (1971) for a water channel with density stratification. However, their design operates at a much higher Reynolds number and is too complicated for microfabrication.

As evidenced from the third item above, it is possible to generate axial fluid motion in open channels through the rotation of a cylinder in a viscous fluid medium. Odell and Kovasznay (1971) studied a pump based on this principle at high Reynolds numbers. Sen et al. (1996) carried out an experimental study of a different version of such a pump. The novel viscous pump, shown schematically in Fig. 15, consists simply of a transverse-axis cylindrical rotor eccentrically placed in a channel, so that the differential viscous resistance between the small and large gaps causes a net flow along the duct. The Reynolds numbers involved in Sen et al.'s work were low ($0.01 < \mathrm{Re} \equiv 2\omega a^2/\nu < 10$, where ω is the radian velocity of the rotor, and a is its radius), typical of microscale devices, but achieved using a macroscale rotor and a very viscous fluid. The bulk velocities obtained were as high as 10% of the surface speed of the rotating cylinder. Sen et al. (1996) have also tried cylinders with square and rectangular cross-sections, but the circular cylinder delivered the best pumping performance.

A finite-element solution for low-Reynolds-number, uniform flow past a rotating cylinder near an impermeable plane boundary has already been obtained by Liang and Liou (1995). However, a detailed two-dimensional Navier-Stokes simulations of the pump described above have been carried out by Sharatchandra et al. (1997), who extended the operating range of Re beyond 100. The effects of varying the channel height H and the rotor eccentricity ϵ have been studied. It was demonstrated that an optimum plate spacing exists and that the induced flow increases monotonically with eccentricity; the maximum flowrate being achieved with the rotor in contact with a channel wall. Both the experimental results of Sen et al. (1996) and the 2-D numerical simulations of Sharatchandra et al. (1997) have verified that, at $\mathrm{Re} < 10$, the pump characteristics are linear and therefore kinematically reversible. Sharatchandra et al. (1997; 1998a) also investigated the effects of slip flow on the pump performance as well as the thermal aspects of the viscous device. Wall slip does reduce the traction at the rotor surface and thus lowers the performance of the pump somewhat. However, the slip effects appear to be significant only for Knudsen numbers greater than 0.1, which is encouraging from the point of view of microscale applications.

In an actual implementation of the micropump, several practical obstacles need to be considered. Among those are the larger stiction and seal design associated with rotational motion of microscale devices. Both the rotor and the channel have a finite, in fact rather small, width. DeCourtye et al. (1998) numerically investigated the viscous micropump performance as the width of the channel W becomes exceedingly small. The bulk flow generated by the pump decreased as a result of the additional resistance to the flow caused by the side walls. However, effective pumping was still observed with extremely narrow channels. Finally, Shartchandra et al. (1998b) used a genetic algorithm to determine the optimum wall shape to maximize the micropump performance. Their genetic algorithm uncovered shapes that were nonintuitive but yielded vastly superior pump performance.

Though most of the micropump discussion above is of flow in the steady state, it should be possible to give the eccentric cylinder a finite number of turns or even a portion of a turn to displace a prescribed minute volume of fluid. Numerical computations will easily show the order of magnitude of the volume discharged and the errors induced by acceleration at the beginning of the rotation and deceleration at the end. Such system can be used for microdosage delivery in medical applications.

3.5 Microturbines. DeCourtye et al. (1998) have described the possible utilization of the inverse micropump device (Section 3.4) as a turbine. The most interesting application of such a microturbine would be as a microsensor for measuring exceedingly small flowrates on the order of nanoliter/s (i.e., microflow metering for medical and other applications).

The viscous pump described in Section 3.4 operates best at low Reynolds numbers and should therefore be kinematically reversible in the creeping-flow regime. A microturbine based on the same principle should, therefore, lead to a net torque in the presence of a prescribed bulk velocity. The results of three-dimensional numerical simulations of the envisioned microturbine are summarized in this subsection. The Reynolds number for the turbine problem is defined in terms of the bulk velocity, since the rotor surface speed is unknown in this case,

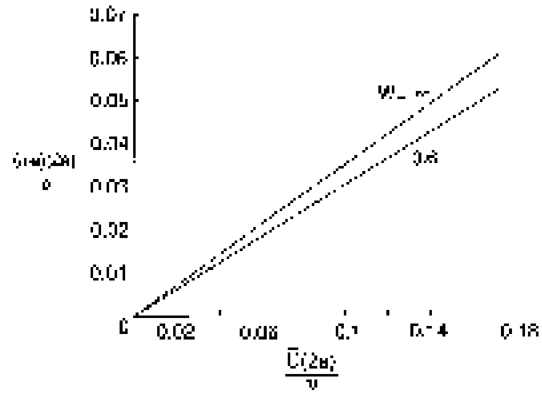

Fig. 16 Turbine rotation as a function of the bulk velocity in the channel. From DeCourtye et al. (1998).

$$\mathrm{Re} = \frac{\bar{U}(2a)}{\nu} \tag{78}$$

where $\bar{U}$ is the prescribed bulk velocity in the channel, a is the rotor radius, and ν is the kinematic viscosity of the fluid.

Figure 16 shows the dimensionless rotor speed as a function of the bulk velocity, for two dimensionless channel widths $W = \infty$ and $W = 0.6$. In these simulations, the dimensionless channel depth is $H = 2.5$ and the rotor eccentricity is $\epsilon/\epsilon_{\max} = 0.9$. The relation is linear as was the case for the pump problem. The slope of the lines is 0.37 for the 2-D turbine and 0.33 for the narrow channel with $W = 0.6$. This means that the induced rotor speed is, respectively, 0.37 and 0.33 of the bulk velocity in the channel. (The rotor speed can never, of course, exceed the fluid velocity even if there is no load on the turbine. Without load, the integral of the viscous shear stress over the entire surface area of the rotor is exactly zero, and the turbine achieves its highest albeit finite rpm.) For the pump, the corresponding numbers were 11.11 for the 2-D case and 100 for the 3-D case. Although it appears that the side walls have bigger influence on the pump performance, it should be noted that in the turbine case a vastly higher pressure drop is required in the 3-D duct to yield the same bulk velocity as that in the 2-D duct (dimensionless pressure drop of $\Delta p^* \equiv \Delta p 4a^2/\rho\nu^2 = -29$ versus $\Delta p^* = -1.5$).

The turbine characteristics are defined by the relation between the shaft speed and the applied load. A turbine load results in a moment on the shaft, which at steady state balances the torque due to viscous stresses. At a fixed bulk velocity, the rotor speed is determined for different loads on the turbine. Again, the turbine characteristics are linear in the Stokes (creeping) flow regime, but the side walls have weaker, though still adverse, effect on the device performance as compared to the pump case. For a given bulk velocity, the rotor speed drops linearly as the external load on the turbine increases. At large enough loads, the rotor will not spin, and maximum rotation is achieved when the turbine is subjected to zero load.

At present it is difficult to measure flowrates on the order of 10^{-12} m^3/s (1 nanoliter/s). One possible way is to directly collect the effluent over time. This is useful for calibration but is not practical for on-line flow measurement. Another is to use heat transfer from a wire or film to determine the local flowrate as in a thermal anemometer. Heat transfer from slowly moving fluids is mainly by conduction so that temperature gradients can be large. This is undesirable for biological and other fluids easily damaged by heat. The viscous mechanism that has been proposed and verified for pumping may be turned around and used for measuring. As demonstrated in this subsection, a freely rotating cylinder eccentrically placed in a duct will rotate at a rate proportional to the flowrate due to a turbine effect. In fact other geometries such as a freely rotating sphere in a cylindrical tube should also behave similarly. The calibration constant, which depends on system parameters such as geometry and bearing friction, should be determined computationally to ascertain the practical viability of such a microflow meter. Geometries that are simplest to fabricate should be explored and studied in detail.

3.6 Microbearings. Many of the micromachines use rotating shafts and other moving parts which carry a load and need fluid bearings for support, most of them operating with air or water as the lubricating fluid. The fluid mechanics of these bearings are very different compared to that of their larger cousins. Their study falls in the area of microfluid mechanics, an emerging discipline which has been greatly stimulated by its applications to micromachines and which is the subject of this paper.

Macroscale journal bearings develop their load-bearing capacity from large pressure differences which are a consequence of the presence of a viscous fluid, an eccentricity between the shaft and its housing, a large surface speed of the shaft, and a small clearance to diameter ratio. Several closed-form solutions of the no-slip flow in a macrobearing have been developed. Wannier (1950) used modified Cartesian coordinates to find an exact solution to the biharmonic equation governing two-dimensional journal bearings in the no-slip, creeping flow regime. Kamal (1966) and Ashino and Yoshida (1975) worked in bipolar coordinates; they assumed a general form for the streamfunction with several constants which were determined using the boundary conditions. Though all these methods work if there is no slip, they cannot be readily adapted to slip flow. The basic reason is that the flow pattern changes if there is slip at the walls and the assumed form of the solution is no longer valid.

Microbearings are different in the following aspects: (1) being so small, it is difficult to manufacture them with a clearance that is much smaller than the diameter of the shaft; (2) because of the small shaft size, its surface speed, at normal rotational speeds, is also small; and (3) air bearings in particular may be small enough for non-continuum effects to become important. (The microturbomachines being developed presently at MIT operate at shaft rotational speeds on the order of 1 million rpm, and are therefore operating at different flow regime from that considered here.) For these reasons the hydrodynamics of lubrication is very different at microscales. The lubrication approximation that is normally used is no longer directly applicable and other effects come into play. From an analytical point of view there are three consequences of the above: fluid inertia is negligible, slip flow may be important for air and other gases, and relative shaft clearance need not be small.

In a recent study, Maureau et al. (1997) analyzed microbearings represented as an eccentric cylinder rotating in a stationary housing. The flow Reynolds number is assumed small, the clearance between shaft and housing is not small relative to the overall bearing dimensions, and there is slip at the walls due to nonequilibrium effects. The two-dimensional governing equations are written in terms of the streamfunction in bipolar coordinates. Following the method of Jeffery (1920), Maureau et al. (1997) succeeded in obtaining an exact infinite-series solution of the Navier-Stokes equations for the specified geometry and flow conditions. In contrast to macrobearings and due to the large clearance, flow in a microbearing is characterized by the possibility of a recirculation zone which strongly affects the velocity and pressure fields. For high values of the eccentricity and low slip factors the flow develop a recirculation region, as shown in the streamlines plot in Fig. 17.

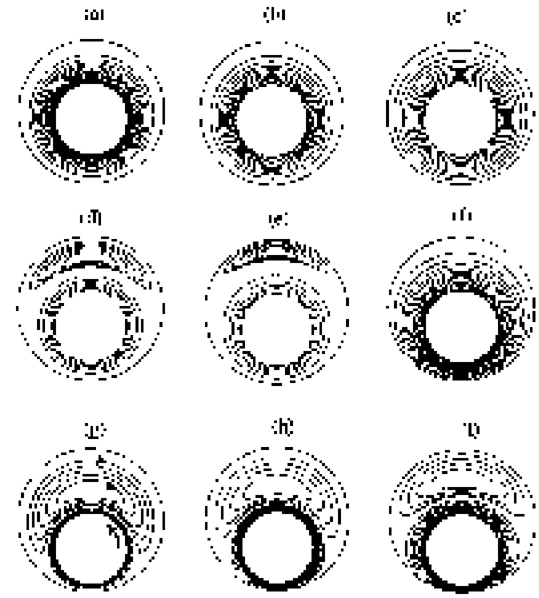

Fig. 17 Effect of slip factor and eccentricity on the microbearing streamlines. From top to bottom, eccentricity changes as $\epsilon = 0.2, 0.5, 0.8$. From left to right, slip factor changes as $S \equiv (2 - \sigma_v/\sigma)Kn = 0, 0.1, 0.5$. From Maureau et al. (1997).

From the infinite-series solution the frictional torque and the load-bearing capacity can be determined. The results show that both are similarly affected by the eccentricity and the slip factor: they increase with the former and decrease with the latter. For a given load, there is a corresponding eccentricity which generates a force sufficient to separate shaft from housing (i.e. sufficient to prevent solid-to-solid contact). As the load changes the rotational center of the shaft shifts a distance necessary for the forces to balance. It is interesting to note that for a weight that is vertically downwards, the equilibrium displacement of the center of the shaft is in the horizontal direction. This can lead to complicated rotor dynamics governed by mechanical inertia, viscous damping and pressure forces. A study of this dynamics may of interest. Real microbearings have finite shaft lengths, and end walls and other three-dimensional effects influence the bearing characteristics. Numerical simulations of the three-dimensional problem can readily be carried out and may also be of interest to the designers of microbearings. Other potential research includes determination of a criterion for onset of cavitation in liquid bearings. From the results of these studies, information related to load, rotational speed and geometry can be generated that would be useful for the designer.

Finally, Piekos et al. (1997) have used full Navier-Stokes computations to study the stability of ultra-high-speed, gas microbearings. They conclude that it is possible—despite significant design constraints—to attain stability for specific bearings to be used with the MIT microturbomachines (Epstein and Senturia, 1997; Epstein et al., 1997), which incidentally operate at much higher Reynolds numbers (and rpm) than the micropumps/microturbines/microbearings considered thus far in this and the previous two subsections. According to Piekos et al. (1997), high-speed bearings are more robust than low-speed ones due to their reduced running eccentricities and the large loads required to maintain them.

4 Concluding Remarks

The forty-year-old vision of Richard Feynman of building minute machines is now a reality. Microelectromechanical systems have witnessed explosive growth during the last decade and are finding increased applications in a variety of industrial and medical fields. The physics of fluid flows in microdevices and some representative applications have been explored in this paper. While we now know a lot more than we did just few years ago, much physics remains to be explored so that rational tools can be developed for the design, fabrication and operation of MEMS devices.

The traditional Navier-Stokes model of fluid flows with no-slip boundary conditions works only for a certain range of the governing parameters. This model basically demands two conditions. (1) The fluid is a continuum, which is almost always satisfied as there are usually more than 1 million molecules in the smallest volume in which appreciable macroscopic changes take place. This is the molecular chaos restriction. (2) The flow is not too far from thermodynamic equilibrium, which is satisfied if there is sufficient number of molecular encounters during a time period small compared to the smallest time-scale for flow changes. During this time period the average molecule would have moved a distance small compared to the smallest flow length-scale.

For gases, the Knudsen number determines the degree of rarefaction and the applicability of traditional flow models. As $Kn \rightarrow 0$, the time- and length-scales of molecular encounters are vanishingly small compared to those for the flow, and the velocity distribution of each element of the fluid instantaneously adjusts to the equilibrium thermodynamic state appropriate to the local macroscopic properties as this molecule moves through the flow field. From the continuum viewpoint, the flow is isentropic and heat conduction and viscous diffusion and dissipation vanish from the continuum conservation relations, leading to the Euler equations of motion. At small but finite Kn, the Navier-Stokes equations describe near-equilibrium, continuum flows.

Slip flow must be taken into account for $Kn > 0.001$. The slip boundary condition is at first linear in Knudsen number then nonlinear effects take over beyond a Knudsen number of 0.1. At the same transition regime, i.e., $0.1 < Kn < 10$, the linear (stress)-(rate of strain) and (heat flux)-(temperature gradient) relations—needed to close the Navier-Stokes equations—also break down, and alternative continuum equations (e.g., Burnett) or molecular-based models must be invoked. In the transition regime, provided that the dilute gas and molecular chaos assumptions hold, solutions to the difficult Boltzmann equation are sought, but physical simulations such as Monte Carlo methods are more readily executed in this range of Knudsen number. In the free-molecule flow regime, i.e., $Kn > 10$, the nonlinear collision integral is negligible and the Boltzmann equation is drastically simplified. Analytical solutions are possible in this case for simple geometries and numerical integration of the Boltzmann equation is straightforward for arbitrary geometries, provided that the surface-reflection characteristics are accurately modeled.

Gaseous flows are often compressible in microdevices even at low Mach numbers. Viscous effects can cause sufficient pressure drop and density changes for the flow to be treated as compressible. In a long, constant-area microduct, all Knudsen number regimes may be encountered and the degree of rarefaction increases along the tube. The pressure drop is nonlinear and the Mach number increases downstream, limited only by choked-flow condition.

Similar deviation and breakdown of the traditional Navier-Stokes equations occur for liquids as well, but there the situation is more murky. Existing experiments are contradictory. There is no kinetic theory of liquids, and first-principles prediction methods are scarce. Molecular dynamics simulations can be used, but they are limited to extremely small flow extents. Nevertheless, measurable slip is predicted from MD simulations at realistic shear rates in microdevices.

MEMS are finding increased applications in the diagnosis and control of turbulent flows. The use of microsensors and microactuators promises a quantum leap in the performance of reactive flow control systems, and is now in the realm of the possible for future practical devices. Simple, viscous-based micropumps can be utilized for microdosage delivery, and microturbines can be used for measuring flowrates in the nanoliter/s range. Both of these can be of value in several medical applications.

Much nontraditional physics is still to be learned and many exciting applications of microdevices are yet to be discovered. The future is bright for this emerging field of science and technology and members of the American Society of Mechanical Engineers should be in the forefront of this progress. Richard Feynman was right about the possibility of building mite-size machines, but was somewhat cautious in forecasting that such machines, while ''would be fun to make,'' may or may not be useful.

Acknowledgments

My original involvement with microdevices was performed under a contract from the National Science Foundation, under the Small Grants for Exploratory Research initiative (SGER Grant no. CTS-95-21612). The technical monitors were Robert Powell and Roger Arndt. I would like to express my sincere appreciation to the members of the ASME Freeman Scholar committee, Richard Bajura, Clayton Crowe and Michael Billet, for their confidence in my ability to deliver this treatise. I am very grateful to Chih-Ming Ho, Fazle Hussain and George Karniadakis for their continuous support and encouragement through the years. Haim Bau, Ali Beskok, Kenneth Breuer, Stuart Jacobson and Sandra Troian provided invaluable help in preparing this manuscript, including sharing some of their reports and papers. Finally, my sincere gratitude to my friend and colleague Mihir Sen, for all the great times we have had while working together on small devices and big ideas.

References

Alder, B. J., and Wainwright, T. E., 1957, ''Studies in Molecular Dynamics,'' *Journal of Chemical Physics,* Vol. 27, pp. 1208–1209.

Alder, B. J., and Wainwright, T. E., 1958, ''Molecular Dynamics by Electronic Computers,'' *Transport Processes in Statistical Mechanics,* I. Prigogine, ed., pp. 97–131, Interscience, New York.

Alder, B. J., and Wainwright, T. E., 1970, ''Decay of the Velocity Auto-Correlation Function,'' *Physical Review A,* Vol. 1, pp. 18–21.

Allen, M. P., and Tildesley, D. J., 1987, *Computer Simulation of Liquids,* Clarendon Press, Oxford, England.

Amato, I., 1998, ''Formenting a Revolution, in Miniature,'' *Science,* Vol. 282, No. 5388, 16 October, pp. 402–405.

Anderson, J. L., and Quinn, J. A., 1972, ''Ionic Mobility in Microcapillaries,'' *Journal of Chemical Physics,* Vol. 27, pp. 1208–1209.

Angell, J. B., Terry, S. C., and Barth, P. W., 1983, ''Silicon Micromechanical Devices,'' *Faraday Transactions I,* Vol. 68, pp. 744–748.

Arkilic, E. B., 1997, ''Measurement of the Mass Flow and Tangential Momentum Accommodation Coefficient in Silicon Micromachined Channels,'' Ph.D. thesis, Massachusetts Institute of Technology, Cambridge, Massachusetts.

Arkilic, E. B., Schmidt, M. A., and Breuer, K. S., 1995, ''Slip Flow in Microchannels,'' *Rarefied Gas Dynamics 19,* J. Harvey and G. Lord, eds., Oxford University Press, Oxford, United kingdom.

Arkilic, E. B., Schmidt, M. A., and Breuer, K. S., 1997a, ''Gaseous Slip Flow in Long Microchannels,'' *Journal of Microelectromechanical Systems,* Vol. 6, pp. 167–178.

Arkilic, E. B., Schmidt, M. A., and Breuer, K. S., 1997b, ''TMAC Measurement in Silicon Micromachined Channels,'' *Rarefied Gas Dynamics 20,* C. Shen, ed., 6 pp., Beijing University Press, Beijing, China.

Ashino, I., and Yoshida, K., 1975, ''Slow Motion between Eccentric Rotating Cylinders,'' *Bulletin of the JSME,* Vol. 18, No. 117, pp. 280–285.

Atwood, B. T., and Schowalter, W. R., 1989, ''Measurements of Slip at the Wall during Flow of High-Density Polyethylene through a Rectangular Conduit,'' *Rheologica Acta,* Vol. 28, p. 134–146.

Bandyopadhyay, P. R., 1986, ''Review—Mean Flow in Turbulent Boundary Layers Disturbed to Alter Skin Friction,'' ASME Journal of Fluids Engineering, Vol. 108, pp. 127–140.

Bart, S. F., Tavrow, L. S., Mehregany, M., and Lang, J. H., 1990, ''Microfabricated Electrohydrodynamic Pumps,'' *Sensors and Actuators A,* Vol. 21–23, pp. 193–197.

Batchelor, G. K., 1967, *An Introduction to Fluid Dynamics,* Cambridge University Press, London, United Kingdom.

Bau, H. H., 1994, ''Transport Processes Associated with Micro-Devices,'' *Thermal Science and Engineering,* Vol. 2, pp. 172–178.

Berkooz, G., Fisher, M., and Psiaki, M., 1993, ''Estimation and Control of Models of the Turbulent Wall Layer,'' *Bulletin of the American Physical Society,* Vol. 38, p. 2197.

Beskok, A., 1994, ''Simulation of Heat and Momentum Transfer in Complex Micro-Geometries,'' M.Sc. thesis, Princeton University, Princeton, New Jersey.

Beskok, A., 1996, ''Simulations and Models of Gas Flows in Microgeometries,'' Ph.D. thesis, Princeton University, Princeton, New Jersey.

Beskok, A., and Karniadakis, G. E., 1994, ''Simulation of Heat and Momentum Transfer in Complex Micro-Geometries,'' *Journal of Thermophysics and Heat Transfer,* Vol. 8, pp. 355–370.

Beskok, A., and Karniadakis, G. E., 1998, ''A Model for Flows in Channels, Pipes and Ducts at Micro- and Nano-Scales,'' *Microscale Thermophysicsl Engineering,* to appear.

Beskok, A., Karniadakis, G. E., and Trimmer, W., 1996, ''Rarefaction and Compressibility Effects in Gas Microflows,'' ASME Journal of Fluids Engineering, Vol. 118, pp. 448–456.

Bhatnagar, P. L., Gross, E. P., and Krook, M., 1954, ''A Model for Collision Processes in Gases. I. Small Amplitude Processes in Charged and Neutral One-Component Systems,'' *Physical Review,* Vol. 94, pp. 511–524.

Bird, G. A., 1963, ''Approach to Translational Equilibrium in a Rigid Sphere Gas,'' *Physics of Fluids,* Vol. 6, pp. 1518–1519.

Bird, G. A., 1965, ''The Velocity Distribution Function within a Shock Wave,'' *Journal of Fluid Mechanics,* Vol. 30, pp. 479–487.

Bird, G. A., 1976, *Molecular Gas Dynamics,* Clarendon Press, Oxford, United Kingdom.

Bird, G. A., 1978, ''Monte Carlo Simulation of Gas Flows,'' *Annual Review of Fluid Mechanics,* Vol. 10, pp. 11–31.

Bird, G. A., 1994, *Molecular Gas Dynamics and the Direct Simulation of Gas Flows,* Clarendon Press, Oxford, United Kingdom.

Blackwelder, R. F., and Gad-el-Hak M., 1990, ''Method and Apparatus for Reducing Turbulent Skin Friction,'' United States Patent No. 4,932,612.

Bryzek, J., Peterson, K., and McCulley, W., 1994, ''Micromachines on the March,'' *IEEE Spectrum,* Vol. 31, May, pp. 20–31.

Brunauer, S., 1944, *Physical Adsorption of Gases and Vapours,* Oxford University Press, Oxford, United Kingdom.

Busch-Vishniac, I. J., 1998, ''Trends in Electromechanical Transduction,'' *Physics Today,* Vol. 51, July, pp. 28–34.

Cantwell, B. J., 1981, ''Organized Motion in Turbulent Flow,'' *Annual Review of Fluid Mechanics,* Vol. 13, pp. 457–515.

Carlson, H. A., and Lumley, J. L., 1996, ''Flow over an Obstacle Emerging from the Wall of a Channel,'' *AIAA Journal,* Vol. 34, pp. 924–931.

Cercignani, C., 1988, *The Boltzmann Equation and Its Applications,* Springer-Verlag, Berlin.

Chan, D. Y. C., and Horn, R. G., 1985, ''Drainage of Thin Liquid Films,'' *Journal of Chemical Physics,* Vol. 83, pp. 5311–5324.

Chapman, S., and Cowling, T. G., 1970, *The Mathematical Theory of Non-Uniform Gases,* Third Edition, Cambridge University Press, London, United Kingdom.

Cheng, H. K., 1993, ''Perspectives on Hypersonic Viscous Flow Research,'' *Annual Review of Fluid Mechanics,* Vol. 25, pp. 455–484.

Cheng, H. K., and Emmanuel, G., 1995, ''Perspectives on Hypersonic Nonequilibrium Flow,'' *AIAA Journal,* Vol. 33, pp. 385–400.

Choi, H., Moin, P., and Kim, J., 1992, ''Turbulent Drag Reduction: Studies of Feedback Control and Flow Over Riblets,'' Department of Mechanical Engineering Report No. TF-55, Stanford University, Stanford, CA.

Choi, H., Moin, P., and Kim, J., 1994, ''Active Turbulence Control for Drag Reduction in Wall-Bounded Flows,'' *Journal of Fluid Mechanics,* Vol. 262, pp. 75–110.

Ciccotti, G., and Hoover, W. G. (editors), 1986, *Molecular Dynamics Simulation of Statistical Mechanics Systems,* North Holland, Amsterdam, the Netherlands.

Debye, P., and Cleland, R. L., 1959, ''Flow of Liquid Hydrocarbons in Porous Vycor,'' *Journal of Applied Physics,* Vol. 30, pp. 843–849.

DeCourtye, D., Sen, M., and Gad-el-Hak, M., 1998, ''Analysis of Viscous Micropumps and Microturbines,'' *International Journal of Computational Fluid Dynamics,* Vol. 10, pp. 13–25.

Den, L. M., 1990, ''Issues in Viscoelastic Fluid Mechanics,'' *Annual Review of Fluid Mechanics,* Vol. 22, pp. 13–34.

Döring, C., Grauer, T., Marek, J., Mettner, M. S., Trah, H.-P., and Willmann, M., 1992, ''Micromachined Thermoelectrically Driven Cantilever Structures for Fluid Jet Deflection,'' *Proceedings IEEE Micro Electro Mechanical Systems '92,* pp. 12–18, 4–7 February, Travemünde, Germany.

Dussan, E. B., 1976, ''The Moving Contact Line: the Slip Boundary Condition,'' *Journal of Fluid Mechanics,* Vol. 77, pp. 665–684.

Dussan, E. B., 1979, ''On the Spreading of Liquids on Solid Surfaces: Static and Dynamic Contact Lines,'' *Annual Review of Fluid Mechanics,* Vol. 11, pp. 371–400.

Dussan, E. B., and Davis, S. H., 1974, ''On the Motion of Fluid-Fluid Interface along a Solid Surface,'' *Journal of Fluid Mechanics,* Vol. 65, pp. 71–95.

Epstein, A. H., and Senturia, S. D., 1997, ''Macro Power from Micro Machinery,'' *Science,* Vol. 276, 23 May, p. 1211.

Epstein, A. H., Senturia, S. D., Al-Midani, O., Anathasuresh, G., Ayon, A., Breuer, K., Chen, K.-S., Ehrich, F. F., Esteve, E., Frechette, L., Gauba, G., Ghodssi, R., Groshenry, C., Jacobson, S. A., Kerrebrock, J. L., Lang, J. H., Lin, C.-C., London, A., Lopata, J., Mehra, A., Mur Miranda, J. O., Nagle, S., Orr, D. J., Piekos, E., Schmidt, M. A., Shirley, G., Spearing, S. M., Tan, C. S., Tzeng, Y.-S., and Waitz, I. A. (1997), ''Micro-Heat Engines, Gas Turbines, and Rocket Engines—The MIT Microengine Project,'' AIAA paper No. 97-1773, AIAA, Reston, VA.

Esashi, M., Shoji, S., and Nakano, A., 1989, ''Normally Closed Microvalve Fabricated on a Silicon Wafer,'' *Sensors and Actuators,* Vol. 20, pp. 163–169.

Fan, L.-S., Tai, Y.-C., and Muller, R. S., 1988, ''Integrated Movable Micromechanical Structures for Sensors and Actuators,'' *IEEE Transactions on Electronic Devices,* Vol. 35, pp. 724–730.

Fan, L.-S., Tai, Y.-C., and Muller, R. S., 1989, ''IC-Processed Electrostatic Micromotors,'' *Sensors and Actuators,* Vol. 20, pp. 41–47.

Feynman, R. P., 1961, ''There's Plenty of Room at the Bottom,'' *Miniaturization,* H. D. Gilbert, ed., pp. 282–296, Reinhold Publishing, New York.

Fiedler, H. E., and Fernholz, H.-H., 1990, ''On Management and Control of Turbulent Shear Flows,'' *Progress in Aerospace Sciences,* Vol. 27, pp. 305–387.

Fuhr, G., Hagedorn, R., Müller, T., Benecke, W., and Wagner, B., 1992, ''Microfabricated Electrohydrodynamic (EHD) Pumps for Liquids of Higher Conductivity,'' *Journal of Microelectromechanical Systems,* Vol. 1, pp. 141–145.

Gabriel, K. J., 1995, ''Engineering Microscopic Machines,'' *Scientific American,* Vol. 260, Sept., pp. 150–153.

Gabriel, K. J., Jarvis, J., and Trimmer, W. (editors), 1988, *Small Machines, Large Opportunities: A Report on the Emerging Field of Microdynamics,* National Science Foundation, published by AT&T Bell Laboratories, Murray Hill, NJ.

Gabriel, K. J., Tabata, O., Shimaoka, K., Sugiyama, S., and Fujita, H., 1992, ''Surface-Normal Electrostatic/Pneumatic Actuator,'' *Proceedings IEEE Micro Electro Mechanical Systems '92,* pp. 128–131, 4–7 February, Travemünde, Germany.

Gad-el-Hak, M., 1989, ''Flow Control,'' *Applied Mechanics Reviews,* Vol. 42, pp. 261–293.

Gad-el-Hak, M., 1993, ''Innovative Control of Turbulent Flows,'' AIAA Paper No. 93-3268, AIAA, NY.

Gad-el-Hak, M., 1994, ''Interactive Control of Turbulent Boundary Layers: A Futuristic Overview,'' *AIAA Journal,* Vol. 32, pp. 1753–1765.

Gad-el-Hak, M., 1995, ''Questions in Fluid Mechanics: Stokes' Hypothesis for a Newtonian, Isotropic Fluid,'' ASME Journal of Fluids Engineering, Vol. 117, pp. 3–5.

Gad-el-Hak, M., 1996, ''Modern Developments in Flow Control,'' *Applied Mechanics Reviews,* Vol. 49, pp. 365–379.

Gad-el-Hak, M., 1998, ''Frontiers of Flow Control,'' *Flow Control: Fundamentals and Practices,* M. Gad-el-Hak, A. Pollard and J.-P. Bonnet, eds., *Lecture Notes in Physics,* Vol. 53, pp. 109–153, Springer-Verlag, Berlin.

Gad-el-Hak, M., and Blackwelder, R. F., 1987, ''A Drag Reduction Method for Turbulent Boundary Layers,'' AIAA Paper No. 87-0358, AIAA, New York.

Gad-el-Hak, M., and Blackwelder, R. F., 1989, ''Selective Suction for Controlling Bursting Events in a Boundary Layer,'' *AIAA Journal,* Vol. 27, pp. 308–314.

Garcia, E. J., and Sniegowski, J. J., 1993, ''The Design and Modelling of a Comb-Drive-Based Microengine for Mechanism Drive Applications,'' *Proceedings of the Seventh International Conference on Solid-State Sensors and Actuators (Transducers '93),* pp. 763–766, Yokohama, Japan, 7–10 June.

Garcia, E. J., and Sniegowski, J. J., 1995, ''Surface Micromachined Microengine,'' *Sensors and Actuators A,* Vol. 48, pp. 203–214.

Gee, M. L., McGuiggan, P. M., Israelachvili, J. N., and Homola, A. M., 1990, ''Liquid to Solidlike Transitions of Molecularly Thin Films under Shear,'' *Journal of Chemical Physics,* Vol. 93, pp. 1895–1906.

Gravesen, P., Branebjerg, J., and Jensen, O. S., 1993, ''Microfluidics—A Review,'' *Journal of Micromechanics and Microengineering,* Vol. 3, pp. 168–182.

Guvenc, M. G., 1985, ''V-Groove Capillary for Low Flow Control and Measurement,'' *Micromachining and Micropackaging of Transducers,* C. D. Fung, P. W. Cheung, W. H. Ko and D. G. Fleming, eds., pp. 215–223, Elsevier, Amsterdam, The Netherlands.

Haile, J. M., 1993, *Molecular Dynamics Simulation: Elementary Methods,* Wiley, New York.

Halsey, T. C., and Martin, J. E., 1993, ''Electrorheological Fluids,'' *Scientific American,* Vol. 269, Oct., pp. 58–64.

Haritonidis, J. H., Senturia, S. D., Warkentin, D. J., and Mehregany, M., 1990a, ''Optical Micropressure Transducer,'' United States Patent number 4,926,696, 22 May 1990.

Haritonidis, J. H., Senturia, S. D., Warkentin, D. J., and Mehregany, M., 1990b, ''Pressure Transducer Apparatus,'' United States Patent number 4,942,767, 24 July 1990.

Harley, J. C., Huang, Y., Bau, H. H., and Zemel, J. N., 1995, ''Gas Flow in Micro-Channels,'' *Journal of Fluid Mechanics,* Vol. 284, pp. 257–274.

Hirschfelder, J. O., Curtiss, C. F., and Bird, R. B., 1954, *Molecular Theory of Gases and Liquids,* Wiley, New York.

Ho, C.-M., and Tai, Y.-C., 1996, ''Review: MEMS and Its Applications for Flow Control,'' ASME Journal of Fluids Engineering, Vol. 118, pp. 437–447.

Ho, C.-M., and Tai, Y.-C., 1998, ''Micro-Elctro-Mechanical Systems (MEMS) and Fluid Flows,'' *Annual Review of Fluid Mechanics,* Vol. 30, pp. 579–612.

Ho, C.-M., Tung, S., Lee, G. B., Tai, Y.-C., Jiang, F., and Tsao, T., 1997, ''MEMS—A Technology for Advancements in Aerospace Engineering,'' AIAA Paper No. 97-0545, AIAA, Washington, D.C.

Hogan, H., 1996, ''Invasion of the micromachines,'' *New Scientist,* 29 June, pp. 28–33.

Israelachvili, J. N., 1986, ''Measurement of the Viscosity of Liquids in Very Thin Films,'' *Journal of Colloid and Interface Science,* Vol. 110, pp. 263–271.

Israelachvili, J. N., 1991, *Intermolecular and Surface Forces,* second edition, Academic Press, New York.

Jacobson, S. A., and Reynolds, W. C., 1993, ''Active Control of Boundary Layer Wall Shear Stress Using Self-Learning Neural Networks,'' AIAA Paper No. 93-3272, AIAA, Washington, D.C.

Jacobson, S. A., and Reynolds, W. C., 1995, ''An Experimental Investigation Towards the Active Control of Turbulent Boundary Layers,'' Department of Mechanical Engineering Report No. TF-64, Stanford University, Stanford, California.

Jacobson, S. A., and Reynolds, W. C., 1998, ''Active Control of Streamwise Vortices and Streaks in Boundary Layers,'' *Journal of Fluid Mechanics,* Vol. 360, pp. 179–211.

James, R. D., Jacobs, J. W., and Glezer, A., 1994, ''Experimental Investigation of a Turbulent Jet Produced by an Oscillating Surface Actuator,'' *Applied Mechancs Reviews,* Vol. 47, pp. S127–S1131.

Jeffery, G. B., 1920, ''Plane Stress and Plane Strain in Bipolar Co-ordinates,'' *Philosophical Transactions of the Royal Society, Series A,* Vol. 221, pp. 265–289.

Kamal, M. M., 1966, ''Separation in the Flow Between Eccentric Rotating Cylinders,'' ASME *Journal of Basic Engineering,* Vol. 88, pp. 717–724.

Kennard, E. H., 1938, *Kinetic Theory of Gases,* McGraw-Hill, NY.

Knudsen, M., 1909, ''Die Gesetze der Molekularströmung und der inneren Reibungsströmung der Gase durch Röhren,'' *Annalen der Physik,* Vol. 28, pp. 75–130.

Kogan, M. N., 1969, *Rarefied Gas Dynamics,* Nauka, Moscow. Translated from Russian, L. Trilling, ed., Plenum, NY.

Kogan, M. N., 1973, ''Molecular Gas Dynamics,'' *Annual Review of Fluid Mechanics,* Vol. 5, pp. 383–404.

Koplik, J., and Banavar, J. R., 1995, ''Continuum Deductions from Molecular Hydrodynamics,'' *Annual Review of Fluid Mechanics,* Vol. 27, pp. 257–292.

Kundu, P. K., 1990, *Fluid Mechanics,* Academic Press, NY.

Landau, L. D., and Lifshitz, E. M., 1987, *Fluid Mechanics,* Second Edition, Pergamon Press, Oxford, United Kingdom.

Liang, W. J., and Liou, J. A., 1995, ''Flow Around a Rotating Cylinder Near a Plane Boundary,'' *Journal of the Chinese Institute of Engineers,* Vol. 18, pp. 35–50.

Liepmann, H. W., and Nosenchuck, D. M., 1982, ''Active Control of Laminar-Turbulent Transition,'' *Journal of Fluid Mechanics,* Vol. 118, pp. 201–204.

Liepmann, H. W., Brown, G. L., and Nosenchuck, D. M., 1982, ''Control of Laminar Instability Waves Using a New Technique,'' *Journal of Fluid Mechanics,* Vol. 118, pp. 187–200.

Lighthill, M. J., 1963, ''Introduction. Real and Ideal Fluids,'' in *Laminar Boundary Layers,* L. Rosenhead, ed., pp. 1–45, Clarendon Press, Oxford, United Kingdom.

Lipkin, R., 1993, ''Micro Steam Engine Makes Forceful Debut,'' *Science News,* Vol. 144, p. 197.

Liu, J., Tai, Y. C., Lee, J., Pong, K. C., Zohar, Y., and Ho, C. M., 1993, ''In-Situ Monitoring and Universal Modeling of Sacrificial PSG Etching Using Hydrofluoric Acid,'' *Proceedings IEEE Micro Electro Mechanical Systems '93,* pp. 71–76, IEEE, NY.

Liu, J., Tai, Y. C., Pong, K., and Ho, C. M., 1995, ''MEMS for Pressure Distribution Studies of Gaseous Flows in Microchannels,'' *Proceedings IEEE Micro Electro Mechanical Systems '95,* pp. 209–215, IEEE, NY.

Loeb, L. B., 1961, *The Kinetic Theory of Gases,* third edition, Dover, New York.

Löfdahl, L., and Gad-el-Hak, M., 1999, ''MEMS Applications in Turbulence and Flow Control,'' *Progress in Aerospace Sciences,* Vol. 35, pp. 101–203.

Löfdahl, L., Glavmo, M., Johansson, B., and Stemme, G., 1993, ''A Silicon Transducer for the Determination of Wall-Pressure Fluctuations in Turbulent Boundary Layers,'' *Applied Scientific Research,* Vol. 51, pp. 203–207.

Löfdahl, L., Kälvesten, E., and Stemme, G., 1994, ''Small Silicon Based Pressure Transducers for Measurements in Turbulent Boundary Layers,'' *Experiments in Fluids,* Vol. 17, pp. 24–31.

Löfdahl, L., Kälvesten, E., and Stemme, G., 1996, ''Small Silicon Pressure Transducers for Space-Time Correlation Measurements in a Flat Plate Boundary Layer,'' ASME JOURNAL OF FLUIDS ENGINEERING, Vol. 118, pp. 457–463.

Loose, W., and Hess, S., 1989, ''Rheology of Dense Fluids via Nonequilibrium Molecular Hydrodynamics: Shear Thinning and Ordering Transition,'' *Rheologica Acta,* Vol. 28, p. 91–101.

Lumley, J. L., 1991, ''Control of the Wall Region of a Turbulent Boundary Layer,'' *Turbulence: Structure and Control,* J. M. McMichael, ed., pp. 61–62, 1–3 Apr., Ohio State University, Columbus, OH.

Lumley, J. L., 1996, ''Control of Turbulence,'' AIAA paper No. 96-0001, AIAA, Washington, D.C.

Lumley, J., and Blossey, P., 1998, ''Control of Turbulence,'' *Annual Review of Fluid Mechanics,* Vol. 30, pp. 311–327.

Majumdar, A., and Mezic, I., 1998, ''Stability Regimes of Thin Liquid Films,'' *Microscale Thermophysical Engineering,* Vol. 2, pp. 203–213.

Majumdar, A., and Mezic, I., 1999, ''Instability of Ultra-Thin Water Films and the Mechanism of Droplet Formation on Hydrophilic Surfaces,'' *Proceedings of the ASME-JSME Thermal Engineering and Solar Energy Joint Conference,* San Diego, CA, 15–19 March.

Mastrangelo, C., and Hsu, C. H., 1992, ''A Simple Experimental Technique for the Measurement of the Work of Adhesion of Microstructures,'' *Technical Digest IEEE Solid-State Sensors and Actuators Workshop,* pp. 208–212, IEEE, NY.

Maureau, J., Sharatchandra, M. C., Sen, M., and Gad-el-Hak, M., 1997, ''Flow and Load Characteristics of Microbearings with Slip,'' *Journal of Micromechanics and Microengineering,* Vol. 7, pp. 55–64.

Maxwell, J. C., 1879, ''On Stresses in Rarefied Gases Arising from Inequalities of Temperature,'' *Philosophical Transactions of the Royal Society Part 1,* Vol. 170, pp. 231–256.

McMichael, J. M., 1996, ''Progress and Prospects for Active Flow Control Using Microfabricated Electromechanical Systems (MEMS),'' AIAA Paper No. 96-0306, AIAA, Washington, D.C.

Mehregany, M., DeAnna, R. G., Reshotko, E., 1996, ''Microelectromechanical Systems for Aerodynamics Applications,'' AIAA Paper No. 96-0421, AIAA, Washington, D.C.

Migun, N. P., and Prokhorenko, P. P., 1987, ''Measurement of the Viscosity of Polar Liquids in Microcapillaries,'' *Colloid Journal of the USSR,* Vol. 49, pp. 894–897.

Moffatt, H. K., 1964, ''Viscous and Resistive Eddies Near a Sharp Corner,'' *Journal of Fluid Mechanics,* Vol. 18, pp. 1–18.

Moin, P., and Bewley, T., 1994, ''Feedback Control of Turbulence,'' *Applied Mechanics Reviews,* Vol. 47, pp. S3–S13.

Moroney, R. M., White, R. M., and Howe, R. T., 1991 ''Ultrasonically Induced Microtransport,'' *Proceedings IEEE Micro Electro Mechanical Systems '91,* Nara, Japan, pp. 277–282, IEEE, NY.

Muntz, E. P., 1989, ''Rarefied Gas Dynamics,'' *Annual Review of Fluid Mechanics,* Vol. 21, pp. 387–417.

Nadolink, R. H., and Haigh, W. W., 1995, ''Bibliography on Skin Friction Reduction with Polymers and other Boundary-Layer Additives,'' *Applied Mechanics Reviews,* Vol. 48, pp. 351–459.

Nakagawa, S., Shoji, S., and Esashi, M., 1990, ''A Micro-Chemical Analyzing System Integrated on Silicon Chip,'' *Proceedings IEEE: Micro Electro Mechanical Systems,* IEEE 90CH2832-4, Napa Valley, CA.

O'Connor, L., 1992, ''MEMS: Micromechanical Systems,'' *Mechanical Engineering,* Vol. 114, Feb., pp. 40–47.

Odell, G. M., and Kovasznay, L. S. G., 1971, ''A New Type of Water Channel with Density Stratification,'' *Journal of Fluid Mechanics,* Vol. 50, pp. 535–543.

Oran, E. S., Oh, C. K., and Cybyk, B. Z., 1998, ''Direct Simulation Monte Carlo: Recent Advances and Applications,'' *Annual Review of Fluid Mechanics,* Vol. 30, pp. 403–441.

Panton, R. L., 1996, *Incompressible Flow,* Second Edition, Wiley-Interscience, NY.

Pearson, J. R. A., and Petrie, C. J. S., 1968, ''On Melt Flow Instability of Extruded Polymers,'' *Polymer Systems: Deformation and Flow,* R. E. Wetton and R. W. Whorlow, eds., pp. 163–187, Macmillan, London, United Kingdom.

Pfahler, J., 1992, ''Liquid Transport in Micron and Submicron Size Channels,'' Ph.D. thesis, University of Pennsylvania, Philadelphia, Pennsylvania.

Pfahler, J., Harley, J., Bau, H., and Zemel, J. N., 1990, ''Liquid Transport in Micron and Submicron Channels,'' *Sensors and Actuators,* Vol. A21–A23, pp. 431–434.

Pfahler, J., Harley, J., Bau, H., and Zemel, J. N., 1991, ''Gas and Liquid Flow in Small Channels,'' *Symposium on Micromechanical Sensors, Actuators, and Systems,* D. Cho et al., eds., ASME DSC-Vol. 32, pp. 49–60, ASME, NY.

Piekos, E. S., and Breuer, K. S., 1996, ''Numerical Modeling of Micromechanical Devices Using the Direct Simulation Monte Carlo Method,'' ASME JOURNAL OF FLUIDS ENGINEERING, Vol. 118, pp. 464–469.

Piekos, E. S., Orr, D. J., Jacobson, S. A., Ehrich, F. F., and Breuer, K. S., 1997, ''Design and Analysis of Microfabricated High Speed Gas Journal Bearings,'' AIAA Paper No. 97-1966, AIAA, Reston, VA.

Pister, K. S. J., Fearing, R. S., and Howe, R. T., 1990, ''A Planar Air Levitated Electrostatic Actuator System,'' IEEE Paper No. CH2832-4/90/0000-0067, IEEE, NY.

Pong, K.-C., Ho, C.-M., Liu, J., and Tai, Y.-C., 1994, ''Non-Linear Pressure Distribution in Uniform Microchannels,'' *Application of Microfabrication to Fluid Mechanics 1994,* P. R. Bandyopadhyay, K. S. Breuer and C. J. Belchinger, eds., ASME FED-Vol. 197, pp. 47–52, ASME, NY.

Porodnov, B. T., Suetin, P. E., Borisov, S. F., and Akinshin, V. D., 1974, ''Experimental Investigation of Rarefied Gas Flow in Different Channels,'' *Journal of Fluid Mechanics,* Vol. 64, pp. 417–437.

Prud'homme, R. K., Chapman, T. W., and Bowen, J. R., 1986, ''Laminar Compressible Flow in a Tube,'' *Applied Scientific Research,* Vol. 43, pp. 67–74.

Reynolds, W. C., 1993, ''Sensors, Actuators, and Strategies for Turbulent Shear-Flow Control,'' invited oral presentation at the AIAA Third Flow Control Conference, Orlando, FL, 6–9 July.

Richardson, S., 1973, ''On the No-Slip Boundary Condition,'' *Journal of Fluid Mechanics,* Vol. 59, pp. 707–719.

Richter, A., Plettner, A., Hofmann, K. A., and Sandmaier, H., 1991, ''A Micromachined Electrohydrodynamic (EHD) Pump,'' *Sensors and Actuators A,* Vol. 29, pp. 159–168.

Robinson, S. K., 1991, ''Coherent Motions in the Turbulent Boundary Layer,'' *Annual Review of Fluid Mechanics,* Vol. 23, pp. 601–639.

Schaaf, S. A., and Chambré, P. L., 1961, *Flow of Rarefied Gases,* Princeton University Press, Princeton, NJ.

Seidl, M., and Steinheil, E., 1974, ''Measurement of Momentum Accommodation Coefficients on Surfaces Characterized by Auger Spectroscopy, SIMS and LEED,'' *Rarefied Gas Dynamics 9,* M. Becker and M. Fiebig, eds., pp. E9.1–E9.2, DFVLR-Press, Porz-Wahn, Germany.

Sen, M., Wajerski, D., and Gad-el-Hak, M., 1996, ''A Novel Pump for MEMS Applications,'' ASME JOURNAL OF FLUIDS ENGINEERING, Vol. 118, pp. 624–627.

Sharatchandra, M. C., Sen, M., and Gad-el-Hak, M., 1997, ''Navier-Stokes Simulations of a Novel Viscous Pump,'' ASME JOURNAL OF FLUIDS ENGINEERING, Vol. 119, pp. 372–382.

Sharatchandra, M. C., Sen, M., and Gad-el-Hak, M., 1998a, ''Thermal Aspects of a Novel Micropumping Device,'' ASME *Journal of Heat Transfer*, Vol. 120, pp. 99–107.

Sharatchandra, M. C., Sen, M., and Gad-el-Hak, M., 1998b, ''A New Approach to Constrained Shape Optimization Using Genetic Algorithms,'' *AIAA Journal*, Vol. 36, pp. 51–61.

Sherman, F. S., 1990, *Viscous Flow*, McGraw-Hill, NY.

Shih, J. C., Ho, C.-M., Liu, J., and Tai, Y.-C., 1995, ''Non-Linear Pressure Distribution in Uniform Microchannels,'' ASME AMD-MD-Vol. 238, ASME, NY.

Shih, J. C., Ho, C.-M., Liu, J., and Tai, Y-. C., 1996, ''Monatomic and Polyatomic Gas Flow through Uniform Microchannels,'' *Applications of Microfabrication to Fluid Mechanics*, K. Breuer, P. Bandyopadhyay and M. Gad-el-Hak, eds., ASME DSC-Vol. 59, pp. 197–203, ASME, NY.

Smits, J. G., 1990, ''Piezoelectric Micropump with Three Valves Working Peristaltically,'' *Sensors and Actuators A*, Vol. 21–23, pp. 203–206.

Smoluchowski, von M., 1898, ''Ueber Wärmeleitung in verdünnten Gasen,'' *Annalen der Physik und Chemie*, Vol. 64, pp. 101–130.

Sniegowski, J. J., and Garcia, E. J., 1996, ''Surface Micromachined Gear Trains Driven by an On-Chip Electrostatic Microengine,'' *IEEE Electron Device Letters*, Vol. 17, July, p. 366.

Swift, J., 1727, *Gulliver's Travels*, 1906 reprinting, J. M. Dent and Company, London.

Tai, Y.-C., and Muller, R. S., 1989, ''IC-Processed Electrostatic Synchronous Micromotors,'' *Sensors and Actuators*, Vol. 20, pp. 49–55.

Tang, W. C., Nguyen, T.-C., and Howe, R. T., 1989, ''Laterally Driven Polysilicon Resonant Microstructures,'' *Sensors and Actuators*, Vol. 20, pp. 25–32.

Taylor, G., 1972, ''Low-Reynolds-Number Flows,'' *Illustrated Experiments in Fluid Mechanics*, pp. 47–54, National Committee for Fluid Mechanics Films, MIT Press, Cambridge, MA.

Tennekes, H., and Lumley, J. L., 1972, *A First Course in Turbulence*, MIT Press, Cambridge, MA.

Thomas, L. B., and Lord, R. G., 1974, ''Comparative Measurements of Tangential Momentum and Thermal Accommodations on Polished and on Roughened Steel Spheres,'' *Rarefied Gas Dynamics 8*, K. Karamcheti, ed., Academic Press, NY.

Thompson, P. A., and Robbins, M. O., 1989, ''Simulations of Contact Line Motion: Slip and the Dynamic Contact Line,'' *Nature*, Vol. 389, 25 Sept., pp. 360–362.

Thompson, P. A., and Troian, S. M., 1997, ''A General Boundary Condition for Liquid Flow at Solid Surfaces,'' *Physical Review Letters*, Vol. 63, pp. 766–769.

Tien, N. C., 1997, ''Silicon Micromachined Thermal Sensors and Actuators,'' *Microscale Thermophysical Engineering*, Vol. 1, pp. 275–292.

Tison, S. A., 1993, ''Experimental Data and Theoretical Modeling of Gas Flows Through Metal Capillary Leaks,'' *Vacuum*, Vol. 44, pp. 1171–1175.

Tsao, T., Jiang, F., Miller, R. A., Tai, Y.-C., Gupta, B., Goodman, R., Tung, S., and Ho, C.-M., 1997, ''An Integrated MEMS System for Turbulent Boundary Layer Control,'' *Technical Digest (Transducers '97)*, Vol. 1, pp. 315–318.

Tuckermann, D. B., 1984, ''Heat Transfer Microstructures for Integrated Circuits,'' Ph.D. Thesis, Stanford University, Stanford, CA.

Tuckermann, D. B., and Pease, R. F. W., 1981, ''High-Performance Heat Sinking for VLSI,'' *IEEE Electron Device Letters*, Vol. EDL-2, No. 5, May.

Tuckermann, D. B., and Pease, R. F. W., 1982, ''Optimized Convective Cooling Using Micromachined Structures,'' *Journal of Electrochemical Society*, Vol. 129, no. 3, C98, March.

Van den Berg, H. R., Seldam, C. A., and Gulik, P. S., 1993, ''Compressible Laminar Flow in a Capillary,'' *Journal of Fluid Mechanics*, Vol. 246, pp. 1–20.

Van Lintel, H. T. G., Van de Pol, F. C. M., and Bouwstra, S., 1988, ''A Piezoelectric Micropump Based on Micromachining of Silicon,'' *Sensors and Actuators*, Vol. 15, pp. 153–167.

Vargo, S. E., and Muntz, E. P., 1996, ''A Simple Micromechanical Compressor and Vacuum Pump for Flow Control and Other Distributed Applications,'' AIAA Paper No. 96-0310, AIAA, Washington, D.C.

Vincenti, W. G., and Kruger, C. H., Jr., 1965, *Introduction to Physical Gas Dynamics*, Wiley, NY.

Wadsworth, D. C., Muntz, E. P., Blackwelder, R. F., and Shiflett, G. R., 1993, ''Transient Energy Release Pressure Driven Microactuators for Control of Wall-Bounded Turbulent Flows,'' AIAA Paper No. 93-3271, AIAA, Washington, D.C.

Wannier, G. H., 1950, ''A Contribution to the Hydrodynamics of Lubrication,'' *Quarterly of Applied Mathematics*, Vol. 8, pp. 1–32.

Warkentin, D. J., Haritonidis, J. H., Mehregany, M., and Senturia, S. D., 1987, ''A Micromachined Microphone with Optical Interference Readout,'' *Proceedings of the Fourth International Conference on Solid-State Sensors and Actuators (Transducers '87)*, Tokyo, Japan, June.

Went, F. W., 1968, ''The Size of Man,'' *American Scientist*, Vol. 56, pp. 400–413.

Wilkinson, S. P., 1990, ''Interactive Wall Turbulence Control,'' in Viscous Drag Reduction in Boundary Layers, D. M. Bushnell and J. N. Hefner, eds., *Progress in Astronautics and Aeronautics*, Vol. 123, 479–509, AIAA, Washington, D.C.

Wiltse, J. M., and Glezer, A., 1993, ''Manipulation of Free Shear Flows Using Piezoelectric Actuators,'' *Journal of Fluid Mechanics*, Vol. 249, pp. 261–285.

Young, A. M., Goldsberry, J. E., Haritonidis, J. H., Smith, R. I., and Senturia, S. D., 1988, ''A Twin-Interferometer Fiber-Optic Readout for Diaphragm Pressure Transducers,'' *IEEE Solid-State Sensor and Actuator Workshop*, June 6–9, Hilton Head, SC.